BLINDED BY THE LIGHT: AN HL-LHC EXTRAPOLATION OF THE RUN 2 SUSY ELECTROWEAK ANALYSIS ENDING IN FULLY HADRONIC FINAL STATES

Joseph J. Mullin

A DISSERTATION
in
Physics and Astronomy

Presented to the Faculties of The University of Pennsylvania
in
Partial Fulfillment of the Requirements for the
Degree of Doctor of Philosophy
2024

Supervisor of Dissertation

Hugh H. Williams, Mary Amanda Wood Professor of Physics

Graduate Group Chairperson

Ravi Sheth, Professor, Physics and Astronomy

Dissertation Committee

Evelyn Thomson, Professor, Physics and Astronomy
I. Joseph Kroll, Professor, Physics and Astronomy
Christopher M. Mauger, Associate Professor, Physics and Astronomy
Philip Nelson, Professor, Physics and Astronomy

BLINDED BY THE LIGHT: AN HL-LHC EXTRAPOLATION OF THE RUN 2 SUSY ELECTROWEAK ANALYSIS ENDING IN FULLY HADRONIC FINAL STATES

ACKNOWLEDGEMENTS

First and foremost I would like to thank every advisor and mentor I have had over many years. Every single one has played a critical role in encouraging me and fostering my growth. This begins with David Stuart, my research advisor at UCSB. Without your influence I'm not sure I would have pursued my PhD in the first place. You took me on as a Sophomore and taught me an incredible amount over the rest of my time in Santa Barbara. I learned so much about putting the scientific method into practice, electronics, debugging, and looking foward at the goals of our research from working with you. I can't put into words how thankful I am to Brig Williams and Joe Kroll for helping me to reach this point. You both had faith in me and encouraged me at points when I had very little in myself. You have both been unbelievably supportive and understanding while giving me the resources I needed to succeed. Brig, over many years I have learned so much about how to look more deeply at results and ask questions to foster my understanding of what is going on inside of any result. Your insight into my work, both on the TRT and analyses, has helped me to keep an eye on the big picture while still exploring the details of each individual problem. Your leadership of the ATLAS group has helped everyone in the group put forward the best work possible. Joe, from my first semester teaching the electronics lab you've always helped me to learn and push my boundaries. I not only enjoyed it, but I learned as much from teaching that lab as I had from my electronics work in undergrad and that prepared me to be successful working on the TRT for many years after. Your ability to slow down speakers and ask critical questions that I was either nervous about asking or unsure how to phrase has always been very appreciated and made any meeting I was in with you much more informative. Thank you Evelyn

Thomson for being the chair of my committee and always helping to keep the process moving and checking in when things seem to have slowed down, I am extremely grateful for your help. To Elliot Lipeles, your presentations at meetings and input on a wide range of topics have improved my understanding on countless occasions and always help to give a deeper level of connection.

Working with the TRT DAQ team has easily been my favorite part of my time at Penn. Right from my first arrival in Geneva when Chris Meyer picked me up from the airport and Bijan Haney showed me the way to where I would be staying in France, the DAQ team has always made me feel at home. Khilesh Mistry taught me an enormous amount about the lab I would eventually spend so many hours working in. Coming into the office that summer was always something to look forward to knowing I would be met with smiles and extremely helpful explanations from Elodie Resseguie and Bijan. I wouldn't have been so successful with my time in Geneva without the help and guidance from Anatoli and Dominik as well. Thank you to everyone on the DAQ team over the years who have given me great memories, an incredible working environment, and both taught me and helped me to do my own work: Chris, Khilesh, Bijan, Elodie, Vincent, Keisuke, Ian, Shion, Lauren, Gwen, Jeff, Nadia, Daniil, Hayden, Colin, Mike, Brig, Joe, Paul, and Mitch. We could never have been successful without the constant support from our DCS colleagues, thank you Elzbieta, Jola, Dominik, and Bartlomeij. The TRT was so well run when I arrived and thanks to all of you, as well as the best leadership I could ask for from Anatoli and Dominik, we've kept our detector running at its best.

Throughout graduate school I have worked through a number of medical issues, both physical and mental, and have benefitted from excellent medical care and an incredible group around me that has supported me through it. I am constantly grateful for having such an amazing cohort including Ben, Jesse, Stephen, Pedro, Jack, Emilie, Sophie, and Matt who made the transition to Philly so easy and fun while keeping my spirits up during some difficult times. Many nights of board games and DnD have always been a high point in my weeks. Also so many incredible students from other years who have expaned my boundaries, given me advice, and just been there to chat, thank you Tasha, David, Luis, Elodie, Khilesh, Bijan, Ian, Lucas, Joey, Lauren, Gwen, Bobby, Michael, and Rebecca. I also had the benefit of very close friends I made through the Penn gym that have kept me connected over many years including Nate, Enoch, Carol, Michael, Amanda, Carl, Kevin, Adnan, Isabell, Naomi, Val, Cody, Albert, Isaac, Greg, Adam, Greta, and many more that I may not have included but I have not forgotten. And again, Brig, you were so supportive and understanding through every setback and every situation I struggled with. You always gave me the opportunities I needed, both in my work and personal life.

Finally, and most importantly, I am so grateful for my family who has supported me through my education througout my entire life. Katherine, I could not have asked for a better and more understanding sister. You know me better than anyone in the world and somehow still put up with all of my nonsense. I don't think there's a single person I am more comfortable talking to or more likely to confide in, in the world. You have always kept an eye out for me as my big sister and I will do my best to be a good uncle for your son when human Sid comes, even when I struggle with little kids. Mom, you have always been such a supportive person and are always looking out for my best interest, even when I start to find it a bit annoying. You've put up with talking to me on the phone for hours over the last few years and always give me a place to vent. Dad, you definitely got me started on the road to studying math and science and have always been interested in what I'm researching. I always look forward to getting to play video games or board games with you and your friends when I'm back home. And Ma, you were always my biggest fan and I know you've been keeping an eye out for me from above for the last eight years. I will forever cherish that tie, even if it's rarely worn, and hope I can keep making you proud. I love you all.

ABSTRACT

BLINDED BY THE LIGHT: AN HL-LHC EXTRAPOLATION OF THE RUN 2 SUSY ELECTROWEAK ANALYSIS ENDING IN FULLY HADRONIC FINAL STATES

Joseph J. Mullin

Hugh H. Williams

This thesis presents the prospects of a search for charginos and neutralinos using fully hadronic final states and missing transverse momentum at the HL-LHC, assuming an integrated luminosity of 3 ab^{-1} and a center-of-mass energy of $\sqrt{s} = 14$ TeV. This search focuses on pair produced electroweakinos that decay into a high-p_{T}gauge or Higgs boson and a neutral stable particle that escapes the detector. Fully hadronic decay modes of W/Z/Higgs bosons are exploited for their large branching ratio and highly efficient background rejection by identifying high-p_{T}bosons using large-radius jets and jet substructure information. The results are presented as expected 95% CL exclusion limits on the particle masses for each simplified model as well as 5σ discovery limits. A wino mass of up to 1560 GeV can be excluded depending on the mass of the bino, the lightest supersymmetric particle in this model. Similarly, a higgsino mass up to 1675 GeV can be excluded in the General Gauge Mediation model with a nearly massless gravitino as the lightest supersymmetric particle. The search is expected to achieve 5σ discovery potential over a wide range of masses that are not excluded by current searches using the LHC Run2 dataset.

TABLE OF CONTENTS

ACKNOWLEDGEMENTS iii

ABSTRACT vi

LIST OF TABLES xi

LIST OF ILLUSTRATIONS xiii

INTRODUCTION 1

1 THEORETICAL FRAMEWORK 8

1.1 Introduction to the Standard Model 8

1.2 The Higgs Mechanism 11

1.3 Beyond the Standard Model 13

1.3.1 Supersymmetry 15

1.3.2 Electroweakly-Produced Supersymmetric Particles 17

2 LHC AND THE ATLAS DETECTOR 18

2.1 The Large Hadron Collider 18

2.1.1 Luminosity 20

2.1.2 Pileup 21

2.2 The ATLAS Detector 21
2.2.1 The Inner Detector 23
2.2.1.1 Pixel Detector 24
2.2.1.2 Semiconductor Tracker 25
2.2.1.3 Transition Radiation Tracker 25
2.2.2 The Calorimeters 26
2.2.2.1 Liquid Argon Calorimeters 28
2.2.2.2 Tile Calorimeters 29
2.2.3 Muon Spectrometer 29
2.3 Object reconstruction 32
2.4 Transition Radiation Tracker Studies 33
2.4.1 TRT Overview 34
2.4.2 TRT Electronics 34
2.4.2.1 TRT Synchronization 36
2.4.2.2 Run 2 Lock Error investigation 38
2.4.2.3 Phase Shift Board Investigation 41
2.4.2.4 Frequency Modulation Investigation 44
2.4.2.5 Going Forward and Final Thoughts 45

3 TRANSITION RADIATION TRACKER COMPRESSION STUDIES 48

3.1 Introduction 48
3.2 Compressing Data 49
3.2.1 Lossless Compression 51
3.2.2 Lossy Compression 51
3.2.3 Run 2 Final Setup 52
3.2.4 Possible Changes 54
3.3 Compression Studies 56

3.4 Run 3 Projected Setup 60

3.5 Documentation 61

4 FULLY-HADRONIC ELECTROWEAK SUSY **63**

4.1 Target Physics Scenarios 63

4.1.1 MSSM scenarios: $(\widetilde{W}, \widetilde{B}), (\widetilde{W}, \widetilde{H}), (\widetilde{H}, \widetilde{B}), (\widetilde{H}, \widetilde{W})$ 64

4.1.2 GGM scenario with gravitino-LSP: $(\widetilde{H}, \widetilde{G})$ 65

4.1.3 QCD axion SM extension with axino-LSP: $(\widetilde{H}, \tilde{a})$ 66

4.2 Datasets and Monte Carlo Samples 67

4.2.1 Data Samples 67

4.2.2 Monte Carlo Simulation 68

4.2.2.1 SM Backgrounds 69

4.2.2.2 Signal 70

4.3 Object Definitions 71

4.4 Event Selection 75

4.4.1 Pre-selection 76

4.4.2 Signal Region Definition 76

4.4.3 Kinematic Selections 78

4.5 Background Estimation 79

4.5.1 QCD multi-jets estimation 82

4.5.1.1 0-lepton regions 83

4.6 Results 87

4.6.1 $(\widetilde{W}, \widetilde{B})$ simplified model exclusion limits 88

4.6.2 $(\widetilde{H}, \widetilde{G})$ model exclusion limits 89

4.6.3 $(\widetilde{H}, \tilde{a})$ model exclusion limits 89

5 **EXTRAPOLATION OF ALL-HADRONIC SUSY SEARCH TO HL-LHC CONDITIONS** **93**

5.1 Intorduction and Motivation . . . 94

5.2 Changes to the Atlas Detector . . . 96

5.3 Target Physics Models . . . 97

5.4 Monte Carlo Simulations . . . 98

5.5 Event Reconstruction and Object Definitions . . . 100

5.6 Event Selection . . . 103

5.6.1 Preselection . . . 103

5.6.2 Signal Region Definitions . . . 104

5.6.3 4Q Signal Regions . . . 105

5.6.4 2B2Q Signal Regions . . . 106

5.6.5 4B Signal Region . . . 107

5.7 Results . . . 110

5.8 Conclusion . . . 116

6 **CONCLUSION** **117**

BIBLIOGRAPHY **120**

LIST OF TABLES

3.1 Table showing increase in allowed occupancy of the TRT . . . 58

4.1 Summary of the production modes, final states, signal regions (SRs) used for the hypothetical tests and the branching ratio assumptions for the signal models targeted in the search. The $(\widetilde{W}, \widetilde{B})$ and $(\widetilde{H}, \widetilde{G})$ models are used for optimizing the selection, and the remainder are considered for interpretation. For the $(\widetilde{W}, \widetilde{H})$ and $(\widetilde{H}, \widetilde{W})$ models, various values of the three MSSM paramaters are considered. For M_2 and μ the values 0–1.2 TeV and -1.2TeV–1.2 TeV respectively are scanned over and the values of 2, 5, 10, and 30 are tested for $\tan\beta$. The $(\widetilde{W}, \widetilde{B})$ simplified models are also interpreted in this analysis in order to compare with past ATLAS electroweakino search results. 68

4.2 Definition of each SR in the 4Q and 2B2Q categories. $n(W_{qq})$, $n(Z_{qq})$, $n(V_{qq})$, $n(Z_{bb})$, and $n(h_{bb})$ are respectively the number of large-R jets that pass the W_{qq}-, Z_{qq}-, V_{qq}-, Z_{bb}-, and h_{bb}-tagging of two leading large-R jets. Note that 4QWZ requires $n(W_{qq}), n(Z_{qq}) \geq 1$ rather than $n(W_{qq}), n(Z_{qq}) = 1$ because the selection of W_{qq}- and Z_{qq}-tagging are not exclusive. Fig 4.4 shows the overlap between the SRs. . . . 77

4.3 Summary of selections for the SRs, CRs, and VRs. $n(V_{qq})$ and $n(!V_{qq})$ are the number of large-R jets that pass and fail the V_{qq}-tagging between the two highest-p_{T}large-R jets respectively. The same selection is applied in the SR or VR and CR in the same category except for the V_{qq}-tagging and some kinematic selections that are explicitly indicated in parentheses. . . . 80

4.4 . . . 85

4.5 . . . 87

4.6 . . . 87

5.1 Summary of the production modes, final states, signal regions (SRs), and the branching ratio assumptions for the signal models targeted in the search. . . . 98

5.2 Summary of selections for the SRs. $n(V_{qq})$ represents the number of large-R jets passing V_{qq}-tagging of the two highest-p_{T}large-R jets. The trigger selection and event cleaning described in Section 4.4 are also applied. . . . 109

5.3 Definition of each SR in the 4Q, 2B2Q, and 4B categories; where $n(W_{qq})$, $n(Z_{qq})$, $n(V_{qq})$, $n(Z_{bb})$, and $n(h_{bb})$ are respectively the number of large-R jets passing the W_{qq}-, Z_{qq}-, V_{qq}-, Z_{bb}-, and h_{bb}-tagging of the two leading large-R jets. SR-4Q-WZ requires $n(W_{qq}), n(Z_{qq}) \geq 1$ instead of $n(W_{qq}) = n(Z_{qq}) = 1$ because the selections in W_{qq}- and Z_{qq}-tagging are not exclusive. . . . 109

5.4 Number of predicted MC data events and the SM backgrounds in the SRs. Negligible contributions are indicated by "-". The top set of rows shows all four $(\widetilde{W}, \widetilde{B})$ SRs. The notation in the first two rows of these regions, written Signal(A, B), indicates the number of Monte Carlo signal events for the mass splitting (A, B) GeV of $(\widetilde{\chi}_{\text{heavy}}, \widetilde{\chi}_{\text{light}})$. Similarly the next two rows are the significance (Z_{n}) values for the relevant mass splittings. The bottom set of rows shows the four SRs that are included in the $(\widetilde{H}, \widetilde{G})$ model. In this case the first two rows of use the notation Signal(X) indicating the number of MC signal events for the mass point X GeV with the branching ratio that gives the maximum yield. The next two rows are similarly the significance values for the corresponding mass point, again with the branching ratio that gives the greatest Z_{n} value. To avoid unnecessary granularity, the background category top is a combination of $t\bar{t}$, $t\bar{t} + X$, and $t + X$ and the category multiboson is a combination of diboson, tri-boson, and higgs. 111

LIST OF ILLUSTRATIONS

1.1 The Standard Model of Elementary Particles. 9
1.2 The potential for a complex scalar field for the case $\mu^2 < 0$ and $\lambda > 0$. 13
1.3 Fermionic loop correction to the Higgs Boson mass 14
1.4 Supermultiplets of the MSSM 16
1.5 Electroweakino mass spectra in target physics scenarios 17

2.1 LHC accelerator complex 19
2.2 Integrated luminosity over time 21
2.3 Run 2 average interactions per bunch crossing 22
2.4 General cut-away view of the ATLAS detector. 23
2.5 A cutaway showing the barrel section of the Inner Detector 24
2.6 Full schematic of the inner detector 25
2.7 SCT being placed into the center of the TRT 27
2.8 Cutaway view of the ATLAS calorimeters 27
2.9 Zoomed in view of the lead, liquid argon layering of the LAr detector. 28
2.10 Schematic of LAr calorimeter near $\eta = 0$ 29
2.11 Schematic representing a quarter of the muon system. 30
2.12 Cutaway image of the ATLAS muon system 31
2.13 Detector signatures of differend SM particles 33

3.1 Structure of the 27-bit straw word. For Run 2 the last 4 bits were dropped giving a 23-bit word. 50
3.2 Data structure of a ROD fragment. 50
3.3 Straw hitmaps generated by TRTViewer 53
3.4 TRT gas configuration 56
3.5 The equations that describe the fragment size and max L1 rate when the zero word is defined as a 2-bit code word that allows a relation between the TRT occupancy and the L1 rate. 57
3.6 Starting from equation 1 in Fig.3.5 and assuming the same L1 rate is constant when using each compression table, gives a condition on how the average word length affects the allowed occupancy of the detector at which it can run without delays. 57

4.1 Mass spectra and mass eigenstates for each model in the bino/wino/higgsino LSP scenario. Solid arrows indicate decay modes that emit a W-boson while dashed arrows represent a decay that emits a $Z-$ or Higgs boson. 65
4.2 Diagram of N2N1 production in the gravitino model where higgsino triplets are represented by $\tilde{H}$. 66
4.3 Diagram of N2N1 production in the axino model where higgsino triplets are represented by $\tilde{H}$. . 67

4.4 The SR segmentation is shown defined by the masses of the two leading large-R jets. In SR4Q (left), both jets are required to pass the W_{qq}- or Z_{qq}-tagging. In SR2B2Q (right), one jet is required to contain exactly two b-tagged track jets (J_{bb}) while the other has at most one (J_{qq}). The mass of J_{bb} is required to be consistent with Z ($70-100$ GeV) or h ($100-135$ GeV), while the J_{qq} is required to pass the W_{qq}- or Z_{qq}-tagging. The W_{qq}-/Z_{qq}-tagging has a variable mass window depending on p_{T}, the typical cut values are indicated. The inclusive SRs (VV, VZ, and Vh) defined by the logical union of two or three mutually overlapping SRs are indicated by the gray dashed lines. 78
4.5 Schematics illustrating how the SRs, VRs, and CRs differ in terms of jet-tagging in the (a) 4Q and (b) 2B2Q categories. As described in Section 4.5, the CRs are defined by the inversion of the V_{qq}-tagging requirement for one of the two leading large-R jets in the SR or VR. The J_{bb} mass window cut is also loosened slightly in the CRs and VRs. 82
4.6 $\min \Delta\phi(j, E_{\mathrm{T}}^{\mathrm{miss}})$ distribution of QCD multi-jet MC for events with (green) and without (red) a large-R jet passing the $V \to qq$ tagging. 0-lepton, $n_{\mathrm{Large}-R\ \mathrm{jets}} \geq 2$, $m_{\mathrm{eff}} > 1$ TeV, $n^{\mathrm{trk}}_{b-\mathrm{jet\ (inside\ J)}} \leq 1$ are applied for both plots. $E_{\mathrm{T}}^{\mathrm{miss}}$>100 GeV is additionally applied for the right plot. The areas for all the histograms are normalized to unity. 84
4.7 $\min \Delta\phi(j, E_{\mathrm{T}}^{\mathrm{miss}})$ distribution of the data and the MC BGs in the A+B region (top) and the C+D region (bottom) (separated at $\min \Delta\phi(j, E_{\mathrm{T}}^{\mathrm{miss}}) = 1.0$) with various $E_{\mathrm{T}}^{\mathrm{miss}}$thresholds. The QCD multi-jet MC is also overlaid as the reference. 86
4.8 Summary of observed data and predicted SM background for all Signal Regions. The bottom panel shows the significance of the difference seen between observed events and predicted SM expectations. 89
4.9 Exclusion limits for the $(\widetilde{W}, \widetilde{B})$ simplified model as a function of the produced wino mass ($m(\widetilde{\chi}_1^{\pm}/\widetilde{\chi}_2^0)$) and the bino LSP mass ($m(\widetilde{\chi}_1^0)$). Expected 95% CL exclusion limits are seen in dashed black lines with the observed limits in solid red for C1C1-WW (top-left), C1N2-WZ (top-right), and C1N2-Wh (bottom). Limits set by previous ATLAS searches on C1C1-WW [12], C1N2-WZ [14, 74], and C1N2-Wh [21] are shown by the light blue contours. Only the strongest mass limits from previous searches are shown. 90
4.10 Expected and observed 95% CL exlusion limits represented by dashed and solid red lines respectively. This is as a function of lightest higgsino mass and $\mathcal{B}(\tilde{\chi}_1^0 \to Z\tilde{G})$. 91
4.11 Expected and observed 95% CL exlusion limits represented by dashed and solid red lines respectively for the axino model. This is for $\mathcal{B}(\tilde{\chi}_1^0 \to Z\tilde{a}) = 100\%$ as a function of lightest higgsino mass and axino mass. 92

5.1 Diagrams of targeted models and final state/signatures are depicted. The final states represented in the top row are used for the $(\widetilde{W},\widetilde{B})$ model and all three final states are used for the $(\widetilde{H},\widetilde{G})$ model discussed in Section 5.3. In these diagrams, $\widetilde{\chi}_{\mathrm{heavy}}$ represents the wino doublet and higgsino triplet respectively and $\widetilde{\chi}_{\mathrm{light}}$ represents the bino and gravitino. 95
5.2 Diagram of N2N1 production for the gravitino model where higgsino triplets are represented by $\tilde{H}$. 99
5.3 The segmentation of the 4Q and 2B2Q categories illustrated as a function of the masses of the two leading large-R jets. Both jets must pass the W_{qq}- or Z_{qq}-tagging for the 4Q category where as in the 2B2Q category one must pass either W_{qq}- or Z_{qq}-tagging while the other must pass either Z_{bb}- or h_{bb}-tagging. Notably, the W_{qq}- and Z_{qq}-boson tagging uses dynamic mass windows as a function of p_{T}so the mass windows pictured are typical values. This leaves significant overlap between the possible masses of each. The Z_{bb}- and h_{bb}-boson tagging, on the other hand, uses a fixed mass window shown on the right. The inclusive SRs, defined by the logical union of a few mutually overlapping SRs, are indicated by the gray dashed lines. The 4B category is not pictured here as only one signal region is included for this analysis. 105

5.4 The m_{eff} distribution for the 4Q-WZ signal region (left) and min $\Delta\phi(E_{\text{T}}^{\text{miss}}, j)$ distribution for the 4Q-WW signal region (right). The plot shows number of events in MC simulation for signal events and each background. All selection criteria other than the kinematic variable being viewed are applied. The far right bin includes the overflow. The arrow represents the selected cuts for the purpose of optimization. The simulated signals are of the ($\tilde{W}$, $\tilde{B}$) model with $(m(\tilde{\chi}_1^{\pm}), m(\tilde{\chi}_1^0))$ $\approx (1300, 200)$ GeV for 4Q-WZ and $\approx (1100, 500)$ GeV for 4Q-WW. 107
5.5 The m_{eff} distribution for the 2B2Q category (left) and m_{T2} distribution for the 4B category (right). The plot shows number of events in MC simulation for signal events and each background. All selection criteria other than the kinematic variable being viewed are applied. The far right bin includes the overflow. The arrow represents the selected cuts for the purpose of optimization. Note that this cut looks somewhat loose, this is due to the low background statistics available. Tightening the cut very quickly causes a significant loss of background MC and the increase in error limits the significance value. Keeping a looser cut, given the amount of background MC available, maintains the highest significance; this cut, in an HL-LHC analysis where much higher MC statistics will be available, can likely be made much tighter. The simulated signals are of the ($\tilde{W}$, $\tilde{B}$) model with with a mass splitting of approximately $(1300, 200)$ GeV for the 2B2Q region and the GGM model with a mass point of 1300 GeV and a 50% branching ratio to Z/h for the 4B category. 108
5.6 C1C1-WW physics model significance contour that includes only SR-4Q-WW. The exclusion limit is calculated at 95% CL (Z_{n}=1.65). The blue region represents the 95% exclusion limit found in the Run 2 analysis calculated from observed events. The 5σ contour represents the projected limit for potential discovery. 112
5.7 The C1N2-WZ physics model significance contour that is a combination of SR-4Q-WZ and SR-2B2Q-WZ. Z_{n} values are added quadratically. The exclusion limit is calculated at 95% CL (Z_{n}=1.65). The blue region represents the 95% exclusion limit found in the Run 2 analysis. The 5σ contour represents the projected limit for potential discovery. 113
5.8 The C1N2-Wh physics model significance contour that is modeled entirely from SR-2B2Q-Wh. The exclusion limit is calculated at 95% CL (Z_{n}=1.65). The blue region represents the 95% exclusion limit found in the Run 2 analysis. The 5σ contour represents the projected limit for potential discovery. 114
5.9 GGM scenario significance contour utilizing boson efficiency and background rejection reweighting representing the 4B-hh signal region. This is a combination that also contains SR-2B2Q-ZZ, SR-2B2Q-Zh, and SR-4Q-ZZ all of which were modeled using explicit boson tagging cuts. The exclusion limit is calculated at 95% CL (Z_{n}=1.65). The y-axis shows the branching ratio of the lightest neutral higgsino into either a Z- or h boson. The top of the plot shows 100% decays into Z and the bottom shows decays entirely to the h bososn. The blue region represents the 95% exclusion limit found in the Run 2 analysis. The 5σ contour represents the projected limit for potential discovery. 115

INTRODUCTION

One of the most common, and often trickiest, questions I am consistently asked when someone hears I am working on my PhD in Physics is what kind of research I do. If I'm talking to someone else in physics, or someone who reads a lot about it, it isn't difficult to tell them that I do research at CERN and possibly describe the specific searches I've worked on if they show some familiarity with the field. However, when I'm in a conversation with someone I met in the gym, on a soccer field, at a family gathering, or sitting next to on a plane who has never heard of CERN and has no idea what particle physics is, it gets a bit more difficult. This is a field I started doing research in at the University of California, Santa Barbara in 2014 as an undergrad working with Dr. David Stuart as we investigated his idea to build a future subdetector with 4 mm by 4 mm silicon photomultipliers (SiPMs) and scintillating fibers. As I've spent more time immersed in the study of high energy physics, this question at times got increasingly difficult to answer. I wanted to describe in even deeper and more complete ways the research I was doing and the things I had learned, but that didn't usually land with someone who barely remembers their high school physics. Do I tell them about CERN and the 32 km circular accelerator, that we bring protons to nearly the speed of light and collide them at specific points inside a detector to study what comes out of the collision? Or maybe focus instead on how we probe higher and higher energies and try to better understand the conditions of the very early universe?

The answer I've come to give most often might be where I should have started all along, it comes from the question that first drew my interest to the field as a whole many years ago. The first time I was told there were even smaller particles inside of protons, that unlike electrons, protons aren't a fundamental particle, I asked that teacher what was inside. He was able to tell me they were quarks, but very little about them or how they worked. Having learned a significant amount about the inner workings of an atom, about the nucleus and electron cloud, and how electrons would populate distinct energy levels; being told that quarks existed, but almost nothing about what they were set me on path leading to writing this thesis now. So when I get this question about my research, I now tell people that I study the fundamental building blocks of matter and the universe. I'll describe how I want to understand the smallest and simplest pieces of matter that combine in unique ways to create every building, machine, toy, piece of art, planet, and star that you can see around you. It was my original motivation to start reading and watching videos about particle physics and, for now at least, it's the best way I have found to convey the motivations of my research to people who aren't familiar with physics.

I mention this in part to give some insight into my motivations for joining this field as well as to hint at the process I've gone through to learn the, often difficult, skill of maintaining a view of the big picture while getting involved in increasingly detailed work. I also wanted to point out my undergraduate reaserch with Dr. Stuart because it was in his lab that I developed a love for hardware electronics. I learned an incredible amount from him about the research process and realized I wanted to continue on to do a PhD. In fact, in my very first trip to Philadelphia to visit the University of Pennsylvania after being accepted, I told every professor I spoke to in the ATLAS group that I wanted to keep working on hardware and asked if they had work going on here that was related. All four professors immediately told me that I had to come to UPenn and about how incredible their hardware group was. Having grown up in California and having several options for graduate school on the west coast, UPenn was not where I thought I was going to end up. By the end of that visit, I couldn't imagine turning down Penn to go anywhere else. I started at the University of Pennsylvania in August 2016 and I have never once doubted that choice.

The remainder of this introduction will mirror the order of the sections in this thesis, as well as roughly my time at Penn chronologically, first discussing my early time at Penn as well as hardware and operations work on the Transition Radiation Tracker. Then presenting some background information on the two major physics analyses I had major roles on following that.

Transition Radiation Tracker

I spent my first year focusing primarily on coursework and teaching, including TAing a hardware electronics lab with Dr. Joe Kroll. During that year I also started looking through some of the documentation about the Transition Radiation Tracker (TRT) and meeting with my advisor, Dr. Hugh Williams (Brig), to talk about some of those papers. I spent the summer of 2017 at CERN working on the TRT, a straw detector that is part of the ATLAS Inner Detector. The TRT provides electron identification and tracking information for ATLAS as one of the subsystems at the very core of the detector as well as providing triggers to the rest of the detector while taking cosmic data. The TRT can also detect transition radiation from high energy electrons and gives a trinary readout to identify both "high" and "low" level hits indicating the presence of transition radiation and an electron without transition radiation respectively. The TRT front end electronics accelerate the 40 MHz clock from ATLAS to a 320 MHz clock that allows for single nanosecond "effective timing".

Over my fist summer I became a member of the TRT DAQ team and have been a part of it my full time at UPenn since. We have usually had a DAQ team of about 4-6 students and post docs over the years. Early on I learned a huge amount from Dr. Christopher Meyer and then graduate students (all doctors now) Khilesh Mistry, Bijan Haney, and Elodie Resseguie. I got to work closely with Dr. Shion Chen, Ian Dyckes, Jeff Shahinian, Nadezhda Proklova, and Daniil Ponomarenko on the TRT as well. In later years I had the opportunity to help bring Gwen Gardner and Lauren Osojnak onto the team as well. I have spent a lot of my time in graduate school working on the TRT, handling day to day operations, studying data compression schemes, running investigations into new problems that arise, and diagnosing and repairing electronics boards, mostly patch panels, that malfunciton.

Much of my time spent testing, debugging, and repairing boards while working in our test stands at CERN will go undocumented in this thesis, not because it wasn't fulfilling, important, or a good learning experience, but the work doesn't lend itself to being presented in a form like this. The TRT has a limited rate at which it can send data out of the detector to ATLAS to be used later to reconstruct the events it is recording. As the collision and trigger rates increased over the years, this meant we were unable to send out every bit that was recorded by the detector. A compression scheme had to be developed, essentially finding a way to upload the same information, but in a form that is made up of less actual space in the form of data. The first way to achieve this is to identify the most common patters that we see in the data and define code words, that are much shorter, in order to replace that pattern to shorten the overall length. My ATLAS qualification task was to study the compression schemes that had been documented by Ian Dyckes and explore any changes that would be necessary for the TRT to make while preparing for operations in Run 3. With Run 3 the LHC would deliver higher pile up (the number of collisions expected per instance when two bunches of protons pass each other at a collision point) than in Run 2 and simulating how this would impact the occupancy (what percentage of the TRT is 'lit up' and identifying that it has detected a charged particle) of the TRT and data compression methods we needed to employ was necessary to ensure a smooth transition. A lossy compression scheme had been developed but never implemented in earlier years due to firmware constraints. In my studies detailed in Chapter 3, I determined that the lossless compression scheme we had been using, Huffman encoding, would be sufficient for the next run, though there were a few changes that would need to be made related to how the zero word was defined. Now a couple of years into Run 3, the transition has been smooth and the TRT has been highly successful.

One of the other major investigations during my time working on the TRT has been understanding and trying to either fix or minimize a resynchronization error, specifically "lock" errors, that have been very disruptive at times. This investigation has proved to be very difficult and has lasted most of my time on the TRT. An in depth discussion of these studies is included in Section 2.4. One of the most challenging, and sometimes perplexing, parts is that we have never been able to recreate this particular error outside of the combined ATLAS partition while taking data. It has sat in a sweet spot where it is just uncommon enough to be difficult to study while sufficiently common to cause enough dead time in the detector that it needs to be addressed. These errors first presented very early during my time on the TRT, late in Run 2. I helped as older studesnt Khilesh and Bijan led the early stages of investigations to determine the cause of the errors. A series of tests were performed to identify the cause of the errors. We found that there did not appear to be a single cause or board at fault, that there were specific pairs of RODs and ROD patch panels that together either created or worsened the problem.

Between Run 2 and Run 3 we worked with the Penn hardware group to develop a "phase shift" board that would be used to further study the specifics of these errors. During 2021, when I was able to return to CERN, I took a leading role in this investigation. Over several weeks of testing and communication with the experts at Penn we were able to run in depth tests of many of the TRT ROD patch panels, though we still could not reproduce the specific errors in either of our test benches. We were able to test how robust the ability of the ROD and ROD patch panels to stablize the clock using the QPLL chips was. Over the years the TRT DAQ team has developed mitigation techniques to minimze these errors, but we have never been able to pin down the exact situations that cause them or find a complete fix to them. With the mitigation techniques the TRT has still been one of the best performing subsystems on ATLAS and has maintained very low dead time throughout Run 3.

Run 2 Fully Hadronic Analysis

I was involved in small roles on some analyses early on that I won't describe, but later in Run 2 I started working on a SUSY search with Dr. Shion Chen, Rachael Creager, Dr. Joe Kroll, and Dr. Brig Williams. A "SUSY" search generally is looking for a supersymmetric particle coming from a collision in the detector. In this search we were looking primarily for Winos, Higgsinos, and Binos the supersymmetric partner of the W-boson, Higgs-boson, and the $\mathrm{U}(1)_Y$ gauge field corresponding to weak hypercharge which will be further detailed in Chapter 1 and Section 5.1. The key to this analysis was that it focused on fully hadronic final states. Focusing on these fully hadronic states allowed us to take advantage of the very large branching ratios from the W, Z, and h boson to quarks allowing for sensitivity to higher mass SUSY particles. When these bosons decay to quarks, the particle sprays are often more difficult to manage and reconstruct the decay than it is for leptonic decays. Advances in reconstruction techniques, in particular the development of "large-radius" jets and improvements to boson tagging methods were necessary to conduct this analysis.

With these improvements making the study possible, though we did not discover any SUSY particles, we were able to set some of the best limits to possible SUSY particle masses in ATLAS, being consistently sensitive to masses in the 800-900 GeV range and in some cases setting limits over 1000 GeV.

I primarily worked on the "boosted" team of the fully hadronic group with 6-7 other graduate students and post docs. In this context "boosted" refers to focusing on an initial decay coming from a particle that is travling at a high speed, so it has a high kinetic energy. We worked alongside a group doing a non-boosted analysis, sharing developments and ideas while pursing separate final analyses. My primary area of contribution to the analysis was on some specific background estimations. I worked on truth level Monte Carlo study focusing on $t\bar{t}$ backgrounds initally. Later on, as Rachael Creager was finishing at UPenn, she taught me some of the methods she had developed and I used them to run a more in depth estimation of the QCD multi-jet background. I kept working with the team up to the final publication and helped with language edits for the final draft. An in depth discussion of this analysis is in Chapter 4 with subsections 4.5.1 and 4.5.1.1 detailing some of my specific work.

HL-LHC Extrapolation

After the unblinding and publication of the Run 2 fully hadronic analysis, I took on a project to extrapolate the study to run conditions that are expected in the HL-LHC in the future discussed in Chapter 5. While working on this extrapolation study I worked with a much smaller group, getting help from Dr. Shion Chen and Dr. Jeff Shahinian while being advised by Dr. Joe Kroll and Dr. Brig Williams. I used the same methods and estimations used by the Run 2 team to conduct the analysis. When possible I used the same Monte Carlo data that had been used and in some cases had to use the same methods to generate higher mass data sets to account for the improved reach of the extrapolation. The largest change for this extrapolation is the projected amount of data, going from an integrated luminosity of 140 fb^{-1} in Run 2 to an expected 3 ab^{-1} for the HL-LHC. During this extrapolation we also had to use or develop methods to account for increases in the center-of-mass energy of the collider and how that impacts cross sections for both signal and background events.

This extrapolation study should serve as strong motivation for a group to conduct a very similar search to the one from Run 2 once HL-LHC data is available. In the extrapolation we were able to predict increases to the mass sensitivity set by the Run 2 analysis ranging from 55% to 95% depending on the model, in some cases predicting a mass sensitivity as high as 1700 GeV. In the Run 2 analysis the fully hadronic group could only consider signal regions that included either four light quarks or two light quarks and two b-quarks in the final state in order to maintain orthogonality with a separate analysis focusing on the four b-quark final state. The extrapolation study was able to include this four b-quark final state so depending on the organization of analyses when HL-LHC data is being studied this inclusion may or may not be possible. I belive the robust nature of the extrapolation is strong motivation for a single analysis covering both signatures.

CHAPTER 1

THEORETICAL FRAMEWORK

1.1 Introduction to the Standard Model

The Standard Model of particle physics (SM) describes the elementary particles, fundamental forces, and their interactions in our universe. It is a non-abelian gauge theory that is invariant under the $SU(3) \otimes SU(2) \otimes U(1)$ unitary groups. The known particles are grouped into three categories: fermions (which can be subdivided), gauge bosons, and the Higgs Boson. Three of the four fundamental forces are described by the standard model: electromagnetic, weak, and strong, omitting gravity. The SM has predicted many physical pheomena and properties (such as mass ratio of Z and W bosons) to a high degree of accuracy and has been well tested and heavily agreed upon. The SM was built over several decades beginning in the 1920s with the first use of Quantum Field Theory (QFT) to describe electrodynamics. During the 1950s and 1960s theory was devolped for various pieces of the SM including explanations of the strong interaction, showing parity is not conserved in the weak interaction, and incorporating the Higgs mechanism into electroweak theory. In the mid 1970's Quantum Choromodynamics (QCD) aquired its modern form and the combination of all of these theories was first termed the Standard Model.

The known elementary particles are:

- Fermions: These make up the matter in the universe. They are spin 1/2 particles and can be subdivided into quarks and leptons by their interaction under $SU(3)$. Quarks carry color charge and interact while

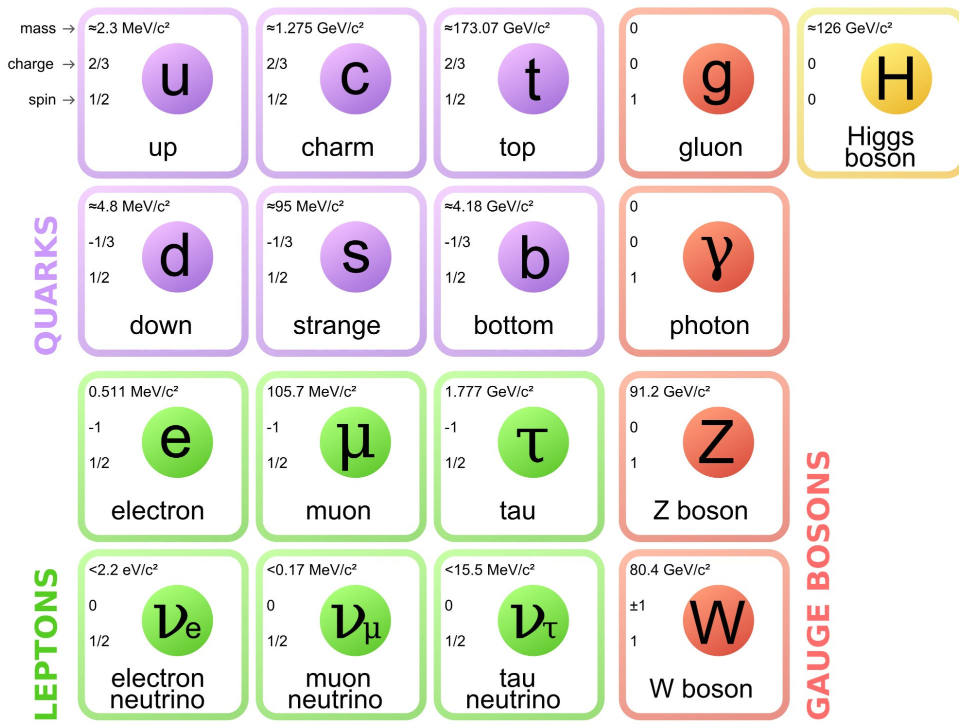

Figure 1.1: A visualization of the Standard Model of Elementary Particles.

leptons are colorless and do not interact. Both of these types of particles are further divided into 3 generations where each subsequent generation shares the same properties as the previous but with a higher mass. There is also an anti-particle for each particle discussed here that has the same properties except the opposite electric charge.

- Quarks include up-like quarks (up, charm, and top) which have a charge of 2/3 and down-like quarks (down, strange, and bottom) with a charge of -1/3.
- Leptons include the charged leptons: electron, muon, tau, which all share a charge of -1 and the neutrinos: ν_e, ν_μ, and ν_τ, which are all chargeless.

- Gauge Bosons: These are the force carriers that mediate interactions and are all spin 1 particles. They include the $W^{\pm}$ and Z^0 which mediate the weak force, the photon which mediates the electromagnetic force, and the gluon which mediates the strong force.
- Higgs Boson: The Higgs boson is an excitation of the Higgs field and has a spin 0. It breaks the

electroweak (EWK) symmetry allowing mixing of the EWK gauge bosons which results in the $W^{\pm}$ and Z^0 gauge bosons. This also gives mass to the fermions and gauge bosons while still respecting gauge invariance.

Under QCD each quark has a color charge, C, by which gluons mediate interactions. Gluons can also self-interact and are "confined" by their color (red, green, or blue). This confinement means that no colored composite particle can exist in nature, they must be colorless so quarks must enter bound states which are called hadrons. There can either be three quarks, one of each color, to form a baryon or one quark and one anti-quark to form a meson. The most plentiful baryons are protons (uud) and neutrons (udd). One example of a meson is the π^- formed be a down quark and an anti-up quark (d$\bar{u}$). All resulting hadrons will then have an integer electric charge. Gluons are a combination of two colors or two anti-colors. Leptons are colorless and unaffected by the strong force.

The strong force fundamentally is what holds the vast majority of matter together, both causing the formation of hadrons from quarks as well as binding hadrons (protons and neutrons primarily) within the nucleus of an atom. With the resulting electrically charged particles, the electromagnetic force can in turn create much more complicated structures that we see in everyday life.

Under quantum electrodynamics (QED) positive and negative charges interact via the photon which is both chargeless and massless. The electromagnetic force (also called the Lorentz force) describes the force exterted on electrically charged particles that are either stationary or moving through an electromagnetic field. This is the easiest force to observe of the three discussed in this document. It is responsible for the vast majority of forces we feel or affect our everyday life. Everything from keeping electrons in the orbit of an atom, to friction, elasticity, normal force, holding solid materials together, and, most obviously, the behavior of a compass in earth's magnetic field or two magnets repelling and attracting one another. The electromagnetic force acts on all charged particles, including hadrons that are non-zero charge, and leptons that are electron-like. Neutrinos are unaffected by the electromagnetic force.

Neutrinos are only affected by the weak force, which is the weakest of the three forces (as the name suggests). The mediators of the weak force are the $W^{\pm}$ and Z^0 bosons, all of which are massive. The weak force is primarily responsible for beta radiation. It is the only force that allows for flavor changing, where a quark can become a different type of quark via a $W^{\pm}$ boson. This change in flavor can cause a proton to become a neutron or vice versa and results in the before mentioned beta radiation. This means the changing of one element to another via the exchange of a neutrino with a neutron resulting in a proton and an electron. The weak force is then responsible for nuclear fusion which is what causes stars to burn and could one day provide abundant energy on earth. The same way that the electromagnetic force conserves electric charge and the strong force conserves color charge, the weak force conserves weak isospin.

The final SM particle, the Higgs boson, is the most recently discovered, is neutrally charged, has a mass of 125.10 ± 0.14 GeV, and is the only spin 0 elementary particle. The Higgs mechanism, which will be addressed in the next section, is what gives all other elementary particles their mass.

1.2 The Higgs Mechanism

As stated in the previous section, the $W^{\pm}$ and Z^0 are all massive particles. However, SU(2) gauge invariance which describes the weak force actually yields massless gauge bosons akin to the photon. Any terms that would give the gauge bosons mass would violate the local symmetry. This discrepency between theory and observation can be explained based on a breaking of local symmetry. It is a spontaneous breaking of the symmetry of electroweak theory and is called the Higgs mechanism.

A spontaneous breaking of the symmetry means there is no explicit term which breaks the symmetry, but instead there is a ground state of a new field from which mass terms will arise. This field is called the Higgs field and is a complex scalar field. We first define our Lagrangian:

$$\mathcal{L} = (\partial_\mu \phi)^\dagger (\partial_\mu \phi) - \mu^2 \phi^\dagger \phi - \lambda (\phi^\dagger \phi)^2, \tag{1.1}$$

with a complex scalar field:

$$\phi = \frac{1}{\sqrt{2}}(\phi_1 + i\phi_2). \tag{1.2}$$

We will now introduce an SU(2) phase transformation:

$$\phi \rightarrow \phi^{'} = e^{i\alpha(x)}\phi \tag{1.3}$$

In order to achieve local invariance we must also replace ∂_μ with the covariant derivative:

$$D_\mu = \partial_\mu + ieA_\mu. \tag{1.4}$$

After substituting these into the lagrangian, with a little work, we can obtain in terms of the real scalar fields ϕ_1 and ϕ_2:

$$\mathcal{L} = \frac{1}{2}(\partial_\mu\phi_1)(\partial^\mu\phi_1) + \frac{1}{2}(\partial_\mu\phi_2)(\partial^\mu\phi_2) - \frac{1}{2}\mu^2(\phi_1^2 + \phi_2^2) - \frac{1}{4}\lambda(\phi_1^2 + \phi_2^2)^2. \tag{1.5}$$

At this time we would like to look at the vacuum expectation value by finding the values of ϕ_1 and ϕ_2 which minimize the potential of the lagrangian. This requires that $\lambda > 0$ in order to have a finite potential. If we choose $\mu^2 > 0$ then the minimum lies at $\phi_1 = \phi_2 = 0$. However, if we choose $\mu^2 < 0$ we see the potential called the "Mexican hat potential" that we see in figure 1.2. This potential is rotationally symmetric having an infinite set of minima following the equation:

$$\phi_1^2 + \phi_2^2 = \frac{-\mu^2}{\lambda} = v^2. \tag{1.6}$$

The rotational symmetry is broken when a direction is selected. Conventionally $\phi_1 = v$ is chosen so $\phi_2 = 0$. Then the complex scalar field can be expanded about the minima using pertubation theory. From this we can find $m = \sqrt{2\lambda}v$.

If this method is carried out on the electroweak lagrangian with a scalar field in $SU(2) \otimes U(1)$ it would yield a neutral field with a massive gauge boson, the Z, a charged field with 2 massive gauge bosons, $W^\pm$, and the massless photon would be preserved. This also gives a ratio of W to Z mass which has been confirmed through high precision measurements at the LHC.

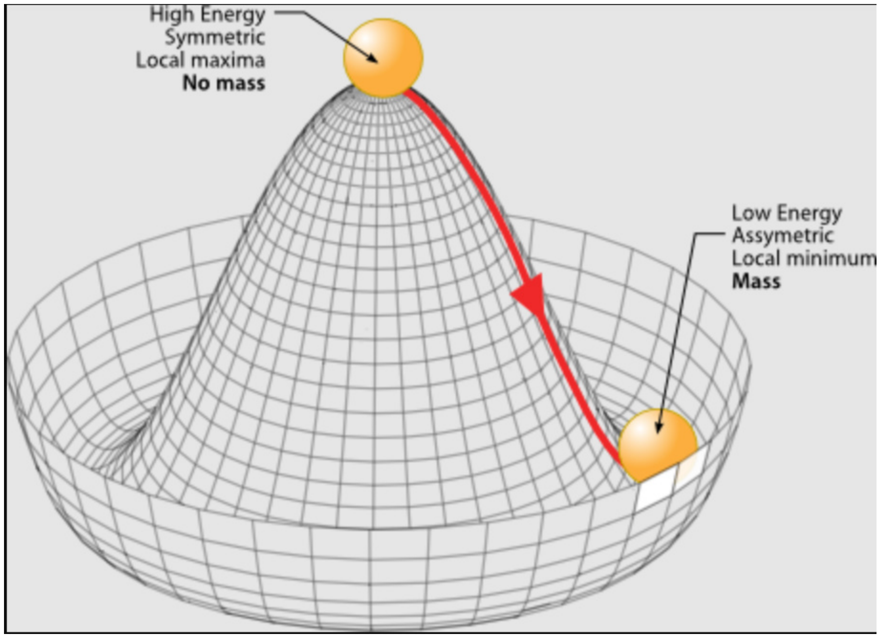

Figure 1.2: A visualization of the Higgs potential when $\mu^2 < 0$ which resembles a ”Mexican hat”. This shows the minimum energy is not at the center. This presents an asymmetry because the ball could roll down any direction on the hill and the symmetry is spontaneously broken when a ϕ is chosen. This broken asymmetry gives mass to the weakly interacting bosons.

1.3 Beyond the Standard Model

The discovery of the Higgs Boson “completed” the Standard Model in its current form. This form has been hugely successful in describing our physical world and predicting a various phenomena, mass ratios, branching ratios, etc. But the SM is still an incomplete theory. It gives no mention of the fourth fundamental force, gravity. To this point General Relativity (GR), which describes gravitational interactions, has not been reconciled with the SM. For subatomic interactions gravity is incredibly weak compared to the other 3 forces but on a much larger scale this is not the case. Astronomical observations have shown that the matter we can see is only a small portion of the energy and mass in the universe. Without the ability to “see” (they do not interact electromagnetically) these have been named dark matter and dark energy.

Measurements of the rotation of galaxies, the movement of stars and gas within galaxies, and gravitational lensing are all indirect proof of dark matter. This is some massive particle(s) that do not interact electromagnetically but do interact gravitationally. This matter is currently predicted to make up 27% of

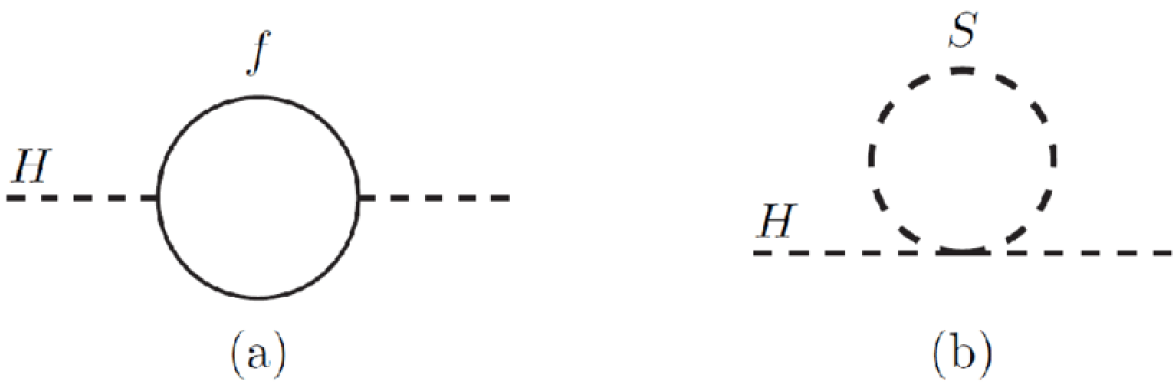

Figure 1.3: Fermionic loop correction to the Higgs Boson mass

the matter and energy in our universe. Dark matter is predicted to make up an even greater portion, it is closer to 68% of our universe. Dark energy is known for driving the expansion of the universe. First evidence came from a Type 1A supernovae. The light from this was weaker than expected because of the rate of expansion of the universe. This leaves only 5% of the universe that is made up of the matter that we observe.

A second unexplained phenomena of the universe is the matter-antimatter asymmetry. Our universe is made up of quarks and leptons instead of anti-quarks and anti-leptons. The theory predicts a symmetry of matter and antimatter, however we live in a universe that is composed of matter. There is no explanation for the favoring of matter in the SM.

Last, are questions about the Higgs itself. We talk about these question in terms of "naturalness" and "fine tuning". This is also referred to as the "hierarchy problem" and involves radiative corrections to the Higgs mass. These corrections can be orders of magnitude larger than the Higgs itself. For example, in figure 1.3 we can see these radiative corrections. On the left is the Dirac fermion loop which yields the equation:

$$\Delta m_H^2 = -\frac{|\lambda_f|^2}{8\pi^2}\Lambda_{UV}^2 + ... \tag{1.7}$$

where Λ_{UV}^2 regulates the loop integral. If we choose this to be on the order of the planck mass, this will yield a correction to the Higgs mass that is 36 orders of magnitude greater than the mass itself. This brings up "fine tuning". This idea is that in order to cancel different terms some parameters would need to be finely tuned to very specific values in order to get the observed $m_H = 125$ GeV. These shortcomings suggest there is a deeper theory or greater symmetry we can consider that may answer at least some of the problems. This section describes a symmetry known as supersymmetry which attempts to address some of these unanswered questions.

1.3.1 Supersymmetry

Supersymmetry (SUSY) is a theoretical extension to the standard model that has the potential to explain some of these pieces. In this thesis we will primarily be describing the Minimal Supersymmetric Standard Model (MSSM). SUSY in its entirety is incredibly complex so considering a version with the addition of minimal new particles and interactions while remaining internally consistent is advantageous. In simplest terms SUSY is a new symmetry that relates bosons and fermions through an operator, Q. This operator turns bosons into fermions and fermions into bosons by changing their spin between integer and half-integer values.

$$Q|Fermion\rangle = |Boson\rangle, Q|Boson\rangle = |Fermion\rangle \tag{1.8}$$

SUSY predicts additional particles, one “superpartner” for each SM particle. The superpartners of the fermions are collectively referred to as “sfermions” and the individual sfermions follow the same naming convention. This means we have squarks (sup, sbottom, scharm, sstrange, stop, and sbottom) and sleptons (selectron, smuon, stau, sneutrinos). The superpartners of the bosons are identified by adding “-ino” to the end. This gives us gauginos from the gauge bosons (Wino and Bino), higgsino for the higgs, gluinos, and gravitino. SUSY particles are all denoted with a tilde above its SM symbol, for example $\tilde{q}$, $\tilde{e}$, $\tilde{W}^{\pm}$, $\tilde{g}$.

A table of the MSSM chiral and gauge supermultiplets is shown in figure 1.4.

This change in quantum numbers would solve the hierarchy problem without the need for any fine tuning if the superpartners had the same mass as their SM partners. It would create cancelations in the Higgs mass equations eliminating the terms that are magnitudes greater than the Higgs mass itself. However, it is easy to tell experimentally that these SUSY particles do not share the same mass as their partners.

Chiral supermultiplets			
Names		Spin 1/2	Spin 0
Quarks, squarks	Q	(u_L, d_L)	$(\tilde{u}_L, \tilde{d}_L)$
3 generations	$\bar{u}$	$\bar{u}_{\mathrm{L}} = (u_{\mathrm{R}})^{\mathrm{c}}$	$\tilde{\bar{u}}_{\mathrm{L}} = \tilde{u}^{\dagger}_{\mathrm{R}}$
	$\bar{d}$	$\bar{d}_{\mathrm{L}} = (d_{\mathrm{R}})^{\mathrm{c}}$	$\tilde{\bar{d}}_{\mathrm{L}} = \tilde{d}^{\dagger}_{\mathrm{R}}$
Leptons, sleptons	L	$(\nu_{\mathrm{L}}, e_{\mathrm{L}})$	$(\tilde{\nu}_{\mathrm{L}}, \tilde{e}_{\mathrm{L}})$
3 generations	$\bar{e}$	$\bar{e}_{\mathrm{L}} = (e_{\mathrm{R}})^{\mathrm{c}}$	$\tilde{\bar{e}}_{\mathrm{L}} = \tilde{e}^{\dagger}_{\mathrm{R}}$
Higgs, Higgsinos	H_{u}	$\left(\tilde{H}^{+}_{\mathrm{u}}, \tilde{H}^{0}_{\mathrm{u}}\right)$	$\left(H^{+}_{\mathrm{u}}, H^{0}_{\mathrm{u}}\right)$
	H_{d}	$\left(\tilde{H}^{0}_{\mathrm{d}}, \tilde{H}^{-}_{\mathrm{d}}\right)$	$\left(H^{0}_{\mathrm{d}}, H^{-}_{\mathrm{d}}\right)$

Gauge supermultiplets		
Names	Spin 1	Spin 1/2
Gluinos, gluinos	g	$\tilde{g}$
W boson, Wino	$W^{\pm}$,W^{0}	$\tilde{W}^{\pm}$, $\tilde{W}^{0}$
B boson, Bino	B	$\tilde{B}$

Figure 1.4: Supermultiplets in MSSM. Chiral supermultiplets are included here for completeness but are outside of the scope of the rest of this thesis.

For example, a 511 keV selectron is simple to rule out. This means the symmetry must be broken to give the superpartners greater masses. It is assumed that something akin to the spontaneous breaking of the electroweak symmetry, which gives the W and Z bosons mass, also exists here. We also assume that it is broken softly, so the mass difference between the SM and SUSY partners aren't too large. This is chosen such that the hierarchy problem can be solved with minimal fine tuning.

Just as the spontaneous symmetry breaking of the electroweak allowed for the $W^{\pm}$, W^{0}, and B bosons to mix, the spontaneous breaking of SUSY will also allow mixing of the supersymmetric partners of the gauge bosons. This mixing yields 6 observable states: 4 neutralinos (neutral mixes of the gauginos) and 2 charginos (charged mixes of the gauginos). These mixed states are denoted by a $\tilde{\chi}$ which are labeled in ascending order by mass:

$$m_{\tilde{\chi}^0_1} < m_{\tilde{\chi}^0_2} < m_{\tilde{\chi}^0_3} < m_{\tilde{\chi}^0_4}, m_{\tilde{\chi}^{\pm}_1} < m_{\tilde{\chi}^{\pm}_2} \tag{1.9}$$

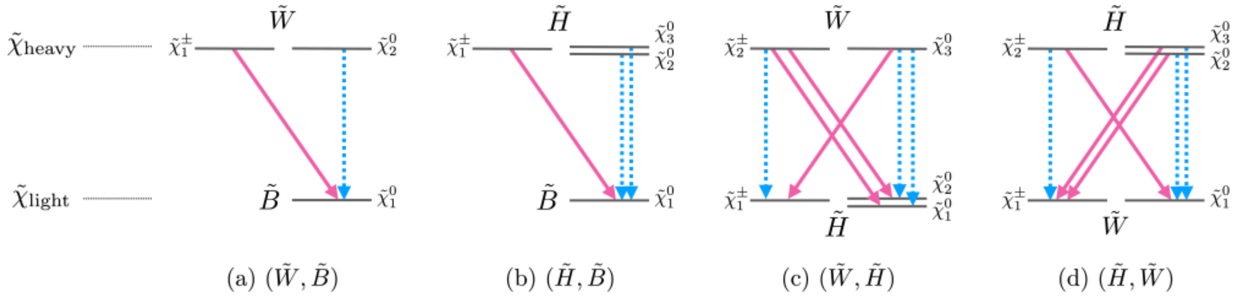

Figure 1.5: The electroweakino mass spectra and corresponding mass eigenstates in each model in the bino/wino/higgsino LSP scenario. The solid (dashed) arrows represent the decay modes emitting a W (Z or h) boson. A W boson is generated when a chargino decays into a neutralino or vice versa; a Z or h boson is emitted when a chargino decays into a chargino or a neutralino decays into a neutralino. Figure credit to Dr. Shion Chen.

1.3.2 Electroweakly-Produced Supersymmetric Particles

This thesis will present an HL-LHC extrapolation of a run 2 search for electroweakly-produced SUSY particles. This section will cover the physics scenarios in this search.

This search assumes a “split SUSY” scenario where some but not all gauginos are decoupled having masses much greater than 1 TeV. Specifically the electroweak gauginos are assumed to stay coupled. The 125 GeV SM Higgs and a naturalness argument motivate this choice. The particles in this search will be assumed to be MSSM-like. The lightest supersymmetric particle (LSP) is assumed to be the lightest neutralino unless specified to be the gravitino. This analysis will focus on electroweakinos with a large mass splitting, Δm=400 GeV $\sim$ 1 TeV. Electroweakino masses up to $\approx$1.5 TeV will be considered. The “heavy state” is either wino or Higgsino-like. The light state will then be Higgsino or wino-like respectively, or bino-like for either case of the heavy state. Naturalness favors a light Higgsino model but there will be 4 combinations considered in total:

$$(\chi_{\tilde{heavy}}, \chi_{\tilde{light}}) = (\tilde{W}, \tilde{B}), (\tilde{W}, \tilde{H}), (\tilde{H}, \tilde{B}), (\tilde{H}, \tilde{W}), \tag{1.10}$$

The target mass spectra are visualized in figure 1.5

CHAPTER 2

LHC AND THE ATLAS DETECTOR

2.1 The Large Hadron Collider

The Large Hadron Collider (LHC) [1] is the largest particle accelerator in the world which supports the largest scientific experiments in the world. It is a 27 km ring that crosses the Franco-Swiss border and sits 100 m underground. The LHC utilizes superconducting magnets and radiofrequency cavities to shape, bend, and accelerate beams of protons, and sometimes lead ions, to nearly the speed of light. There are 2 beams circulating in opposite directions at an energy of 6.5 TeV, so when collided they reach a center of mass energy of 13 TeV. These collisions take place at 4 interaction points where quadrapole superconducting magnets focus the beam to make it much denser in order to increase the number of interactions. Bunches of protons are collided evert 25 ns in the center of 4 experiments (ATLAS, CMS, ALICE, and LHCb).

The proton is a composite particle made up of 3 quarks (two up quarks and one down quark) and gluons which share its energy. This means that even though the bunches are at 13 TeV the actual collisions will only have some portion of that energy, the distribution is unkown but determined by parton distribution functions (PDFs). PDFs are probability densities for finding a given component particle to have a certain fraction of the momentum of the composite particle. The protons are first taken from a tank of ionized hydrogen gas. These protons are first accelerated in a linear accelerator, Linear Accelerator 2 (LINAC2), where they reach an energy of 50 MeV. There are then 3 circular accelerators that the protons pass through. First the Proton

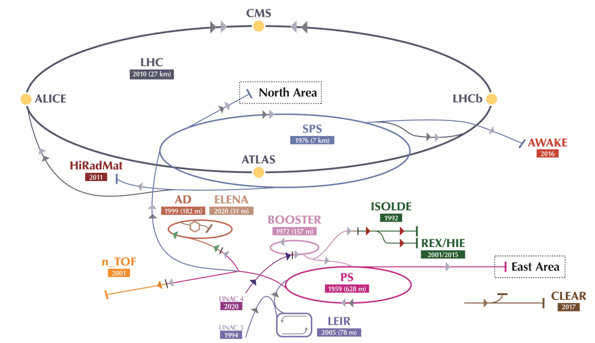

Figure 2.1: LHC accelerator complex

Synchrotron Booser (PSB), then the Proton Synchrotron(PS) and the Super Proton Synchrotron(SPS) where they reach energies of 1.4, 25, and 450 GeV respectively. Finally protons are injected into the LHC in two beams going in opposite directions where they are brought up to an energy of 6.5 TeV to be ready for collisions. The schematic for the full accelerator complex is seen in figure 2.1.

Within the LHC beam pipe, proton bunches must pass through the RF cavities in phase with the oscillating electric field in order to be properly accelerated. This requires the electric field frequency to be an integer multiple of the revolution frequency, this integer is the harmonic number. The harmonic number determines how many locations (often called buckets) in the beam a bunch can be. For the LHC that number is 35,640, but in run 2 only 1 in every 10 buckets could be filled giving 3,564 buckets to utilize. The bunch structure or bunch pattern determines which of these buckets are filled, during run 2 only 2000-2500 were filled.

The proton-proton collisions in experiments such as ATLAS recreate conditions right after the Big Bang. This environment, where energy and mass are fluid, is ideal for studying the electroweak processes, the Higgs boson, and seeking out supersymmetric particles. The higher the center of mass energy, the closer to the instant of the Big Bang we can see. This makes the center of mass energy the most important quantity of the beams. The luminosity, or the collision rate per second, is vital as it determines the rate at which data can be taken.

2.1.1 Luminosity

The luminosity ($\mathcal{L}$) and the cross section of a process (σ) determine the rate at which those events are generated ($\frac{dN}{dt}$).

$$\frac{dN}{dt} = \mathcal{L} \cdot \sigma, \tag{2.1}$$

The luminosity is dependent on the number of protons per bunch N_p, the beam frequency f_{rev}, the bunches per beam which is denoted as n_b, γ the Lorentz factor, β^* the beta function, or how compact the beam is, and F, the geometric factor that accounts for the crossing angle of the beams:

$$\mathcal{L} = \frac{N_p^2 n_b f_{rev} \gamma}{4\pi\beta^* \epsilon} F \tag{2.2}$$

This is the instantaneous luminosity and is measured in units of $cm^{-2}s^{-1}$ or $nb^{-1}s^{-1}$. The LHC was designed to reach values of 1x$10^{34}nb^{-1}s^{-1}$ but was able to achieve values up to 2x$10^{34}nb^{-1}s^{-1}$. The luminosity is highest at the start of a run but will slowly decrease over time as protons collide and N_p decreases. The run is divided up into many luminosity-blocks (LBs) where the luminosity is approximately constant. When the luminosity gets too low that it is no longer economical to take data a beam dump is executed and the beams will then be refilled with a new set of protons for the next run.

One of the most important quantities is the integrated luminosity as it represents the total amount of data that was collected. This is just the integral of Luminosity with respect to time:

$$\mathcal{L}_{int} = \int \mathcal{L} dt \tag{2.3}$$

The total luminosity collected by ATLAS and deemed fit for physics analysis was 139 fb^{-1}. The luminosity collected for both run 1 and 2 data taking periods is shown in figure 2.2. The analysis that this extrapolation is based on was conducted and formed its results with the full 139 fb^{-1} of data. This extrapolation will be based on Monte Carlo (MC) simulations but will compare the projected results to those found in the run 2 analysis.

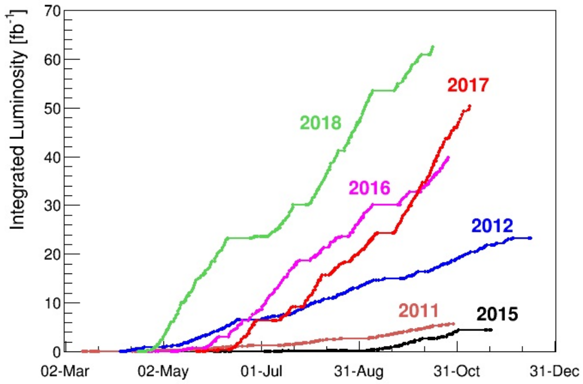

Figure 2.2: This shows the integrated luminosity over time for each year of data taking.

2.1.2 Pileup

There are many protons per bunch and as such there can be multiple interactions per bunch crossing, in fact we want to have many interactions as this increases the data taking rate as long as the detector can "keep up" with the accelerator. The number of collisions (or interactions) per bunch crossing is referred to the pileup (μ) which depends on the beam parameters. In ATLAS we define a quantity, $\langle\mu\rangle$, which is the average number of interactions per bunch crossing. There are 2 kinds of pileup, in-time and out-of-time pileup. In-time pileup is the overlap of other interactions in the same bunch crossing. Out-of-time pileup refers to interactions with other bunch crossings. Pileup can decrease the resolution of an event, cause track misreconstruction, create dead time in the detector due to the rate of processing events, and in general make reading out events more difficult. This creates a balance where a higher pileup corresponds to higher data taken for a given luminosity but it must be kept below critical values where many subdetectors begin to have trouble handling higher pileup.

2.2 The ATLAS Detector

ATLAS is a general-purpose cylindrical particle detector based at point 1 in Meyrin, Switzerland right next to the French border. It was primarily designed to find the Higgs boson as well as make high precision measurements of electroweak interactions and search for new physics beyond the SM. The detector was

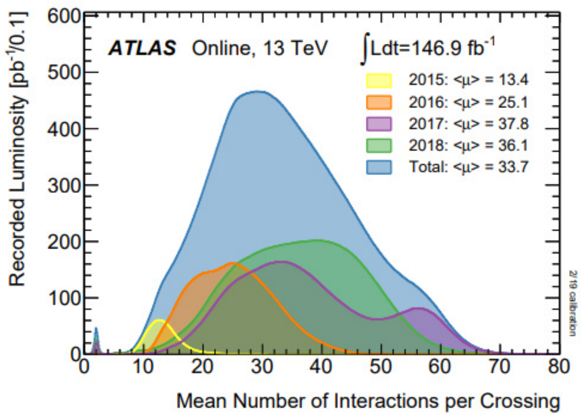

Figure 2.3: Run 2 average interactions per bunch crossing

designed to identify, measure, and reconstruct photons, electrons, muons, and hadronic jets. There is nearly 4π coverage from the ATLAS detector with a length of 44 meters and a height of 25 meters. There are 3 separate concentric systems: the Inner Detector (ID), Calorimeters, and Muon Spectrometer (MS). Each of these is made up of subdetectors that have a barrel system centered around the interaction point and an endcap system placed further on both the negative and positive z-axis. The ID is used to track all charged particles and includes the TRT, a subsytem that this thesis will pay special attention to as I have spent large portions of my time working on operations and maintenance of the TRT. The calorimeters are designed to stop electromagnetic and hadronic particles and measure their energy. Finally, the MS identifies and tracks muons.

A right handed coordinate system is used to describe ATLAS with its origin at the interaction point. The z-axis points down the beam pipe, the x-axis points toward the center of the accelerator, and the y-axis points up. Cylindrical coordinates are used in the trasverse plane where ϕ is the azimuthal angle around the z-axis with $\phi = 0$ points to the center of the LHC ring. The rapidity (y) or pseudorapidity (η) are used as the final coordinate. The rapidity and pseudorapidity of a particle are defined as:

$$y = \frac{1}{2}ln(\frac{E + p_z}{E - p_z}), \qquad \eta = -ln(\frac{\theta}{2}) \tag{2.4}$$

Where E is the energy and p_z is the momentum in the z-direction. The pseudorapidity is equal to the

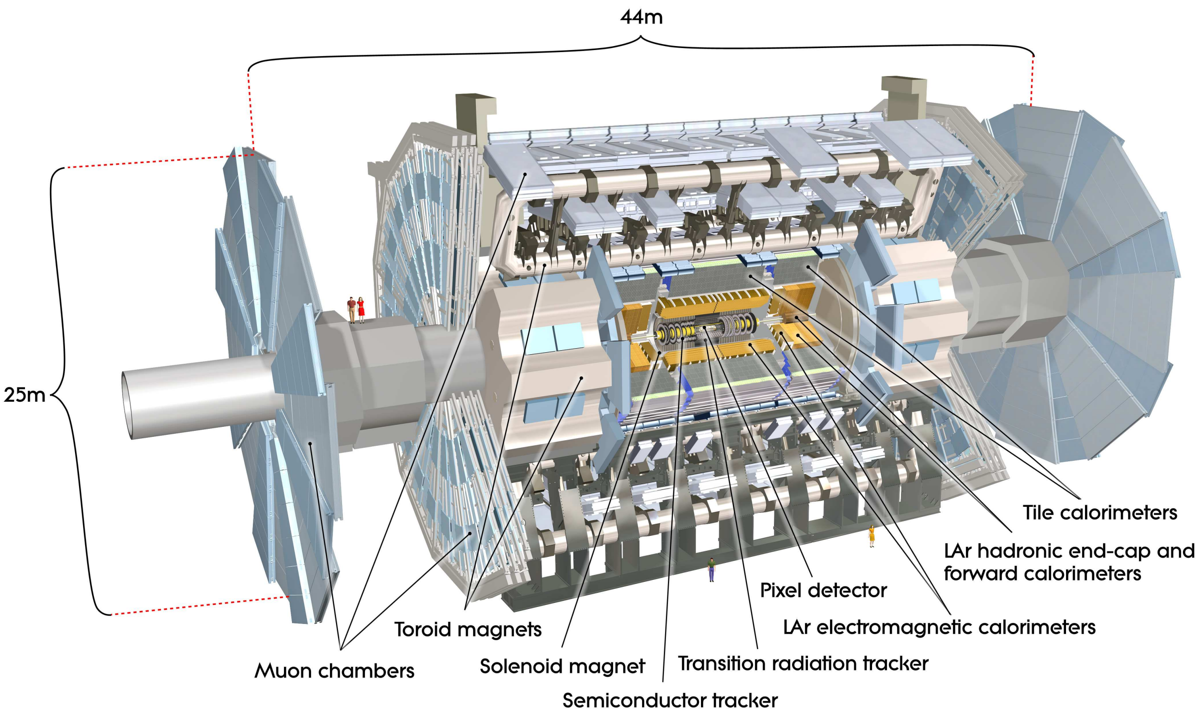

Figure 2.4: General cut-away view of the ATLAS detector [2].

rapidity in the limit where particles are considered massless. Both y and η are Lorentz invariant under boosts (θ is not) so angular distance is measured in units of:

$$\Delta R \equiv \sqrt{(\Delta\eta)^2 + (\Delta\phi)^2} \tag{2.5}$$

This transverse (x-y plane) is incredibly important because with partons colliding there's no way to know their momentum in the z direction, however it is known that the momentum in the x-y plane is zero.

2.2.1 The Inner Detector

The Inner Detector (ID) is the first part of the ATLAS detector to interact with a particle from any collision and is able to "see" all electrically charged particles. It serves the primary purpose of precisely measuring the trajectories (called tracking) of charged particles. There is a 2T axial magnetic field throughout the ID which allows measuring of the charge, momentum, and decay vertex. It covers a pseudorapidity of $|\eta| = 2.5$

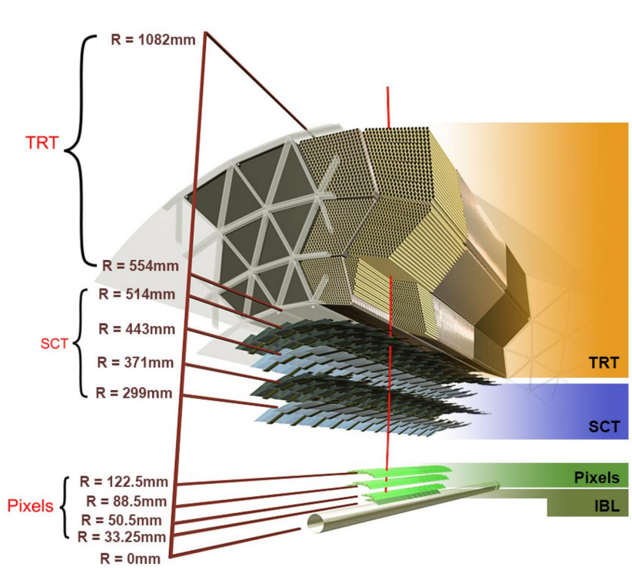

Figure 2.5: A cutaway showing the barrel section of the Inner Detector

and has a radius of about 1.1 m. The tracks from the ID are used directly or indirectly in the reconstruction of leptons, photons, and jets. It is also important for vertex reconstruction and missing transverse energy (MET) calculation. MET, often written E_T^{miss}, is the imbalance in energy in the transverse plane that can indicate the presence of invisible particles. The ID is made up of a high granularity pixel detector followed by a silicon microstrip tracker, then the outermost is the TRT, a straw tube tracker capable of measuring trasition radiation as well as electron identification. A cutaway of the barrel region can be seen in figure 2.5 and a schematic is shown in figure 2.6

2.2.1.1 Pixel Detector

The innermost layer of the pixel detector, the Insertable B-Layer (IBL) was inserted into ATLAS in 2014 during Long Shutdown 1 (LS1). The addition of it provided better resolution of the vertex and the transverse impact parameter (d_0) information. d_0 indicates the distance between the primary interaction vertex and the closest point of a particle track in the ATLAS detector. It is positioned R=33.25 mm away from the z-axis and has 8 million readout channels. Each pixel is 50 x 250 μm and provides a resolution for tracks of 8 μm in the x-y plane and 40 μm in the z direction. Beyond the IBL the pixel detector is made up of three

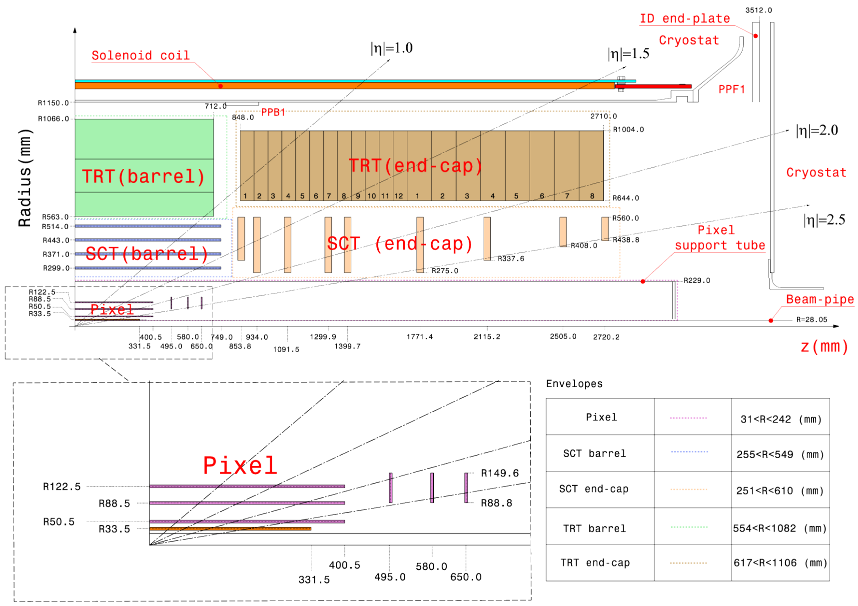

Figure 2.6: Full schematic of the inner detector

concentric, cylindrical barrels and three disk endcaps in total including over 80 million pixels. The barrel portions are at distances of R = 50.5, 88.5, and 122.5 mm and endcap disks sitting in the z direction at 495, 580, and 650 mm from the collision point.

2.2.1.2 Semiconductor Tracker

The Semiconductor Tracker (SCT) uses the same basic technology as the pixels, but with larger silicon "strips". There are 4 barrel layers and 9 endcap wheels on each side utilizing silicon microstrips that are 12cm long and have a pitch of 80 μm. This pitch elongates the silicon sensor which allows the SCT to cover a larger volume without having to increase the materials or the number of readout channels. The strips supply a hit resolution of 17 x 580 μm. There are a total of 768 strips contained on each of the 15,912 sensors, yielding 6.4 million readout channels.

2.2.1.3 Transition Radiation Tracker

The Transition Radiation Tracker (TRT) is a proportional drift straw tracker providing electron identification and tracking coverage up to η<2.0 as the outermost component of the ID. The TRT is made from 352,256 gas filled polyimide straws that are 4 mm in diameter. They are filled with a gas mixture of 70%, 27%, 3% xenon(or argon), carbon dioxide, and oxygen respectively. There is a 32 μm diameter gold-plated tungsten wire running down the center of each straw. A 1,500 volt potential is applied between the outer casing of the straw and the wire. Charged particles passing through the straws will ionize gas molecules causing them to then drift toward the outer casing while electrons drift toward the wire. There is an amplification of the signal by a factor of about 20,000 due to an avalanche of electrons as one approaches the wire. This allows timing information to be extracted and gives a 130 μm resolution of straw hits.

The TRT, as its name implies, can also detect transition radiation. There is a polypropylene-polyethylene fiber mat about 3mm thick between the straws. This has a different index of refraction than the gas mixtures or normal air so when a charged particle moves through the two materials there is a chance of producing transition radiation photons with energy proportional to its Lorentz factor. Electrons, with a lighter mass, have a higher Lorentz factor than muons, pions, and other charged particles so produce higher energy transition radiation. This photon will travel into the straws and excite not just the gas, but also charged particles. A larger signal is created by this type of radiation, so the TRT uses a trinary system that has both a low threshold to detect charged particles passing through straws as well as a high threshold to pick up the transition radiation. This is exploited to better aid in electron identification utilizing this high threshold.

More in depth information about the TRT, the data taking process, and compression schemes are covered in the next chapter.

2.2.2 The Calorimeters

Beyond the Inner Detector and solenoid there are two types of calorimeters. ATLAS uses one for measuring electromagnetically interacting particles and another for hadronically interacting particles covering the region with $|\eta| < 4.9$. These are the Liquid Argon (LAr) calorimeter and the Tile calorimeter respectively, both of which are sampling calorimeters. This means they have alternating layers of absorbers to induce showers and active layers that measure those showers. In order to get accurate measurements of trasverse energy it is vital that particles fully deposit their energy and electromagnetic and hadronic showers are fully contained

Figure 2.7: A picture showing both the SCT and TRT during production when the SCT is being placed in the center of the TRT.

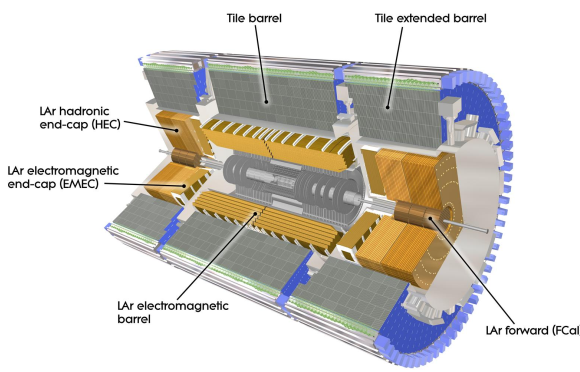

Figure 2.8: Cutaway view of the ATLAS calorimeters

within their respective calorimeters. To ensure this they must be sufficiently thick, at $\eta = 0$ the hadronic calorimeter is 11 interaction lengths λ_t thick and the EM calorimeter is 22 radiation lengths (X_0) deep. One interaction length is the mean distance between hadronic interactions and one radiation length is the average distance over which the energy of a particle is reduced by a factor of $\frac{1}{e}$. Together these systems measure the energy for all particles except muons, neutrinos, and possibly any long lived sparticles or BSM particles. A cutaway view of the calorimeter systems is shown in figure 2.8.

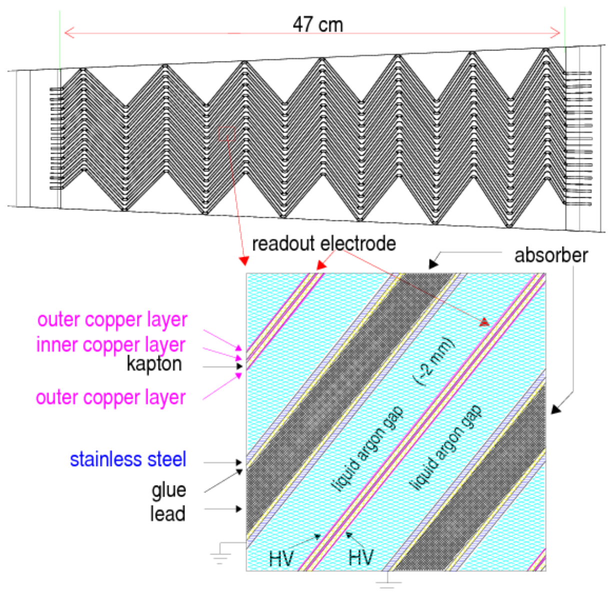

Figure 2.9: Zoomed in view of the lead, liquid argon layering of the LAr detector.

2.2.2.1 Liquid Argon Calorimeters

The Liquid Argon calorimeter (LAr) measures electromagnetically interacting particles, specifically electrons and photons, in the $|\eta| < 3.2$ region. The absorber layers are made out of lead for its heavy nucleus. Electrons interact with the lead emitting bremsstrahlung photons. Photons decay into e^+e^- pairs creating a narrow energy deposit and will once again interact with the lead continuing in this "showering" process. The active portions of the detector, which measure the energy, are made of liquid argon. It was selected for its linear response in energy and for its radiation hardness. A zoomed in view of the layering can be seen in figure 2.9

The LAr has a unique accordian geometry, pictured in figure 2.10, that gives it complete ϕ coverage without any cracks. This also allowed it to be made fully hermetic, allowing for pointing information of photons. It is divided into barrel sections ($|\eta| < 1.475$) and endcap sections ($1.375 < |\eta| < 3.2$). The endcaps are further subdivided into inner and outer wheels, divided at $|\eta| = 2.5$. For $|\eta| < 2.5$, the coverage of the inner detector, it is segmented into three layers. These layers have very fine granularity, the first layer has particulary fine granularity in the η direction to differentiate prompt photons from showers caused by neutral pions decaying into two collimated photons. The outer endcap wheels are segmented into two layers

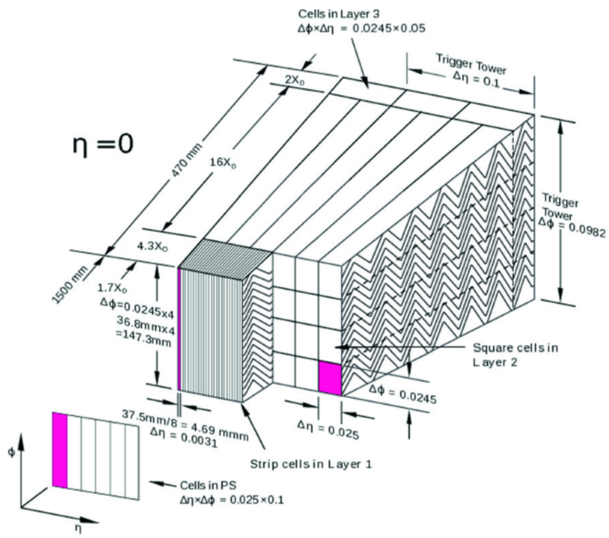

Figure 2.10: Schematic of LAr calorimeter near $\eta = 0$

and don't have as fine of a lateral granularity. The $|\eta| < 1.8$ region actually has an active layer of liquid argon before the first layer of the calorimeter. This helps to correct for energy lost before the calorimeter.

2.2.2.2 Tile Calorimeters

The Tile calorimeter provides coverage for hadronic showers in the region $|\eta| < 4.9$. It consists of three barrel layers and two endcap wheels. The absorber in the barrel region $|\eta| < 1.5$ is made of steel plates and the active material consists of plastic scintillating tiles. In the endcap regions $1.5 < |\eta| < 3.2$ a copper absorber is used with LAr as active material. And in the forward region $3.2 < |\eta| < 4.9$ LAr is still used as the active material but it utilizes copper/tungsten absorbers instead due to the larger radiation flux.

The readout is done on both sides of the tiles through fibers and into photomultiplier tubes. Hadronic showers decay through the strong interaction, mostly into showers of pions. These showers are generally much broader so the active material can have a lower granularity.

2.2.3 Muon Spectrometer

Muons typically pass through the ID and Calorimeters without depositing a significant portion of their energy. They will not be affected by the hadronic calorimeter as they are colorless. Having about 200 times

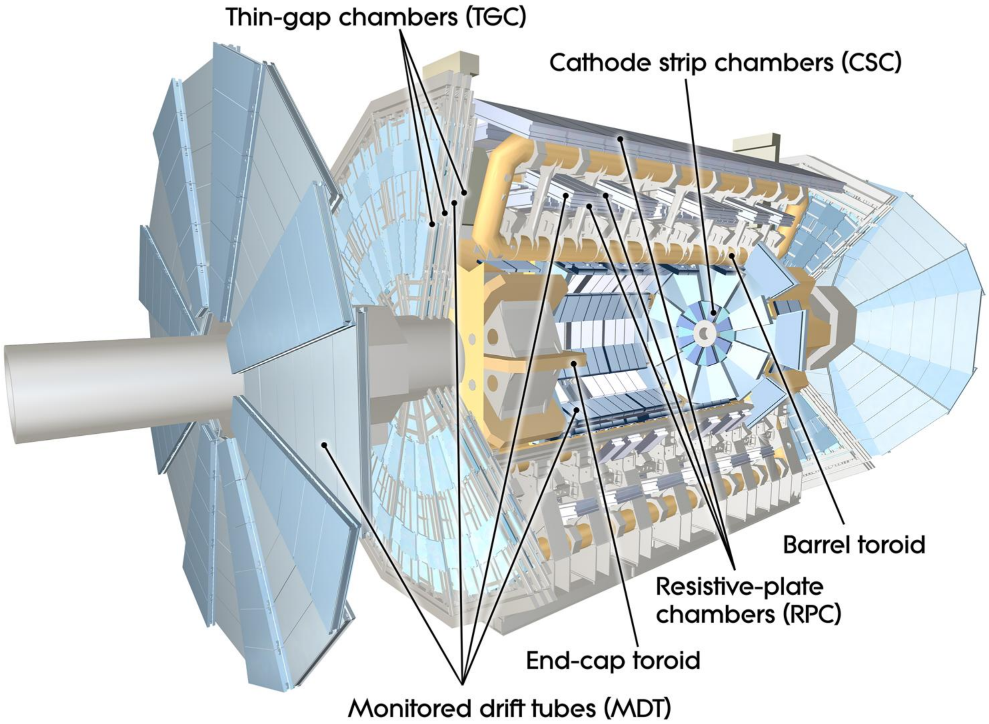

Figure 2.11: Schematic representing a quarter of the muon system.

the mass of electrons and minimally ionizing they will pass through the EM calorimeter losing very little energy. To obtain accurate measurements of Muon energy there is one more subsystem dedicated to this.

The outer most layer of the ATLAS detector is the Muon Spectrometer (MS), pictured in figure 2.11, which consists of two different tracking and triggering systems is the solution to this. The MS has a barrel region that covers $|\eta| < 1.05$ and an endcap system that reaches out from there to $|\eta| < 2.7$. It is the largest subsystem by volume and interspersed with the toroid magnet around the outside of the detector. The toroid's 0.5 T magnetic field fills the region bending the muons and allowing for measurements of the tracks that allow the calculation of muon p_T up to 3% precision.

There are three cylindrical layers of Monitored Drift Tubes (MDTs) in the barrel region that are used for tracking. Additionally, two outermost layers are surrounded by Resistive Place Chambers (RPCs) for triggering. MDTs are more or less bigger versions of TRT straws. They have a 3cm diameter and are filled with argon gas with a central tungsten wire. The potential between the tube and wire is held at 3,000 Volts

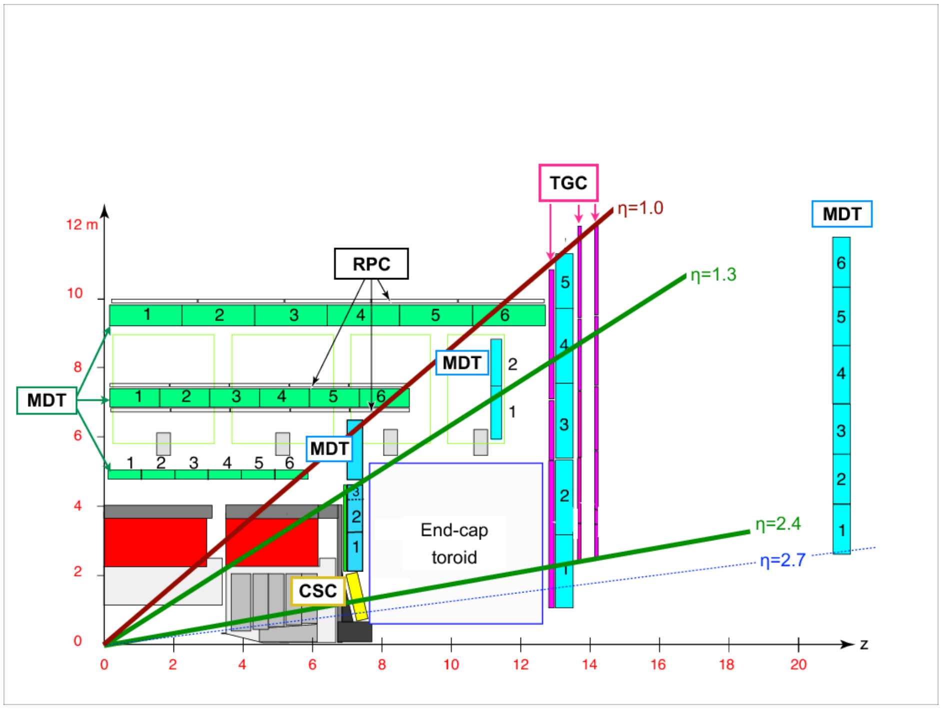

Figure 2.12: Cutaway image of the ATLAS muon system

and this works the same way the TRT does. When muons pass through the drift tubes they ionize the gas causing the electrons to drift to the central wire while the ion drifts to the outer shell. The MDTs can acheive a spatial precision of 80 μm. The RPCs that surround the two outer MDTs are sheet capacitors. They have 2mm gaps which are filled with $C_2H_2F_4$ gas and an electric field of 4,500 V/mm. Ionized electrons are read out from both sides of the RPCs and provide a timing resolution of 2 nanoseconds for the trigger.

The endcap regions additionally contain Cathode Strip Chambers (CSCs) are used in the high $|\eta|$ regions (2.5-2.7) where the MDTs experience too high of an occupancy due to the high flux of particles. These are like strip versions of MDTs with a higher granularity and have a precision of 60 μm. CSCs are made of proportional chambers with tungsten wires at 2,160 volts and lie perpendicular to readout strips. The endcap region also uses Thin Gap Chambers (TGCs) which have three layers surrounding the third wheel of the endcap. These are very similar to the CSCs except they operate with gold plated tungsten wires held at 3,100 volts. They provide a timing resolution of about 4ns. A schematic of one quarter of the muon system is seen in figure 2.12.

2.3 Object reconstruction

Digitized signals are read out from the various subdetectors of the ATLAS detector. These signals are used to identify tracks in the Inner Detector and muon system and energy measurements in the calorimeters as well as the muon system. From this information events are reconstructed based on signatures of various SM particles to create Physics objects such as leptons and jets with detailed information such as momentum or energy that can be used in analyses.

Electrons can be identified by the TRT and their tracks are mapped in the ID. They are also characterized by energy left in the EM calorimeter. Photons are also identified based on energy left in the EM calorimeter but, since they are chargeless, they don't leave tracks in the ID. Stable hadrons, neutrons and protons, leave very little energy in the EM calorimeter but deposit most of their energy in the hadronic calorimeter. Muons are tracked by both the ID and MS but deposit very little energy in either calorimeter. Neutrinos are invisible in the detector as they only interact weakly but can be identified by imbalances in energy, referred to as MET. Figure 2.13 shows a representation of some of these signatures for SM particles.

The boost in the z-direction of any collision is unkown as the momentum of individual partons are unknown, however the momentum in the transverse direction going into the collision is zero, so it must still be zero after the collision. Taking the negative of the vector sum of the momenta of all visible particles will yield missing transverse momentum (p_T^{miss}). The magnitude of this is then E_T^{miss}. This can be used to infer the presence of neutrinos or, in more exciting cases, new invisible particles.

Color confinement causes any colored particles to hadronize and produce sprays of color neutral particles, these are called jets. It is difficult to distinguish light flavor quarks (u, d, s) from each other and from gluons as they decay extremely quickly and their jets can look nearly identical. Heavier quark iniltiated jets can be better identified however. Top-quarks are very unique in that they decay weakly to b-quarks which then hadronize. B-quarks are associated with hadrons that have a slightly longer lifetime and can travel a few mm from the interaction point before hadronizing. This means the jet vertex can allow identification of b-jets, and to a lesser extent jets from c-quarks.

These reconstructed objects have a very detailed set of properties associated with them. Physics analyses

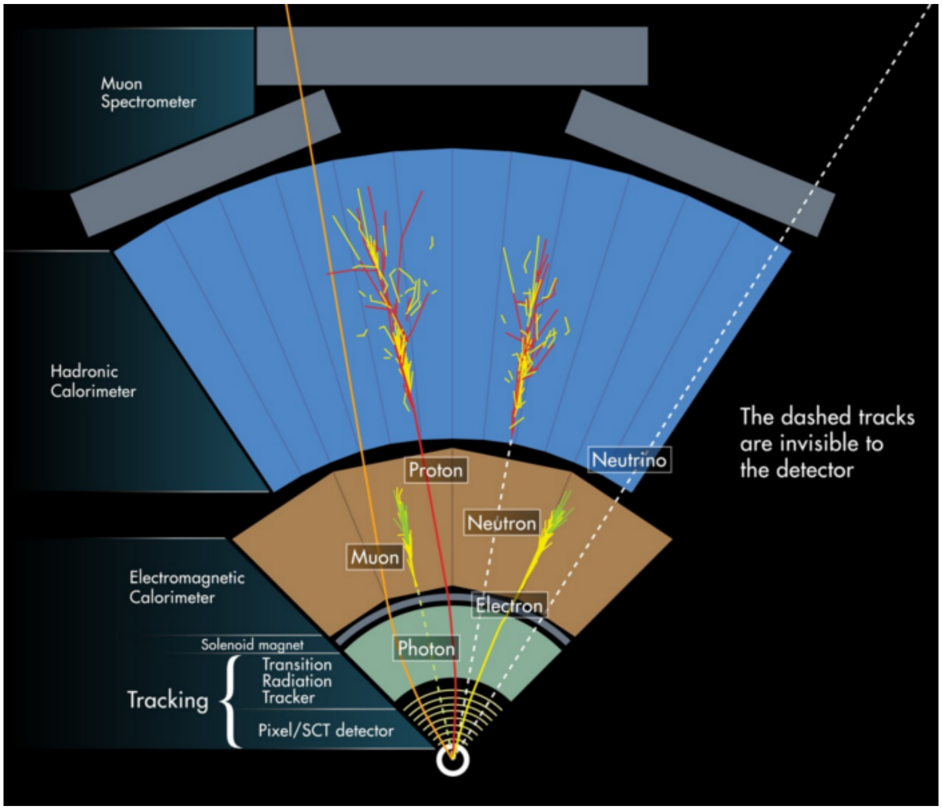

Figure 2.13: Detector signatures of differend SM particles

will apply additional selection criteria to these objects based on these details. These selections along with criteria applied to values such as E_T^{miss} are selected to optimize signal efficiency and background rejection. In some cases also selected to ensure sufficient background is kept to allow for consistent predictions can be made. In chapter 5 this thesis will describe some of these selections for both the run 2 fully hadronic analysis as well as for the HL-LHC extrapolation.

2.4 Transition Radiation Tracker Studies

This section will give a more detailed description of the TRT, continued from sub-section 2.2.1.3. Some of my favorite work while at Penn was keeping the TRT running as smoothly as possible by conducting investigations into reoccuring errors when they became prominent, testing and repairing many boards over the years while at CERN, and assiting in day to day operations including taking on-call shifts, running calibrations, and replacing boards in the detector as needed. It will start with a more general view of the sub-detector. It will cover the read out chain, the process of going from a particle interaction inside the detector to that siganl being carried out to eventually be stored as data for an event. The timing related to reading out events will be included with the description of the read out electronics. Finally, descriptions or mentions of some of the specific projects I worked on directly related to the TRT will be included.

2.4.1 TRT Overview

The TRT is the outermost of the three sub-systems of the Atlas inner detector and is a straw tracker. It is composed of two primary sections, the barrel which is around the primary interaction point at low z and the endcap which is on either side of the barrel at high z, farthest from the interaction point. These two sections are also split into two sides each, denoted side “A” and side “C”, being divided at $z = 0$. In total between these four regions, over 250,000 straws are included in the TRT with straws arranged axially in the barrel and radially in the endcaps. The straws are placed such that at least 35 hits can be identified on a track for a charged particle that originates at the interaction point. The TRT is used for electron identification, tracking information, and serves as a trigger while ATLAS runs in its cosmic mode for testing purposes with no active beams.

2.4.2 TRT Electronics

The TRT electronics can be thought of as being separated into 2 categories. One I would call the read out chain, which takes the signal from the straws, packages, and delivers it to be stored as data. The other sends signals into the detector to set configurations, send resets and triggers, and overall allow for the read out chain to be controlled.

The control portion of the electonics begins with the Timing and Trigger Controller (TTC). This is an off-detector VME module that is responsible for “steering” the front end electronics (portion that are on-detector). The TRT operations teams and ATLAS shifters can communicate with the TTC in order to send signals to the front end. These signals go through TTC lines to the TTC patch panel, which distributes the signal to the front end electronics ensuring that each line in the front end will receive the same commands and run in sync.

The majority of this discussion will focus on the read out chain which starts with the front end electronics. The straws within the TRT are organized into groups of 8, each of which is tied to an ASDBLR (amplification, shaping, discrimination, and base-line restoration). The ASDBLR is the first chip in the read out chain and the only analog one. It can boost and shape the signal received directly from the straw, as the name suggests, and detect signals at two different thresholds. The signal from the straw is first amplified, then shaped in order to identify the electron avalanche from the ion tail. The long ion tail is then removed and the signal is passed to the baseline restorer to recover the shape without the tail. This modified signal is passed to a pair of discriminators that check the two threshold values. The first discriminator checks for a low threshold to signal a hit on the straw and the second applies a high threshold to identify transition radiation. Nominally these values were 200 eV and 5 keV, but the values are set per channel and fine tuned using calibration scans throughout the detector in order ensure proper read out. These thresholds have also slowly increased as the TRT has aged and been exposed to large amounts of radiation. An analog-to-digital conversion is performed within the ASDBLR and the ouput signal is ternary: "0" for no threshold, "1" for low threshold, and "2" for high threshold.

This signal is sent directly to the second chip in the read out chain, the digital time measurement read-out chip (DTMROC). Each DTMROC receives signals from two ASDBLRs, therefore 16 straws feed into it. Every time a trigger is recieved from the TTC patch panel, the DTMROC will take the data received from the ASDBLR and package it to be sent to off detector electronics. Each of these packages includes 75 ns of data, meaning it covers three bunch crossings, so the data is bundeled into three 25 ns segments. On the DTMROC chip the 40 MHz clock is multiplied by a factor of eight to achieve a 320 MHz clock. This allows the DTMROC to sample the output of the discriminator on the ASDBLR every 3.125 ns to locate the leading and trailing edges of the signal. This sampling rate gives a root mean square "effective time resolution" of 1 ns. The DTMROC will in total send a 444 bit package to the ROD patch panel through a single twisted pair cable for the full 75 ns period. More detail in the structure of these packages can be found in Section 3.2.

The ROD patch panel receives the data from the DTMROC through twisted pair cables where a Gigabit Optical Link (GOL) will then organize, package, and send it through a fiber optic link to the read out driver (ROD). It is important to note that within this thesis a ROD will refer to a logical ROD. A physical ROD, meaning one complete board, has two logical RODs on it. Some resources are shared by both logical RODs, but the data read out is treated separately for the two. The ROD will then repackage the data from the DTMROCs (120 in the endcaps and 104 in the barrel) into a single output buffer. It is during this packaging that the data is compressed, this process is discussed in depth in Chapter 3. The ROD then passes this output buffer through the S-Link to the ATLAS read out system. There are in total 64 RODs in the barrel, so with 104 DTMROCs per ROD meaning 1,632 straws, a total of 104,448 barrel straws are read out. In the endcaps there are a total of 128 RODs with 120 DTMROCs, so 1,920 straws, per ROD giving a total of 245,760 straws being read out.

2.4.2.1 TRT Synchronization

This section details some of the major timing issues that have been prevalent in the TRT for years now. They first became prominent during late Run 2 and have continued into Run 3 including having several investigations into their causes in an attempt to better understand and address the errors. This section is more intended for those more studied on the TRT, especially TRT DAQ experts, but I will give an overview of some of the relevant parameters and key details.

The LHC supplies a 40 MHz beam clock that is propagated to all subdetectors via the ATLAS TTC. This clock is received by the TRT at the TRT TTC which then sends the signal down the line to all of the TRT electronics boards. The TRT TTC sends this clock to the TTC patch panel which will then send the clock to the front end boards which have the ASDBLR and DTMROC. Every set of chips on the front end boards need to have an ability to delay the clock signal in order to synchronize with each other as well as the upstream boards. This delay is handled on the TTC patch panel, individually for each channel, in order to set the delay for each front end chip. This is very important as there is a small delay presented every time a signal must be sent through any cable, and slightly different cable lengths will mean a need to individually delay the clock in order to offset this difference. The TRT TTC also sends the clock to the ROD which forwards the signal to the ROD patch panel. The ROD patch panel can also control the delay on the clock in order to properly set the phase of the GOL with respect to the incoming data. Delays for the clock signal, for both triggers to take data on the front end and read out data on the ROD patch panel, are handled and can be adjusted by the Delay25 chips. These can delay the signal from 0 to 24.5 ns in increments of 0.5 ns. A set of two delay scans are run within the TRT in order to determine and set proper delay parameters to the various chips. The first is used to ensure the clock signal is latched by the DTMROC, each delay is then set. The second finer scan is run to ensure that all of the chips read by a single GOL (up to 30 DMTROCs) read back correct data that is in sync. Notably there are regions of instability in both scans, generally on the rising edge of the clock.

It is important to note for part of the description of one investigation detailed later, that the clock is sent to the ROD and then from the ROD to the ROD patch panel.

During running of the ATLAS detector, unstable beams will regularly cause issues with timing both in the TRT and other subsystems. But even after these timings have been determined and during stable beam data taking, there are a few known scenarios that can cause errors in the timing. Typically these occur when the Quartz Phase Locked Loop (QPLL) chip and its associated crystal have problems and are unable to sufficiently stablize the clock signal. This can happen because either the chip itself or the associated Quartz crystal on the board have an error themselves or when the LHC clock has too much jitter, which is known to occur at times. These chips are on the ROD itself (which has 1 chip-crystal pair) as well as the ROD patch panel (which has 4 chip-crystal pairs). As mentioned before, the ROD receives the clock first, it will be stablized by the QPLL, then sent to the ROD patch panel where it is split into 4 clock signals, each of which is stablized again by its own QPLL. Notably, there is one QPLL-crystal pair associated with each GOL on each board.

There are two types of timing or synchronization errors in the TRT. The first is called a “lock resync error” and the second id a “buffer resync error”. In either case, when they occur the full TRT must resynchronize which takes roughly 30 seconds meaning the TRT will assert busy and prevent the entire ATLAS detector from taking data, this delay is referred to as dead time. In many cases 30 seconds doesn't sound that long, but when you consider the bunch crossing rate in the detector gives 40 million potential collision times per second, this 30 second dead time represents the loss of a lot of potential data. It is important to note that this loss of potential data taking accounts for only several percent of the total possible; however, this is considered unacceptable for a single subsystem on ATLAS to cause so much loss. With many subsystems within ATLAS, if each caused even a few percent of lost data taking time, it would quickly add up to a very large loss of data overall. The buffer errors are most often caused by large jitter from the LHC clock and tends to affect subsystems across the detector in random patterns, so are less important to correct from the perspective of finding a fix within the TRT specifically. The lock errors however tend to indicate a problem in the QPLL so are a TRT specific problem. They are generally expected to be mostly random and distrubted independently throughout the TRT. The following subsection will focus on the lock error investigations during Run 2, further discussion of the buffer errors is beyond the scope of this document.

2.4.2.2 Run 2 Lock Error investigation

For most of Run 2 there was a fairly low rate of these random lock errors, but late in 2017 and during early 2018 data taking there was a marked increase in the rate at which we saw them. During these errors there was no indication of instability in the LHC clock or of any hardware problems that would affect or degrade the signal as it was propagated to or within the TRT. In order to further investigate a simple database was developed to combine error logs from the TRT as well as the beam information from the central ATLAS database. With this a basic framework was devised to study the specific error types from the TRT and associate them with beam conditions to look for any patterns.

The first noticable finding was that these errors were not independently distributed within the TRT, there was a distinct pattern within the lock errors. It was seen that approximately 8% of the 192 RODs had more than 10 lock errors each making up the majority of lock errors. The pattern within each ROD was also consistent. To ensure clarity, this does not mean the 8% RODs all have the same error as each other, but rather that each individual ROD tends to have the same error each time a lock error presents. When a lock error is given it indicates which of the four GOLs on the associated ROD patch panel is giving the lock error. This can be one of the four GOLs or multiple, including all four GOLs at once.

This initially lead to the expectation that the problem was originating on the ROD patch panels given the granularity. The ROD only has one GOL (and therefore one QPLL-crystal pair) so any timing error on the ROD would be expected to affect all four lines. Having errors present as only a subset of the four GOLs on the patch panels implies that something on the patch panel was the problem. Attempts were made in test stands outside of the ATLAS detector to replicate these errors to better study the details. This turned out to be very difficult however as the errors were fairly rare, occurring approximately once in every one trillion clock ticks. This lands in a difficult region where it is rare enough to be very hard to reproduce outside of the main detector, while simultaneously being common enough to cause significant dead time in the detector given the massive number of clock ticks while running.

To test this hypothesis a series of tests were devised to be carried out simultaneously. First, the ROD with the largest number of lock errors (about 350 errors) recorded was swapped with the neighboring ROD which had no errors. Then the second most offending ROD (which had about 175 erros) had its patch panel replaced with a spare from outside of the detector that was known to be good. Three more RODs with nearly the same number of errors (approximately 150 each) were in one case swapped with a spare ROD, next was unplugged and reseated in the VME crate, and finally had its GOL cables swapped. These last two tests were done to ensure it was not a connectivity issue that would also have been fixed by swapping a board as in the other tests.

The results from this test were in many ways mixed. The first ROD swap caused a decrease in the error rate, but did not fully fix it. The second ROD swap fully eliminated the errors. The patch panel swap also fully eliminated the errors. And the two tests involving swapping cables and reseating the board saw no change to the error rate. This showed that a problem that was affecting only one GOL on a patch panel could be fixed by either swapping the patch panel itself or the associated ROD which has one QPLL which is connected to all four on the patch panel. At the same time switching the ROD can alleviate without fully solving the problem. The final two cases did show that it did not seem to be an issue with a cable or board connection and it is a problem on the boards themselves.

This series of tests lead to a few primary conclusions. The timing problem at its core seems to be on the ROD patch panel, as the granularity shows it can be on a subset of the patch panel GOLs, and is relatively infrequent. This explains why changing the patch panel can fix the problem. However, since the problem is related to a timing issue, if the incoming clock can be made more stable by cleaning up any clock jitter before reaching the patch panel, then the problem can also be either reduced or eliminated. This explains how swapping or replacing the ROD associated with the patch panel can reduce the error rate. The core problem seems to be that the QPLL chip and crystal pair are just on the edge of stability. This is why the errors are occuring only once every 10^{12} clock ticks. It is also apparent that for some reason the problem is exacerbated by higher occupancy during the high pileup environments of late 2017 and early 2018. This could help explain some of the difficulty in recreating the error outside of ATLAS. Overall it appeared that specific pairs of RODs and ROD patch panels combine to cause the problem. This means the stability can be restored and the errors can be either fixed or reduced by replacing the patch panel, therefore removing the offending QPLL, or replacing the ROD so that the replacement hopefully sends a more stable clock to the patch panel.

At this stage mitigation efforts were employed to minimize the dead time while running during further investigations. Problematic ROD and ROD patch panel pairs were kept track of and when these errors would present either the ROD or the patch panel would be replaced. Due to a limited number of spare boards, removed RODs and patch panels were used as replacements so long as they were not going to be paired with the same one they had been paried with when they were originally removed.

A board was also designed at the University of Pennsylvania with the instrumentation engineering group in order to measure the clock jitter on the signal coming out of the various RODs. The plan was to measure the jitter on the set of boards that were causing resyncs as well as those that reduced or stopped the resyncs on a particular patch panel. If there is a substantial difference in the size or amount of jitter between these RODs that could confirm the going hypothesis. This would suggest the issue is in fact on the patch panel, but the incoming signal quality impacts the ability of the QPLL to properly stablize it. If this is in fact the scenario, a campaign to measure all ROD output jitter could help to prevent bad pairs of RODs and patch panels going forward. When the initial testing was conducted however, there was no noticable variation in the amount of jitter from the various RODs. It appeared that although certain ROD and patch panel pairs were problematic, it couldn't be explained simply by the jitter coming from the particular RODs.

Finally, plans were made to further investigate the error itself. By triggering on the lost lock signal of the QPLL and looking at different signals on the ROD and patch panel, a better understanding of the exact conditions and cause of the lock error might be identified. This is much easier to do in a test setup outside of the detector with more access to the boards themselves. One hypothesis following the jitter measurements was that the lock errors may not be from clock jitter, but from a slightly shifted clock phase or phase jump, where the delay between the falling edge of the clock and the next rising edge is longer than the nominal 40 MHz clock would typically give that causes the loss of synchronization. The details of this investigation are presented in subsection 2.4.2.3

2.4.2.3 Phase Shift Board Investigation

To proceed with this phase shift testing, a second board was designed by the University of Pennsylvania instrumentation group that can take the output clock from the ROD, shift the phase of the clock by passing it through an additional length of cable, and then pass it to the patch panel in hopes of finding a consistent way to recreate the lock errors without the full ATLAS partition. This "phase shift" board was brought to CERN while preparing for Run 3 where I led the investigation into how robust the QPLLs were in dealing with changes to the phase and frequency of the received clock signal and ideally allow the lock errors to be recreated in either the building 104 or SR1 test stands. Some of the major details and results are presented in this subsection.

After the end of Run 2, the phase shift board was built at University of Pennsylvania in order to proceed with the proposed testing during LS2. This testing was delayed due to COVID travel restrictions during 2020 and into early 2021. Once travel was more accessible during the summer of 2021 the planned testing was started. The primary goals were to first measure how robust the QPLL and crystal pairs were with respect to clock jitter. This was planned with two separate tests to be conducted in the TRT test stand in building 104. The first was to provide a shift to the phase of the clock received by the ROD patch panel to test how much of a phase jump the QPLL could still stablize and at what point the QPLL would lose its lock. Next, a signal generator would be used to supply a clock that differed very slightly from the nominal rate of the LHC clock and the range would be measured in which the QPLL maintained lock. This testing would be done on a set of ROD patch panels which included a known problematic GOL as well as patch panels with no history of lock errors while in the main ATLAS detector.

The setup for this testing placed the phase shift board between the ROD and the ROD patch panel. While this clock was being supplied to the board an oscilloscope would be used to spy on the QPLL output that signals when it loses lock, meaning synchronization was lost. The phase shift board has two paths that could be switched between, one that had no delay passing straight through the circuit on the board and the second that was delayed by passing through one of several LEMO cables of set lengths before passing through the remainder of the board, using the same circuits as the first path. The board could switch between the two outputs either using a push button or with an input signal from a signal generator sending a binary signal, where low would activate the delay and high would have no additional delay. This would allow the ouput clock from the board to the ROD patch panel to "jump" when the delay is activated. The delay could be set in 1 ns increments (the granularity chosen for initial testing) by changing which length cable was being used.

Results from this testing, though interesting, once again did not give a clear answer to what caused the lock errors in the TRT. One known bad patch panel, one patch panel known to be generally good but susceptible to these lock errors on a specific channel, and several working pathc panels were tested and compared. For each patch panel and GOL channel the test was run and categorized as "passing" meaning lock was never lost, "unstable" to indicate that lock was lost with only one direction of the phase shift, and finally "failing" where it would lose lock in either direction. The known bad patch panel would become unstable with a shift as low as 2 ns on some channels and with a 3 ns shift on every channel. The board with regular lock errors from one of the four GOLs would consistently pass on every channel with a 3 ns phase shift, become unstable on every channel with a 4-5 ns phase shift, and fail on every channel with a 6+ ns shift. This immediately showed that the specific GOL that would present lock errors was no less capable of handling phase shifts than the three other channels on this patch panel. When the known good patch panels were tested, most showed identical results. Every single known good patch panel would pass with a phase shift up to 3 ns, the majority became unstable with a 4 ns delay, and all but one failed with a 6 ns delay. The one board that did not was for some reason more stable than most being able to consistently pass witha 5ns delay, become unstable with a delay of 6ns, and only fail once a delay of 7 ns was applied. Either way, we saw that the board known to be prone to lock errors performed at the same level as many with no history of them.

A second test related to the phase shift was added at this time to consider that it may not be a single phase shift, but repeated phase shifts that occurred frequently enough to cause loss of synchronization. The signal generator used to trigger the jump would ouput a square wave and the frequency could be changed to set how often the clock would jump forward or backward in phase. Originally this was only used to switch the phase often enough to reasonably test when the synchronization was lost. Increasing the frequency of this square wave allowed us to test if it isn't a single phase jump, but more regular jumps in the phase coming from the ROD, that would cause the loss of synchronization. Because most boards fully passed the testing by retaining lock with a jump of 3 ns, but became unstable with a 4 ns jump, each board was tested with the 3 ns jump and slowly increasing how frequently that jump would occur until the QPLL would lose lock. Not every board was tested for this, but the patch panel known to have lock errors along with two others that did not. Once again there was no difference between the three boards, the patch panel with a lock error history performed identically. All three boards continued to be in the passing state with a 3 ns jump until the frequency of the phase shifting reached 1 kHz at which point they became unstable.

It is important to note that at each stage of this tesing the test set up in the test stand was run with the altered clock input to see if the "loss of lock" that was being observed from the QPLL chip ever resulted in "lock resync error" that had come up in combined runs of the ATLAS detector. In every case when a sufficient phase shift was supplied to cause a loss of lock in the QPLL, the testing output would give a number of errors, but they never presented as the specific lock error that we had been trying to isolate.

2.4.2.4 Frequency Modulation Investigation

The final set of tests run thus far in an attempt to isolate the lock error was the frequency modulation tests as were briefly mentioned in subsection 2.4.2.3. This testing still utilized the phase shift board, but with an altered set up. In this instance the goal was not to supply an identical clock signal with a jump in the phase of that clock, but instead to supply a clock of a slightly different frequency than the nominal LHC clock. Notably the LHC clock is technially slightly above the stated 40 MHz, actually being 40.07897 MHz. In order to do this no phase shift was used, we would not be switching it on and off so there was no benefit to using the shift, but instead the clock from the ROD was not sent to the patch panel. Instead a 40.08 MHz clock signal was produced by a signal generator and injected into the phase shift board to mimic the 40 MHz LHC clock. Normally the clock signal is sent from the ROD through an ethernet cable, which has four pairs of wires, one of which is the clock. In order to keep the ROD patch panel running an ethernet cable had to be opened and only the clock signal from the ROD was disconnected and replaced by the signal from the generator. The other 3 signals are still relevant to the TRT so they still needed to be passed from the ROD to the patch panel. At this stage the intent of the tests was more so to test how robust the QPLLs were generally. There wasn't necessarily a motivation as to why this altered frequency would correlate to the lock errors or what the reason would be that it created the lock errors if the problematic GOL was found to differ substantially in its allowed frequency range.

For each patch panel in the testing group the signal generator supplying the modified clock would be varied slowly until both a lower and upper bound for which the QPLL would maintain lock was found. In this test there once again was no problem found with the known problematic patch panel. In fact, the patch panel in question was actually found to be slightly more robust than many of the others. It had an allowed frequecy range from 40.0747-40.0823 MHz on the channel in question, comfortably containing the nominal 40.7897 MHz. Many of the other patch panels had a similar lower limit but only worked up to about 40.080

MHz.

The final state of this testing campagin gave a substantial amount of information and potentially useful data about the QPLL chips and crystals regarding how robust they are, that could one day be helpful. This testing has been documented and recorded through a number of presentations including sheets of collected data in the event these questions are asked again. However, with respect to the specific questions for running the TRT in Run 3, nothing notable regarding the still mysterious lock errors was identified.

2.4.2.5 Going Forward and Final Thoughts

This final subsection is a bit less technical and instead describes some of the current practices being used with the TRT to mitigate the lock errors. I also discuss some of the "next steps" that have not been followed up on at this time, but if there is a growing need could be looked into. Finally I will mention a few of the other projects that I have

First to address the status of the lock error mitigation, the preventative measures that were adopted near the end of Run 2 are being continued in Run 3 and so far have been generally effective. When a ROD and patch panel pair present with a large number of lock errors, an intervention is scheduled to replace one or the other with a board that does not have a history of having lock errors in the new pairing. A set of all patch panel and ROD replacements is kept by TRT DAQ, including the reason for the replacement, in order track which pairs have a history of creating lock errors in order to keep them apart. It still seems to be that particular pairs of RODs and patch panels tend to have more of these errors, and by avoiding those pairs the dead time has been kept to a minimum. During early Run 3 there have been multiple other problems that came up and caused more dead time by the TRT that have required the focus of the TRT DAQ team. In every one of these cases, the combination of the TRT experts working on various parts of the TRT, both at CERN and abroad, have been able to find solutions and get the TRT back to running with minimal dead time.

As to the status of the lock error investigation, there has still been no success in recreating these lock errors outside of the ATLAS detector. In fact, they haven't even been seen when running the TRT in its standalone partition inside of the main cavern, they have only been found while the combined ATLAS partition is running. This presesnts a major challenge in that to try to continue trying to identify the cause we need the full detector running every subsystem has its own projects and investigations they're working on. In hopes of being able to look into this further, the patch panel that was being used as the problematic example had a "spy cable" soldered onto the QPLL signal which identifies a loss of lock. The initial goal for this was to install it in the main cavern, along with an oscilloscope monitoring that signal which can be controlled and monitored from an off-detector cavern to try to better study what can cause this problem. One problem with this was a question of whether or not the oscilloscope could function properly with the amount of radiation in the main cavern when there are active beams, and on top of that, if there is a chance that the $30,000 rental oscilloscope could be seriously damaged by the beam radiation, which is a major risk to take.

A second plan was developed that would be safer, albeit less effective, than having the oscilloscope in the main cavern. There are a number of extra ethernet cables that were installed in the cavern early on and run up to the off-detector cavern, which are available in case there is a need for them. An ethernet cable with a female connector was cut open and soldered to the spy cable in order to send this signal to the upper cavern. In this location the oscilloscopec can be safely used without being exposed to significant radiation. But sending this signal up through a very long ethernet cable does result in a signficant loss to how clean the signal is. One additional problem that limits how much of an ability we have to run this investigation, is that in order to actually use this setup a known bad pairing of ROD and patch panel has to be used with the goal of triggering the error and therefore causing dead time for the detector as a whole. This means it isn't the most desireable choice anytime data taking is actually being conducted. Unless the lock errors become more significant and the need to further investigate this problem is increased, this testing is on hold.

This resync testing and various related investigations have been some of my major projects on the TRT, along with the compression studies I conducted as part of my qualification task, which is presented in Chapter 3. I wanted to take a moment at the end of this section to give a short mention to some of the other tasks and work I have been involved with on the TRT. As with all TRT DAQ experts I have taken part in day to day operations of the TRT to keep it running and ensure it's in the correct mode for each run of the ATLAS detector. We have all taken a share of on-call shifts where for a week at a time we are reachable day and night in case there is a problem with the TRT and the current shifter needs to reach us. We have all been a part of regular interventions to replace boards that start having regular errors with one of the spares we have. One of the places where my time on the TRT differs from many is a task I was trained for, starting my first summer at CERN, by an older student that had this task before me. This was to handle, test, and repair these boards after they are removed from the detector. The first round of testing after a board is removed typically happens in our test stand in building 104. I have spent many years keeping this test stand running properly, making small repairs at times to maximize its functionality, and having to make major adjustments in some instances when everything seems to stop working. I have also become one of the final experts on tesing the patch panels that are removed from the detector, identifying which ones seem to work fine and which need to be repaired, trying to tell which that need repairs seem to be the simplest and most likely to be fixed, and finally going about making those repairs. The TRT test stand in building 104 is one that has essentially served as my office many times, is a room that I have become intimately familiar with, and will always associate with my time at CERN working on the TRT, and not just because it's one of the only air conditioned rooms I'm able to use in Switzerland.

CHAPTER 3

TRANSITION RADIATION TRACKER COMPRESSION STUDIES

3.1 Introduction

During Run 2, a number of upgrades were made to the TRT hardware and software to ensure stable running and no data loss. The target L1A (Level 1 trigger) rate was 100 kHz and with an average pileup of $\mu = 60$. A general background of the TRT readout is provided in the granularity note (See ref. [3]). A more detailed and technical outline of the upgrades is found in the Run 2 TRT DAQ Performance note (See ref. [4]).

Briefly stated, the data from the front end boards is packaged in the RODs (read out drivers) and sent up to the ATLAS readout system (ROS) via the S-Links. The size of the ROD fragment being sent to the ROS and the speed at which the S-Link can transmit limits the L1 trigger rate. If this rate is exceeded then the ROD will assert busy and create deadtime for the entire detector. To improve the allowable L1 rate either the fragment size can be reduced or the S-Link speed can be increased.

At the end of Run 2 the targeted pileup, $\mu = 60$, and L1 rate of 100 kHz were achieved. Improvements to the S-Links and later upgrading the HOLA cards on the S-Links allowed for the S-Link rate to be increased to 60 MHz. Improvements to the data compression also decreased the ROD fragment size. In addition, dropping the least significant bits, suppressing specific error words, and introducing the hardware validity gate (HWVG) to increase the zero word rate further improved the compression. A more detailed set of upgrades and the process from early Run 2 leading to the final Run 2 setup can be seen in the Run 2 Performance note (See ref. [4]) as well as outlined in Ian Dyckes's qualification note (See ref. [5]).

Looking forward to Run 3, the process of investigating the TRT's performance needs to be revisited. The purpose of this section is to cover the documentation and provide detail on the methods that were considered, their performance, and the changes that are likely to be made. In subsection 2 an overview of the data structure of the TRT straw words is given. Also a brief description of the compression method is given comparing the lossless Huffman encoding and lossy compression schemes including a specific one, Scheme0p. Then an overview of the final Run 2 setup is given as a starting point for any possible changes which are outlined in subsection 4. Subsection 5 contains the detailed studies comparing these projected changes as well as investigating the ability to implement them and leading to a projected set up for early Run 3 detailed following that. Finally, a description of some of the documentation changes relevant to properly running the compression software is given. Updates to some of the general TRT documentation in TRT-DAQ-DOCS as well as a page to better navigate the documentation for newer users is outlined.

3.2 Compressing Data

A very thorough description of this section with more detailed information is seen in (See ref. [4]) and (See ref. [5]) including specifics regarding the timing and a more precise counting of the relevant bits of each of these processes. More briefly than in those documents, an ASDBLR reads out 8 straws and sends its output to the DTMROC. Each DTMROC reads out 2 ASDBLRs and therefore has the information from 16 straws. When a L1 accept is sent from the front end electronics the ROD then receives the data from the DTMROC representing hits in the straw as well as high threshold hits representing transition radiation.

Each straw word includes data from 3 bunch crossings and is shown in Figure 3.1. A bunch crossing occurs every 25 ns and the straw word includes 9 bits for each one. The first bit is a high level bit representing if the straw crossed the threshold for transition radiation at any time in the 25 ns. Also every 3.125 ns (8 times per 25 ns period) a low level bit is created representing if the straw was over the tracking threshold. This makes 9 bits per straw per 25 ns bunch crossing period. Three bunch crossings per straw word gives a 27 bit straw word.

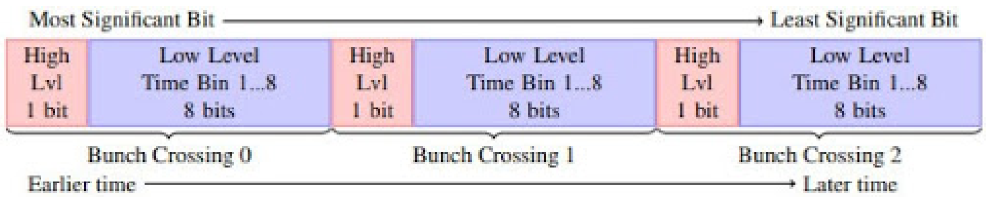

Figure 3.1: Structure of the 27-bit straw word. For Run 2 the last 4 bits were dropped giving a 23-bit word.

The ROD collects this data for 3 bunch crossing from 120 and 104 DTMROCs from the endcap and barrel respectively to form 1 ROD fragment. The last 4 low threshold bits were particularly susceptible to out of time pileup and were not very useful so were dropped to reduce fragment size. This change had been planned from early on because reading the data from the front end into the RODs would limit the rate to 90 kHz. Dropping the last 4 low threshold bits was necessary to go above this trigger rate. Figure 3.1 shows the structure of 1 straw word coming from each DTMROC and Figure 3.2 shows a ROD fragment containing the necessary information for offline event building. In order to send these 27 bit readouts as 32 bit words, the 5 upper bits in the 32 bit word are set to either '0's or '1's depending on the current ROD firmware. The ROD fragment consists of a header, 16 straw words, variable width error block, and trailer.

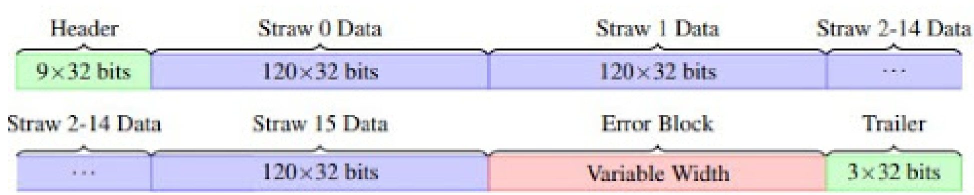

Figure 3.2: Data structure of a ROD fragment.

3.2.1 Lossless Compression

The TRT uses Huffman encoding, a form of lossless compression. A more detailed description of Huffman encoding is again given in (See ref. [3]) including a visual example. Briefly, Huffman encoding assigns a short code word to each common straw pattern. The most common patterns have the shortest code words and very uncommon patterns are not given a code word at all if it is more efficient to output the full straw word rather than increase the average size of code words. These code words are stored in a compression table which is loaded onto the RODs to compress the data and used again to decompress the fragments to reconstruct the event offline. The zero word is by far the most common and in our case it has a single bit code word, 0b1, so all other code words must begin with 0b0 as Huffman encoding is prefix free, meaning that no code word can contain another code word.

Huffman encoding is a 1-to-1 process so it is fully invertible. All information can be regained during the decompression. It is called a form of lossless compression because no information is lost in the process. Some of the earlier processes that reduced the code word size (dropping low threshold bits, hardware validity gate, high threshold bit masking) are not invertible but these occur prior to the Huffman encoding in order to reduce the number of common straw words.

The downside of lossless compression is that it is subject to information entropy. This is the minimum number of bits that can successfully store all information in the data. This will be dependent on the number of patterns being encoded as with more patterns the longer the code words are on average. Huffman encoding is subject to this as all lossless schemes are. In order to further reduce the size of the compressed data some information must be lost, this is called Lossy compression.

3.2.2 Lossy Compression

Lossy compression does not create an invertible 1-to-1 mapping, but rather a N-to-1 mapping where multiple straw words will be reduced to a single code word. This is a non-invertible process as the code word cannot be successfully converted back into each original straw word. The data cannot be fully regained after lossy compression.

In this scheme, more straw words will have corresponding code words in the compression table. This results in fewer instances that require sending full straw words through the S-Link. The code words will be shorter on average as well. These two effects will give a shorter average non-zero word length and therefore a higher compressibility. The compressibility will be measured by the non-zero word length.

This higher compressibility comes at the cost of information loss. Ideally the scheme is designed such that only unused information is lost and as much unused or irrelevant information as possible is lost. A more aggressive lossy compression with more information lost will give a shorter average word length and therefore a higher compressibility.

For any lossy compression scheme, such as scheme0p, analysis of the encoded data would have to be done using the N-to-1 mapped data words and the information lost is unrecoverable. The TRT N-to-1 mapping would be done in the ROD firmware prior to the encoding using the compression table. The reduced data from the N-to-1 mapping would then be encoded using the compression table (built from a dataset that has undergone the N-to-1 mapping) and sent through the S-Link to the ROS just as with the lossless compression scheme.

Scheme0p is the specific lossy scheme that was investigated during Run 2 but never implemented due to firmware timing errors. Detailed information on the Scheme0p compression algorithm can be found in ref. [5].

3.2.3 Run 2 Final Setup

During Run 2, the hardware upgrade of the HOLA cards was a sufficient addition to the use of lossless Huffman encoding to run at $\mu = 60$ and 100 kHz without saturating the S-Link. Scheme0p was never implemented due to the mentioned difficulties with firmware violations. So the final compression scheme of Run 2 only employed this lossless compression scheme.

To optimize running at higher pileup, a table was created using a high μ dataset. Even though the firmware was upgraded to allow the zero word to be changed from 0b1 thanks to Vincent Wong, the byte stream converter was not. This meant there was a limit on how high of a pileup dataset could be used.

Huffman encoding is a prefix free code. This means that when data is being decoded there is no need for a special marker between code words. In order for this to work, no code word can begin with an identical string to another complete word. Otherwise while decoding the data, the first complete word would be detected and any code word that contained another complete word as a prefix would never be decoded. This means no straw word can be encoded as a code word that is a prefix of another. Defining a relatively short code word will prevent that sequence from being used again and terminate any further branches in a binary tree from that point. At $\mu = 55$ the zero word is dominant enough that it is still most efficient to encode it as a single bit, 0b1, despite cutting off the encoding tree at that junction. However, above $\mu = 55$ this is no longer the case. The zero word is no longer dominant enough to require all other words to begin with 0b0.

For most of Run 2 Table 139 was used and had been generated from a $\mu = 37$ dataset. Table 140 was made to replace Table 139 and improve the compression. Due to the zero word constraint Table 140 was created using $\mu = 55$ data. In this case the zero word was encoded as 0b1 and is compatible with the byte stream converter. This table was validated by first taking a noise run in standalone mode followed by an additional noise run in combined mode. The straw hit maps were compared between Table 140 and Table 139. As seen in Fig.3.3, the known dead boards matched and there was no sign of corruption in the new table. The full process for validating a new table is shown in Ian Dyckes's qualification note (See ref. [5]) and will be referenced when validating a new table early in Run 3.

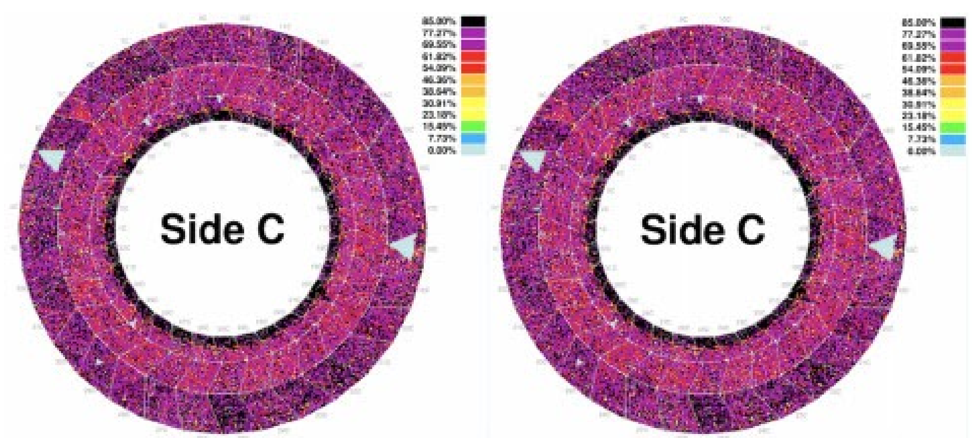

Figure 3.3: Straw hitmaps generated by TRTViewer for high occupancy noise runs using compression Table 139 (left) and Table 140 (right). Known dead boards match between the two and there is no visible corruption from the new table.

3.2.4 Possible Changes

This section details planning and analysis that was done during late Run 2 and LS2. For continuity it discusses Run 3 as a future event, even though Run 3 is ongoing now.

Going forward into Run 3 some beam conditions will likely be changing while some, including the intended peak pileup within the detector, are intended to stay the same. Not all of the information about Run 3 beam conditions are fully known, so as further plans are decided, more accurate predictions of the TRT's occupancy can be made. For now several possible changes were suggested and tested on late run 2 datasets to compare their performance and test what changes will be necessary to run smoothly after start up.

The beam structure in Run 3 is still unknown as of the time this was written and several options are being considered. The exact beam structure and shape will likely not affect the ability of the TRT to properly take data at any given rate. It will however likely require a new compression table to be made early on in Run 3 that can account for these changes and how they affect the most common straw words.

The projected pileup of $\mu = 60$ is the same as in late Run 2. This is the main factor to consider to best predict necessary changes and the eventual performance of the TRT. Because this is not intended to change, it is likely that necessary changes to the current compression will be minimal to optimize data taking and perform smoothly in Run 3. The L1 rate is also planned to stay the same which will also support this.

The suggested changes to consider for the compression include: training a table at $\mu =$ 60 (requires updating the byte stream converter), implementing N-to-1 mapping in the form of Scheme0p (this was the proposed and tested form of lossy compression that was not implemented in late Run 2), using compression tables built for region specific data, and compression tables built and applied based on the different gas content in different straws and regions of the detector. Each of these changes has a different set of potential benefits and difficulties that will be explored.

As noted before, the final setup for Run 2 used a table trained with a $\mu = 55$ dataset. This was done because the byte stream converter currently hardcodes the zero word as 0b1. As Huffman encoding is prefix free this works only when the zero word is by far the most common straw word. When $\mu >$ 55, it is no longer dominant enough to make this efficient. This means to train a table at $\mu = 60$ the byte stream converter will need to be modified. According to researchers involved in creating the table (primarily Paul Keener), it should be easily changed but will require their help closer to the start of Run 3. The firmware is fully prepared to handle these changes thanks to Vincent Wong.

In theory, implementing Scheme0p would greatly improve the occupancy that the TRT can properly run at for any given maximum L1A rate based on studies originally done by Ian. The efficacy of Scheme0p was also demonstrated by Ian in (See ref. [5]). There are much more substantial difficulties with the implementation in the TRT ROD firmware that lead to the system not being used during Run 2. When trying to implement Scheme0p there were prominent timing errors with the ROD firmware. According to Vincent Wong, to fix these timing errors the firmware would likely need to be fully redone. This is seemingly impossible option unless absolutely necessary.

Region specific compression (primarily considering a different barrel and endcap compression) would be easily implemented in the TRT if it is beneficial. Each ROD can be set to load a different compression table. This does require that any defined "region" includes all straws on the relevant ROD. This means that if there is a reason to, each barrel or endcap section can use a different table as each region is made up of straws on distinct sets of RODs. The tables can be trained on data from any individual region as well. This option is simple to implement if there is a real benefit, but it will slightly complicate the process of defining and updating the compression tables being used if there is a reason to change them.

The gas content geometry varies greatly from the ROD geometry. Individual portions of the barrel and endcap have different gas configurations shown in Fig.3.4. This is however not how individual RODs are distributed. As each ROD has to use its assigned compression table for every straw it reads out, the different gas regions cannot be given unique compressions due to overlap of different gas content on each ROD. Without modifying the gas geometry to match the ROD geometry, this is unlikely to be a possible change.

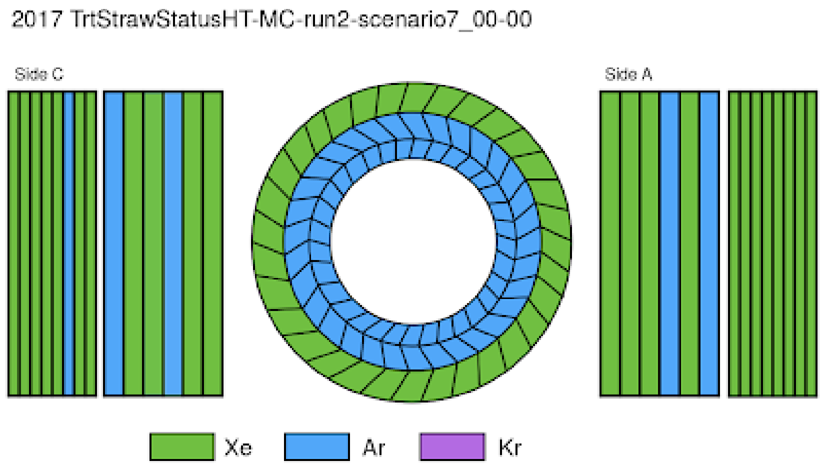

Figure 3.4: The gas configuration of the TRT showing which portions have straws filled with Argon versus Xenon.

3.3 Compression Studies

To begin the study there needs to be a metric to measure and compare the compressibility under different conditions. As stated in section 2, the best metric to measure the compressibility is the average non-zero word length. It is however difficult to quickly relate this metric to the conditions of the detector in each run such as L1 rate, occupancy, luminosity, pileup, etc. These conditions are recorded for each run so it is possible to use the average word length to study how one of these variables is affected for each compression method.

Referencing the equations shown in Figure 3.5, the average word length can be related to the allowed occupancy. By using the recorded conditions (max L1 rate, S-Link rate, etc.) one can derive the relation between the occupancy and the average word length. This makes it possible to use the differences in average word length to measure the allowed increase or decrease in occupancy as shown in Fig.3.6.

Compressed

$$\text{fragment size} = N_{straws} \times [occ \times l_{ave} + (1 - occ) \times 2]/32 + \text{error block} + \text{fixed overhead} \tag{3.1}$$

$$= N_{straws} \times [occ \times (l_{ave} - 2) + 2]/32 + \text{error block} + \text{fixed overhead}$$

Figure 3.5: The equations that describe the fragment size and max L1 rate when the zero word is defined as a 2-bit code word that allows a relation between the TRT occupancy and the L1 rate.

$$\begin{aligned} &occ_1 \times (l_{ave,1} - 2) = occ_2 \times (l_{ave,2} - 2) \\ &\frac{occ_2}{occ_1} = \frac{l_{ave,1} - 2}{l_{ave,2} - 2} \end{aligned} \tag{3.2}$$

$$\begin{aligned} textrmAllowedoccupancypercentincrease &= \frac{occ_2 - occ_1}{occ_1} \\ &= \frac{occ_2}{occ_1} - 1 \\ &= \frac{l_{ave,1} - 2}{l_{ave,2} - 2} - 1 \end{aligned} \tag{3.3}$$

Figure 3.6: Starting from equation 1 in Fig.3.5 and assuming the same L1 rate is constant when using each compression table, gives a condition on how the average word length affects the allowed occupancy of the detector at which it can run without delays.

From this point on, the efficiency of different compression tables will be measured by the allowed increase in occupancy. This means how much the occupancy can increase for a given max L1 rate (planned is 100 kHz) without causing problems in the TRT.

The first change tested was building a new table at the same pileup as Table 140 but in the late Run 2 beam structure. The beam structure changed slightly from the dataset used to train Table 140 and that was used in late Run 2. This gives an idea of how training a table with early datasets in Run 3 (with the Run 3 beam structure) can improve the TRT's compression. There likely will be a more dramatic difference in beam structure from late Run 2 to the start of Run 3 than from the data used to build Table 140 to late Run 2 data.

Table compared to	Table being compared	$\mu = 55$ dataset	$\mu = 60$ dataset	$\mu = 60$ endcap only dataset	$\mu = 60$ barrel only dataset
$\mu = 55$ table	$\mu = 60$ table	4.4	7.6	baseline	baseline
$\mu = 60$ table	$\mu = 60$ endcap table	-0.28	.0.04	0.05	-0.25
$\mu = 60$ table	$\mu = 60$ barrel table	worse	worse	-2.5	-2.3

Table 3.1: This shows the increase in allowed occupancy. The columns represent the dataset that was being compressed. The rows represent the table that was being used to compress the data. The far left notes what these were being compared to. In the $\mu = 60$ table row the 'baseline' designation indicates that there was no $\mu = 55$ table used to test endcap or barrel only datasets. This means the $\mu = 60$ table has nothing to compare to and instead creates a baseline to compare the region specific tables with.

Using Table 140 to compress the data from late Run 2, gave an average nonzero code word length of 11.1368 bits. For the newly trained table that was built from data with the same beam conditions and bunch structure the average length was 11.055 bits. Based on equation 3.3, that yields a 0.8% increase in allowed occupancy for the new table. This is very minor but supports the plan to train a new table on early Run 3 data. From this point forward the average word length will be omitted and only the change in allowed occupancy will be discussed as it is the more relevant and recognized value.

Future tables were all compared to Table 140 (and to each other in many cases) both in their efficiency in compressing a set of data with $\mu = 60$ and $\mu = 55$. This tests that it is still efficient in compressing once the pileup begins to drop during the run. For brevity not all of the values will be shown but no values that did not fit the trend represented were omitted. To see all of these values as well as most of the average word lengths, view the set of updates on this project found in ref. [6]). All of the stated allowed increases that follow are shown in the charts in Table 3.1.

The change to a table trained with $\mu = 60$ was tested next. This table showed an allowed increase in occupancy of 4.4% when compressing a $\mu = 55$ dataset compared to Table 140. It showed an allowed increase of 7.6% when compressing a $\mu = 60$ dataset compared to Table 140. From this increase it is apparent that updating the byte stream converter to allow for a zero word that is not a single bit and therefore a compression table trained at higher μ data will be very beneficial.

The increase in allowed occupancy when compressing the data at a higher μ is the more relevant number in all of these cases. The TRT will be closest to capacity at points in a run where the pileup is the highest so in this case the 7.6% increase is the most relevant number. The increase at lower μ is primarily to show there are no possible complications or inefficiencies as the run progresses and pileup decreases.

Region specific compression was not tested against Table 140. It was instead tested against the table built from $\mu = 60$ data from the full detector. The efficiency compared to Table 140 is less relevant and can easily be found from the comparison to the $\mu = 60$ trained table which was tested against both the regional compression and Table 140.

First endcap data was used to build a table from a $\mu = 60$ dataset and compared against the full detector dataset. When compressing $\mu = 55$ data of the full detector it gave a -0.28% increase (so decreased the efficiency). When compressing $\mu = 60$ data from the full detector there was almost no change, it yielded a -0.04% increase in allowed occupancy.

The endcap trained table, full detector table, and barrel trained table were compared when compressing compressing $\mu = 60$ datasets of the full detector, barrel only, and endcap only. The table built from barrel only data performed dramatically worse than the other two in all cases, very similar to tables trained at $\mu = 55$. This makes sense as the barrel RODs only receive signals from 104 DTMROCs whereas the endcap RODs receive signals from 120 DTMROCs so there should in general be many more straw words in the endcap data. The best case for compressing data from the endcap alone was using the endcap trained table. This only yielded an increase in the allowed occupancy of 0.05% over the table generated from the full detector however. This was the only time there was any advantage to the endcap trained table. The most effective case for compressing data from the barrel alone was using the full detector trained compression table which gave a 0.25% increase in allowed occupancy over the compression table generated from the endcap only dataset. Using a table generated from a barrel only dataset was less efficient than either.

From these studies, there appears to be no reason to consider a barrel only trained compression table. There is such a small increase in the allowed occupancy from applying a table trained specifically to the endcaps that it seems pointless to go to the trouble of building multiple compression tables and loading different tables to different RODs. The simplicity in only using a full detector trained table far outweighs and minor benefit.

A table was built using Scheme0p on $\mu = 60$ data as well. This table gave a 20% increase in the allowed occupancy compared to a lossless compression table trained on $\mu = 60$ data. This would be a considerable improvement to the compressibility of the ROD fragments. The difficulty with Scheme0p lies in the feasibility of its implementation and if it is necessary.

From discussing the implementation feasibility issue with firmware experts it appears that to make Scheme0p work it would require fully remapping the firmware of the RODs, a massive undertaking. Currently the planned conditions for Run 3 are very similar to those of late Run 2. The beam energy is increasing, beyond that only the bunch structure and possibly beam shape appear to be likely to change. Importantly, the pileup is not projected to increase and this is the most critical characteristic affecting the compressibility of data from the TRT. Table 140, which was trained on $\mu = 55$ data, was successfully used through the end of Run 2, so it seems unnecessary to implement as well. With the max L1 rate and average pileup projected to be the same in Run 3 as they were in late Run 2 it is unlikely that the occupancy would change significantly. And given the 7% increase in allowed occupancy at this trigger rate from a table trained at $\mu = 60$ this should easily cover early runs in Run 3 with a new bunch structure before a new table is made on Run 3 data and should leave a significant amount of space to ensure there are no issues in the TRT's ability to run properly in Run 3 once a new table is trained on Run 3 data.

The gas specific compression based on portions of the TRT that use Xenon versus Argon in the straws was also considered. The gas geometry seen in Fig.3.4 differs significantly from the ROD geometry. This makes categorizing RODs based on the gas content of the straws they read out infeasible. The way the ROD and gas geometries overlaps causes most RODs to read a mixture of Argon filled and Xenon filled straws.

3.4 Run 3 Projected Setup

Currently the full Run 3 run conditions are unknown. The maximum L1 rate is set to be the same as in late Run 2 at 100 kHz and the projected peak pileup is also planned to be the same as in late Run 2 at $\mu = 60$. These are the two most prominent variables in limiting the maximum TRT detector occupancy that can be readout. Based on this there is a good chance that no changes will need to be made other than simply training a new table early in Run 3.

The change in beam energy, bunch structure, and any other changes in the beam in Run 3 could affect the most common straw words, but likely not the occupancy. This means that it will be important to ensure that the compression code is running properly and easily leading up to the start of Run 3 so that a new table can be made early on, validated, and loaded into the RODs. This is likely the only necessary change.

Scheme0p would yield considerable improvements. These improvements in the allowed occupancy are almost certainly unnecessary and it seems infeasible to implement Scheme0p at this time.

A compression table trained at a higher pileup, $\mu = 60$, will yield significant improvements. The only necessary change for this is the modification of the byte stream converter to allow for a zero word that is more than 1 bit. This should be a simple change, that likely requires Paul Keener's assistance, but should be easily implemented with that.

Region specific compression is either detrimental or the benefits are negligible and would only add unnecessary complications to the process of loading compression tables and decompressing data. There appears to be no reason to implement this.

Gas specific compression appears to be infeasible at this time without changing the gas geometry to match the ROD geometry, or change the ROD geometry which is even less likely.

Based on these studies, the projected setup for TRT compression going into Run 3 will be to have a table trained on late Run 2 data at $\mu = 60$ with the byte stream converter updated to allow for the zero word to be greater than 1 bit. Early in Run 3 a new table should be trained on early Run 3 data at $\mu = 60$ to account for any changes in bunch structure. These changes should allow the TRT to operate smoothly in Run 3 if the running conditions are as the current plan suggests.

3.5 Documentation

All of the documentation described below were made in the TRT DAQ documentation wiki (TRT DAQ-DOCs). Changes were made throughout the documentation however the most significant change was the addition of an introduction page (See ref. [7]).

This page is intended to introduce new members of the project to the system. It points to important documentation for background reading to learn about the detector initially. These are also extremely important for reference later on as well. The page also includes descriptions of some of the important categories on the site and some description of where to start and how to navigate the pages.

During the process of testing the compression of the TRT all documentation related to compression was updated as necessary. This included correcting some instructions that were out of date due to other changes in the framework. Also making some instructions more explicit to make the process of going back to running the compression code faster to relearn and making it easier for a new student to take on the project and begin to use the relevant programs.

Several other sets of instructions and how to guides were also updated during this time. These were primarily small corrections in places where the framework had changed and the relevant how-to guides needed to be updated. Also in some instances these instructions were made more explicit where current experts understood the guide but a new member would be unaware of some background information.

CHAPTER 4

FULLY-HADRONIC ELECTROWEAK SUSY

This chapter describes a search conducted following Run 2 of the ATLAS detector for electroweak supersymmetric particles decaying to fully-hadronic final states.

4.1 Target Physics Scenarios

Three primary physics scenarios are studied in this analysis. This includes the baseline MSSM scenario where $\widetilde{\chi}_{\text{heavy}}$ and $\widetilde{\chi}_{\text{light}}$ are modeled as bino, wino, and higgsino electroweakinos. Next the gravitino LSP scenario based on the general gauge mediation (GGM) model. And last a SM extension with a QCD axion is considered resulting in an axino LSP scenario.

These three physics scenarios are described in the following sub-sections where each model is labeled as (A,B) representing ($\widetilde{\chi}_{\text{heavy}}$, $\widetilde{\chi}_{\text{light}}$). It's assumed that all other SUSY particles are decoupled in mass [8, 9]. The production modes, final states, included signal regions (SRs), and branching ratio assumptions for each model are summarized in Table 4.1.

In this analysis only boosted states are considered with a mass splitting of $\Delta m(\tilde{\chi}_{heavy}, \tilde{\chi}_{light})$ >400 GeV. Wino-like states form a doublet and higgsino-like states form a triplet creating a mass degeneracy. The mass splittings of these multiplets are typically on the order 10 GeV or less. Because of the large difference between the mass splittings of $\tilde{\chi}_{heavy}$ and $\tilde{\chi}_{light}$ compared to those of the multiplets, the SUSY states within each multiplet are treated as degenerate. Thus particles generated by decays within the multiplets are ignored.

4.1.1 MSSM scenarios: $(\widetilde{W}, \widetilde{B}), (\widetilde{W}, \widetilde{H}), (\widetilde{H}, \widetilde{B}), (\widetilde{H}, \widetilde{W})$

The first model considered is in the MSSM scenario with the Bino, Wino, and Higgsino. There are four mass hierarchies considered: $(\tilde{W}, \tilde{B})$, $(\tilde{W}, \tilde{H})$, $(\tilde{H}, \tilde{B})$, $(\tilde{H}, \tilde{W})$. The mass spectra, mass eigenstates, and decays are displayed in Figure 4.1. A W-boson is charged and therefore generated when a chargino decays to neutralino or vice-versa. A $Z-$ or Higgs boson are emitted when there is no change in charge so a chargino to a chargino or a neutralino to a neutralino.

The assigned branching ratios of $\widetilde{\chi}_{\text{heavy}}$ must be considered. For the $(\widetilde{W}, \widetilde{B})$ and $(\widetilde{H}, \widetilde{B})$ models there can either be a produced chargino or neutralino (two possible neutralinos of slightly different masses in case of the higgsino) but they must all decay into a bino LSP $(\widetilde{\chi}_1^0)$. The produced chargino $(\widetilde{\chi}_1^{\pm})$ that decays into the neutral bino must then emit a $W-$boson. However, the produced neutralino that decays into the neutral bino can emit either a $Z-$ or Higgs boson. To handle this, the branching ratio of the second lightest neutralino $(\widetilde{\chi}_2^0)$ is left as a free parameter and scanned over 0%, 25%, 50%, 75% and 100%, setting $\mathcal{B}(\widetilde{\chi}_2^0 \to Z\widetilde{\chi}_1^0)(= 1 - \mathcal{B}(\widetilde{\chi}_2^0 \to h\widetilde{\chi}_1^0))$ for each model.

For the $(\widetilde{H}, \widetilde{B})$ model, there is the additional heavy neutral higgsino $(\widetilde{\chi}_3^0)$ to consider, where the branching ratios will be fixed with respect to those of $\widetilde{\chi}_2^0$ by:

- $\mathcal{B}(\widetilde{\chi}_2^0 \to Z\widetilde{\chi}_1^0) + \mathcal{B}(\widetilde{\chi}_3^0 \to Z\widetilde{\chi}_1^0) = 1$,
- $\mathcal{B}(\widetilde{\chi}_2^0 \to h\widetilde{\chi}_1^0) + \mathcal{B}(\widetilde{\chi}_3^0 \to h\widetilde{\chi}_1^0) = 1$.

These provide a good approximation as long as $\Delta m(\widetilde{\chi}_{\text{heavy}}, \widetilde{\chi}_{\text{light}})$ is significantly larger than m_h [10].

For the $(\widetilde{W}, \widetilde{H})$ and $(\widetilde{H}, \widetilde{W})$ models the branching ratios are largely dictated by three MSSM parameters. These are the wino mass parameter(M_2), higgsino mass parameter(μ), and the vacuum expectation values

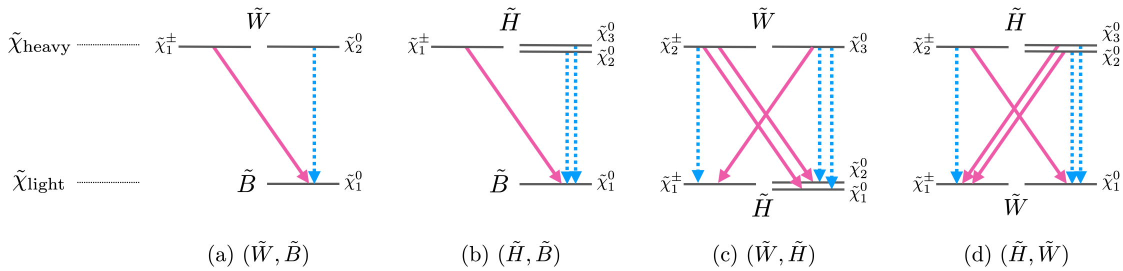

Figure 4.1: Mass spectra and mass eigenstates for each model in the bino/wino/higgsino LSP scenario. Solid arrows indicate decay modes that emit a W-boson while dashed arrows represent a decay that emits a $Z-$ or Higgs boson.

ratio of the two Higgs fields ($\tan\beta$). For any given set of these values the branching ratios are derived using SUSY-HIT 1.6.1 [11]. The mass parameters of all decoupled SUSY particles are set to 7 TeV and the signal models are tested for various combinations of the three MSSM parameters.

Most previous eletroweakino searches at the LHC have targeted the simplified $(\widetilde{W}, \widetilde{B})$ model. In these, only a specific production channel and decay mode are considered, as described in Section 4.2.2.2. For the $\widetilde{\chi}_1^{\pm}\widetilde{\chi}_1^{\mp}$ production decaying into WW, $m(\widetilde{\chi}_1^{\pm}) < 400$ GeV were excluded for $m(\widetilde{\chi}_1^0) < 200$ GeV [12, 13]. For $\widetilde{\chi}_1^{\pm}\widetilde{\chi}_2^0$ production, $m(\widetilde{\chi}_1^{\pm}/\widetilde{\chi}_2^0) < 640$ GeV were excluded for $m(\widetilde{\chi}_1^0) < 300$ GeV when $\widetilde{\chi}_2^0$ decays 100% into Z and $\widetilde{\chi}_1^0$ [14–18], and $m(\widetilde{\chi}_1^{\pm}/\widetilde{\chi}_2^0) < 740$ GeV were excluded for $m(\widetilde{\chi}_1^0) < 250$ GeV [19–24] when $\widetilde{\chi}_2^0$ decays entirely into h and $\widetilde{\chi}_1^0$. This analysis considers the simplified models as well in order to compare with previous results.

4.1.2 GGM scenario with gravitino-LSP: $(\widetilde{H}, \widetilde{G})$

The second model is general gauge mediation (GGM)[25–29], which has a nearly massless gravitino ($\tilde{G}$) as the primary LSP candidate. In this model a relatively light higgsino triplet is produced and decays into a gravitino LSP. This model has been explored in ATLAS [30, 31] and CMS [18], as illustrated in Figure 4.2.

All four production modes are considered: $\widetilde{\chi}_1^{\pm}\widetilde{\chi}_1^{\mp}$, $\widetilde{\chi}_1^{\pm}\widetilde{\chi}_2^0$, $\widetilde{\chi}_1^{\pm}\widetilde{\chi}_1^0$, $\widetilde{\chi}_1^0\widetilde{\chi}_2^0$. A small higgsino-gravitino coupling is considered where the heavy higgsinos always decay into a gravitino via the lightest higgsino $\widetilde{\chi}_1^0$. The

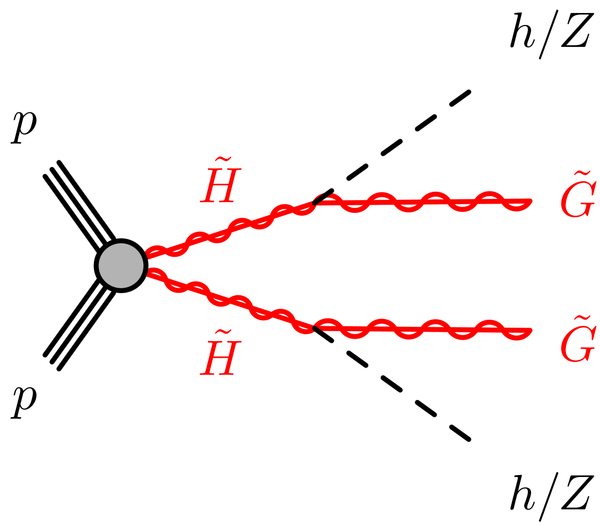

Figure 4.2: Diagram of N2N1 production in the gravitino model where higgsino triplets are represented by $\tilde{H}$.

$\tilde{\chi}_1^0$ is considered to have a short enough lifetime to be considered a prompt decay. In this model the light higgsino decays into the LSP and either a $Z-$ or Higgs boson. The branching ratio between the Z decay and h decay is treated as a free parameter and scanned in the limit setting.

4.1.3 QCD axion SM extension with axino-LSP: $(\widetilde{H}, \tilde{a})$

The final considered model is the naturalness-driven axino. In this model the axino ($\tilde{a}$) is the primary LSP candidate. This model comes from the "strong CP problem". The QCD Lagrangian allows for CP violation, but this has not been observed. This would require a highly unnatural tuning of the parameters. An additional chiral U(1) symmetry is introduced by the Peccei-Quinn mechanism [32] which causes the CP violating term to vanish and instead leave a Nambu-Goldstone boson [33, 34]. This boson is known as the axion and the super-partner is the axino.

This model includes a light higgsino triplet as well with the same 4 signal production modes as the previous model. The $\tilde{\chi}_1^0$ undergoes a prompt decay to an $\tilde{a}$ and a $Z-$ or Higgs boson where the branching ratio is once again scanned over. The decay is illustrated in Figure 4.3.

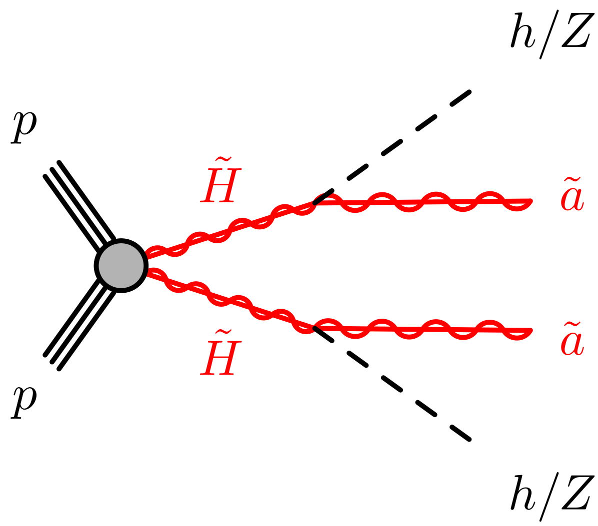

Figure 4.3: Diagram of N2N1 production in the axino model where higgsino triplets are represented by $\tilde{H}$.

The main way this model differs from the GGM scenario is that it allows for a massive LSP unlike the (nearly) massless Gravitino. The mass range studied in this analysis is $m(\tilde{a}) < 500$GeV.

4.2 Datasets and Monte Carlo Samples

4.2.1 Data Samples

The data used in this analysis was collected by the ATLAS detector during stable beam conditions at the LHC while running at $\sqrt{s} = 13$ TeV from 2015-2018. This dataset corresponds to an integrated luminosity of 139 fb^{-1} [35]. The data must satisfy the "Good Run List" selection requirements including that the ATLAS detector was running properly and magnetic fields were operating as expected.

For an event to be accepted they must have sufficient missing trasverse momentum. This acceptance requires

Events are selected by a trigger that requires high missing transverse momentum. For online MET this requirement varied from $E_T^{miss} > 70$ up to $E_T^{miss} > 110$ GeV, where the threshold increases with

Model	Production	Final states	SRs simultaneously fitted	Branching ratio
$(\widetilde{W},\widetilde{B})$	$\tilde{\chi}_1^\pm\tilde{\chi}_1^\mp$, $\tilde{\chi}_1^\pm\tilde{\chi}_2^0$	WW, WZ, Wh	4QVV, 2B2QWZ, 2B2QWh	$\mathcal{B}(\tilde{\chi}_1^\pm \to W\tilde{\chi}_1^0) = 1$, $\mathcal{B}(\tilde{\chi}_2^0 \to Z\tilde{\chi}_1^0)$ scanned.
$(\widetilde{H},\widetilde{B})$	$\tilde{\chi}_1^\pm\tilde{\chi}_1^\mp$, $\tilde{\chi}_1^\pm\tilde{\chi}_2^0$, $\tilde{\chi}_1^\pm\tilde{\chi}_3^0$, $\tilde{\chi}_2^0\tilde{\chi}_3^0$	WW, WZ, Wh, ZZ, Zh, hh	4QVV, 2B2QVZ, 2B2QVh	$\mathcal{B}(\tilde{\chi}_1^\pm \to W\tilde{\chi}_1^0) = 1$, $\mathcal{B}(\tilde{\chi}_2^0 \to Z\tilde{\chi}_1^0)$ scanned, $\mathcal{B}(\tilde{\chi}_3^0 \to h\tilde{\chi}_1^0) = 1 - \mathcal{B}(\tilde{\chi}_2^0 \to Z\tilde{\chi}_1^0)$
$(\widetilde{W},\widetilde{H})$	$\tilde{\chi}_2^\pm\tilde{\chi}_2^\mp$, $\tilde{\chi}_2^\pm\tilde{\chi}_3^0$	WW, WZ, Wh, ZZ, Zh, hh	4QVV, 2B2QVZ, 2B2QVh	Determined from $(M_2, \mu, \tan\beta)$.
$(\widetilde{H},\widetilde{W})$	$\tilde{\chi}_2^\pm\tilde{\chi}_2^\mp$, $\tilde{\chi}_2^\pm\tilde{\chi}_2^0$, $\tilde{\chi}_2^\pm\tilde{\chi}_3^0$, $\tilde{\chi}_2^0\tilde{\chi}_3^0$	WW, WZ, Wh, ZZ, Zh, hh	4QVV, 2B2QVZ, 2B2QVh	Determined from $(M_2, \mu, \tan\beta)$.
$(\widetilde{H},\widetilde{G})$	$\tilde{\chi}_1^\pm\tilde{\chi}_1^\mp$, $\tilde{\chi}_1^\pm\tilde{\chi}_1^0$, $\tilde{\chi}_1^\pm\tilde{\chi}_2^0$, $\tilde{\chi}_1^0\tilde{\chi}_2^0$	ZZ, Zh, hh	4QZZ, 2B2QZZ, 2B2QZh	$\mathcal{B}(\tilde{\chi}_1^0 \to h\widetilde{G})$ scanned.
$(\widetilde{H},\tilde{a})$	$\tilde{\chi}_1^\pm\tilde{\chi}_1^\mp$, $\tilde{\chi}_1^\pm\tilde{\chi}_1^0$, $\tilde{\chi}_1^\pm\tilde{\chi}_2^0$, $\tilde{\chi}_1^0\tilde{\chi}_2^0$	ZZ, Zh, hh	4QZZ, 2B2QZZ, 2B2QZh	$\mathcal{B}(\tilde{\chi}_1^0 \to h\tilde{a})$ scanned.
$(\widetilde{W},\widetilde{B})$ simplified models: $(\widetilde{W},\widetilde{B})$-SIM				
C1C1-WW	$\tilde{\chi}_1^\pm\tilde{\chi}_1^\mp$	WW	4QWW	$\mathcal{B}(\tilde{\chi}_1^\pm \to W\tilde{\chi}_1^0) = 1$.
C1N2-WZ	$\tilde{\chi}_1^\pm\tilde{\chi}_2^0$	WZ	4QWZ, 2B2QWZ	$\mathcal{B}(\tilde{\chi}_1^\pm \to W\tilde{\chi}_1^0) = \mathcal{B}(\tilde{\chi}_2^0 \to Z\tilde{\chi}_1^0) = 1$.
C1N2-Wh	$\tilde{\chi}_1^\pm\tilde{\chi}_2^0$	Wh	2B2QWh	$\mathcal{B}(\tilde{\chi}_1^\pm \to W\tilde{\chi}_1^0) = \mathcal{B}(\tilde{\chi}_2^0 \to h\tilde{\chi}_1^0) = 1$.

Table 4.1: Summary of the production modes, final states, signal regions (SRs) used for the hypothetical tests and the branching ratio assumptions for the signal models targeted in the search. The $(\widetilde{W},\widetilde{B})$ and $(\widetilde{H},\widetilde{G})$ models are used for optimizing the selection, and the remainder are considered for interpretation. For the $(\widetilde{W},\widetilde{H})$ and $(\widetilde{H},\widetilde{W})$ models, various values of the three MSSM paramaters are considered. For M_2 and μ the values 0–1.2 TeV and −1.2 TeV–1.2 TeV respectively are scanned over and the values of 2, 5, 10, and 30 are tested for $\tan\beta$. The $(\widetilde{W},\widetilde{B})$ simplified models are also interpreted in this analysis in order to compare with past ATLAS electroweakino search results.

instantaneous luminosity during the data taking [36]. For offline $E_{\mathrm{T}}^{\mathrm{miss}}$is required to be at above 200 GeV when reconstructed in order to be in the plateau of the trigger efficiency turn-on curve, where acceptance efficiency reaches 100%. This search uses this requirement as well.

4.2.2 Monte Carlo Simulation

Monte Carlo (MC) simulations are used for modeling SM backgrounds as well as the signals that contribute to the analysis region. These are used during the development stage. The same trigger and reconstruction algorithms are used for the simulated evenst and the data. Scale factors are employed to correct simulated lepton and photon trigger efficiencies to match those of the data reconstruction. The scale factors depend on p_{T} and η of the leptons and photons, derived from control samples [37, 38].

4.2.2.1 SM Backgrounds

ATLAS centrally produces all MC for SM backgrounds. The backgrounds considered in this analysis are di-boson, tri-boson, W+jets, Z+jets, QCD multijet, $t\bar{t}$+SM bsosons, and single top.

Diboson events include WW, WZ, and ZZ. These events with fully-leptonic decays are simulated using the SHERPA v2.2.1 [39] (for $\nu\nu\nu\nu$) or v2.2.2 ($\ell\ell\ell\ell$, $\ell\ell\ell\nu$, $\ell\ell\nu\nu$ and $\ell\nu\nu\nu$) generator. Matrix elements for WW, WZ, and ZZ processes at next-to-leading order accuracy in QCD for up to one additional parton and leading order accuracy for up to three additional partons emitted. All processes with four or six electroweak vertices are included. Semi-leptonic decays ($\ell\nu qq$, $\ell\ell qq$ and $\nu\nu qq$) are simulated with SHERPA v2.2.1 as well. Only on-shell bosons are considered and all-hadronic diboson contributions are ignored as the $E_T^{miss} > 200$ GeV cut makes them negligible.

Tri-boson production includes WWW, WWZ, WZZ, and ZZZ events. Only cases with one leptonically decaying boson and two hadronically decaying boson are considered. These processes are generated using MADGRAPH5_aMC@NLO v2.6.6 at leading order.

Events containing a leptonically-decaying W or Z boson that are associated with hadron jets are produced using SHERPA v2.2.1 generator. The matrix elements are calculated using Comix [40] and OpenLoops [41, 42] generators for up to two partons at next-to-leading order and four partons and leading order accuracy. Events are normalized to the next-to-next-to-leading order QCD cross sections.

The QCD multijet processes are simulated with SHERPA using CT10 parton distribution function (PDF) tune.

$t\bar{t}$ and single-top ($t + X$) events are generated with POWHEG-BOX [43–46] v2 at next-to-leading order with the `NNPDF30nlo` PDF sets. The parton showering is simulated using PYTHIA8 with the `NNPDF23lo` PDF set and the A14 tune. $t\bar{t}$events are normalized to next-to-nex-to-leading order QCD including next-to-next-to-leading logarithmic soft-gluon terms [47–49]. Single-top events use next-to-leading order cross sections.

4.2.2.2 Signal

Five of the signal models considered in this analysis, $(\widetilde{W}, \widetilde{B})$, $(\widetilde{H}, \widetilde{B})$, $(\widetilde{W}, \widetilde{H})$, $(\widetilde{H}, \widetilde{W})$, and $(\widetilde{H}, \tilde{a})$, are simulated by combining the simplified model signals. Six sets of simplified models are generated to cover the different final states, these are derived as variants of the models with a bino LSP ($(\widetilde{W}, \widetilde{B})$ and $(\widetilde{H}, \widetilde{B})$). These six simplified models are:

- wino pair production, with each decaying into a bino LSP (denoted as $(\widetilde{W}, \widetilde{B})$ simplified models or $(\widetilde{W}, \widetilde{B})$-SIM):

  C1C1-WW: $\widetilde{\chi}_1^{\pm}\widetilde{\chi}_1^{\pm} \to WW\ \widetilde{\chi}_1^0\widetilde{\chi}_1^0 \quad (\mathcal{B}(\widetilde{\chi}_1^{\pm} \to W\widetilde{\chi}_1^0) = 100\%)$

  C1N2-WZ: $\widetilde{\chi}_1^{\pm}\widetilde{\chi}_2^0 \to WZ\ \widetilde{\chi}_1^0\widetilde{\chi}_1^0 \quad (\mathcal{B}(\widetilde{\chi}_1^{\pm} \to W\widetilde{\chi}_1^0) = \mathcal{B}(\widetilde{\chi}_2^0 \to Z\widetilde{\chi}_1^0) = 100\%)$

  C1N2-Wh: $\widetilde{\chi}_1^{\pm}\widetilde{\chi}_2^0 \to Wh\ \widetilde{\chi}_1^0\widetilde{\chi}_1^0 \quad (\mathcal{B}(\widetilde{\chi}_1^{\pm} \to W\widetilde{\chi}_1^0) = \mathcal{B}(\widetilde{\chi}_2^0 \to h\widetilde{\chi}_1^0) = 100\%)$,

- neutral higgsino pair production, with each decaying into bino LSP (denoted as $(\widetilde{H}, \widetilde{B})$-SIM):

  N2N3-ZZ: $\widetilde{\chi}_2^0\widetilde{\chi}_3^0 \to ZZ\ \widetilde{\chi}_1^0\widetilde{\chi}_1^0 \quad (\mathcal{B}(\widetilde{\chi}_2^0 \to Z\widetilde{\chi}_1^0) = \mathcal{B}(\widetilde{\chi}_3^0 \to Z\widetilde{\chi}_1^0) = 100\%)$

  N2N3-Zh: $\widetilde{\chi}_2^0\widetilde{\chi}_3^0 \to Zh\ \widetilde{\chi}_1^0\widetilde{\chi}_1^0 \quad (\mathcal{B}(\widetilde{\chi}_2^0 \to Z\widetilde{\chi}_1^0) = \mathcal{B}(\widetilde{\chi}_3^0 \to h\widetilde{\chi}_1^0) = 100\%)$

  N2N3-hh: $\widetilde{\chi}_2^0\widetilde{\chi}_3^0 \to hh\ \widetilde{\chi}_1^0\widetilde{\chi}_1^0 \quad (\mathcal{B}(\widetilde{\chi}_2^0 \to h\widetilde{\chi}_1^0) = \mathcal{B}(\widetilde{\chi}_3^0 \to h\widetilde{\chi}_1^0) = 100\%)$.

The kinematics of each final state are modeled by these samples where the $(\widetilde{W}, \widetilde{B})$-SIM samples are used to model events containing WW, WZ or Wh and $(\widetilde{H}, \widetilde{B})$-SIM samples are used for events with ZZ, Zh or hh. A reweighting is applied based on the production cross-sections and $\widetilde{\chi}_{\text{heavy}}$ branching ratios in the model. The main assumption of this method is that the event kinematics rely on only $m_{\widetilde{\chi}_{\text{light}}}$and $m_{\widetilde{\chi}_{\text{heavy}}}$. This means the kinematics are independent of production modes, LSP type, or any other MSSM variable.

The $(\widetilde{H},\widetilde{G})$ model has a dedicated sample generated with all production modes ($\widetilde{\chi}_1^{\pm}\widetilde{\chi}_1^{\mp}$, $\widetilde{\chi}_1^{\pm}\widetilde{\chi}_1^0$, $\widetilde{\chi}_1^{\pm}\widetilde{\chi}_2^0$, $\widetilde{\chi}_1^0\widetilde{\chi}_2^0$) included.

All SUSY samples are generated using leading order matrix elements with up to two additional partons by the MadGraph [50] v2.6.1 generator. Parton showering and hadronization is simulated with Pythia 8.230 [51]. The PDF used for the simulation is `NNPDF23lo` with the Pythia A14 set of tuned underlying event and shower parameters. The masses of all SM particles are set to their SM values while decoupled SUSY particles are set with a mass of 3 TeV.

Pythia is used to simulate the decays of produced electroweakinos. As seen above, for the $(\widetilde{W},\widetilde{B})$-SIM and $(\widetilde{H},\widetilde{B})$-SIM signals, the branching ratios are set to 100% for the relevant decay mode in each set of samples. In the $(\widetilde{H},\widetilde{G})$ signal, the heavy higgsinos ($\widetilde{\chi}_1^{\pm}$,$\widetilde{\chi}_2^0$) are defined to be 0.5 GeVheavier than the lightest higgsino ($\widetilde{\chi}_1^0$) in mass and to decay entirely into $\widetilde{\chi}_1^0$ and soft particles. EvtGen [52] v1.2.0 is used to simulate the decays of bottom and charm hadrons.

4.3 Object Definitions

This section describes the primary objectes and defines the methods used to reconstruct them for this analysis. There are two classes of selection criteria used for reconstructed objects, which is common for many SUSY analyses. These are "baseline" and "signal" objects. Baseline objects are defined with a loose criteria and are used to define the final states more broadly and create orthogonal regions. The signal selection includes additional requirements to give a tight criteria used to carefully select a signal region. the signal criteria is optimized to reject incorrectly identified objects, also referred to as fakes, and pileup contribution.

An overlap removal will be applied to both sets of objects and is described at the end of the section. A subset of these objects are also used in the extrapolation to this study in Chapter 5.

Baseline electron candidates are reconstructed from electromagnetic clusters formed by energy deposits in the ECAL consistent with tracks in the inner detector using the super-cluster algorithm. Electrons are required to have $p_{\mathrm{T}} > 4.5$ GeV and $|\eta| < 2.47$, and meet the *Loose* criteria of the likelihood-based identification [53]. For signal electrons this requirement is increased to $p_{\mathrm{T}} > 10$ GeV and the *Tight* criteria is imposed. Additionally for baseline electrons, a longitudinal impact paramater requirement is imposed, $z_0 \sin\theta < 0.5$ mm, to reject fake electrons originating from pileup jets. The transverse impact parameter is required to satisfy $|d_0/\sigma(d_0)| < 5$ for signal electrons in order to reduce non-prompt electrons from heavy hadron decays.

Muons are reconstructed using the "combined muon algorithm" **??** which selects tracks from the inner detector that are consistent with those from the muon spectrometer. Baseline muons must have $p_{\mathrm{T}} > 3$ GeV and $|\eta| < 2.7$, and to meet the *Medium* [54] identification criteria defined for muons. For muons a longitudinal impact paramater requirement, $z_0 \sin\theta < 0.5$ mm, is imposed for the baseline class. Signal muons also require $p_{\mathrm{T}} > 10$ GeVand the transverse impact parameter to satisfy $|d_0/\sigma(d_0)| < 3$. The *Tight* working point is required for signal muons as well.

It is important to note that this is a 0-lepton analysis, so there must be exactly zero leptons that pass the baseline criteria. The event selection efficiency is therefore sensitive to the baseline definition of both lepton flavors. The above kinematic values and identification criterea were selected after comparing a variety of working points for the acceptace rate of 0-lepton events and 1-lepton rejection efficiency after overlap removal. The signal criteria for leptons is only used in this analysis for validation of the background estimations.

Small-R jet candidates are reconstructed from particle-flow objects [55] using the anti-k_t algorithm with a radius parameter of $R = 0.4$. Baseline small-R jets are required to be within $|\eta| < 4.5$ and have $p_{\mathrm{T}} > 30$ GeV. Signal small-R jets are selected to be within $|\eta| < 2.8$ and any with $p_{\mathrm{T}} < 120$ GeV and $|\eta| < 2.5$ must also satisfy the *Tight* quality criteria of the track-based jet vertex tagger [56, 57] in order to suppresses jets originating from pileup. Note that in this analysis small-R jets are only used directly for $E_{\mathrm{T}}^{\mathrm{miss}}$calculation and in the kinematic variable min $\Delta\phi(E_{\mathrm{T}}^{\mathrm{miss}}, j)$.

Finally, the primary physics objects used in this study are large-radius jets (large-R jets). These are defined with a radius parameter of $R = 1.0$. They are reconstructed from locally calibrated topo-clusters

[58] using the anti-k_t algorithm [59] in the FastJet package [60]. To remove contributions from underlying events and pileup a trimming algorithm [61] is applied to mitigate the effects of pileup and soft radiation. The constituents of each jet are reclustered with the k_t algorithm [62] into $R = 0.2$ subjets, these are removed if they carry under 5% of the original jet p_{T}. The jet mass, m_J, is calculated based on the combined mass prescription [63] to have the best mass resolution. This is achieved by taking the weighted sum of masses computed using the calorimeter and tracking information. The $p_{\mathrm{T}}$and mass scales are initially calibrated using simulation, followed by an in situ calibration [64] to correct for residual differences between data and MC simulation. Baseline large-R jets used in the analysis are selected with $p_{\mathrm{T}} > 200$ GeV, $|\eta| < 2.0$, and $m_J > 40$ GeV.

Two types of boosted boson tagging are applied on the preselected large-R jets to identify SM boson decays within each structure. The first is to tag light-flavor quarks, $W_{qq}(Z_{qq})$-tagging targeting $W(Z) \to qq$. The second focuses on tagging specifically b-quarks, $Z_{bb}(h_{bb})$-tagging targeting $Z(h) \to bb$. In this note, large-R jets are often referred to in this way, by the boson which is tagged, and whose decay appears to be the origination of the large-R jet, as well as by the quark content of the jet.

The primary variables used in boosted boson tagging are large-R jet mass (m_J), the energy correlation function (D_2), and track multiplicity (n_{trk}). The D_2 variable is defined as the ratio of three-point to two-point energy correlation functions [65, 66]. These variables can be thought of as 3-prongness and 2-prongness respectively and are based on the energies and pairwise angular separations of particles within a jet. The definition is:

$$D_2 = E_{CF3}(\frac{E_{CF1}}{E_{CF2}})^3 \tag{4.1}$$

Where the energy correlation functions are defined as:

$$E_{CF1} = \sum_i p_{\mathrm{T},i} \tag{4.2}$$

$$E_{CF2} = \sum_{i,j} p_{\mathrm{T},i}\ p_{\mathrm{T},j}\ \Delta R_{ij} \tag{4.3}$$

$$E_{CF3} = \sum_{i,j,k} p_{\mathrm{T},i}\ p_{\mathrm{T},j}\ p_{\mathrm{T},k}\ \Delta R_{ij} \Delta R_{jk} \Delta R_{ki} \tag{4.4}$$

Events with a 2-prong structure will have a low D_2 but 1-prong and 3-prong events will both have large D_2 values. Track multiplicity, n_{trk}, is the number of tracks that, before trimming is applied, are matched to the large-R jet by ghost-association [67]. The selections are optimized separately for targeting W and Z bosons. The cut values applied to m_J and D_2 are the same as for the "50% efficiency W/Z tagger" in Ref. [68]; an n_{trk} cut, loosened from ≤ 26 to ≤ 32 (34) for the $W_{qq}(Z_{qq})$-tagging, is applied in this analysis to achieve the optimum sensitivity and better modeling in MC simulation. In order to maintain orthogonality with $Z_{bb}(h_{bb})$-tagging, the b-jet multiplicity of the large-R jet is required to be less than two.

A generic large-R jet which contains two light flavor (b-) quarks is referred to as J_{qq} (J_{bb}) and defined by the boson tagging process. A large-R jet that originates from a particle tagged as a W boson and contains two light flavor quarks is referred to as W_{qq}. Similarly a large-R jet that originates from a particle tagged as a Z boson and contains two light flavor (b-)quarks is referred to as Z_{qq} (Z_{bb}). Finally, a particle tagged as a h boson whose decay is the origination point of a large-R jet containing 2 b-quarks is referred to as h_{bb}. To be identified as any of these, a large-R jet must pass the requisite tagging. This includes having the proper number of either light flavor or b-quarks tagged within the radius of the large-R jet (J_{qq} or J_{bb} tagging) as well as the reconstructed jet being consistent with the appropriate mass range as defined next.

One of the tools used to identify which boson a jet originated from is the missing transverse momentum, $p_{\mathrm{T}}^{\mathrm{miss}}$, which has a magnitude of $E_{\mathrm{T}}^{\mathrm{miss}}$. The SUSYTools package with *Tight* is used to reconstruct the $p_{\mathrm{T}}^{\mathrm{miss}}$and $E_{\mathrm{T}}^{\mathrm{miss}}$. $p_{\mathrm{T}}^{\mathrm{miss}}$is the negative vector sum of all momenta of identified physics objects as well as a soft term

$E_{\mathrm{T}}^{\mathrm{miss}}$requirements are also heavily used to include any requirements imposed by $E_{\mathrm{T}}^{\mathrm{miss}}$triggers (these are discussed in Section 5.6.1), define particle tagging that is used in the analysis, and provide background rejection cuts. For this analysis light quark jets are tagged as originating from a W or Z boson with a dynamic mass window cut versus $p_{\mathrm{T}}$where the W boson typically has a mass between 65 GeV and 95 GeV while the Z boson is generally from 75 GeV to 105 GeV. In the b-tagged jets however, the Z boson is tagged with a fixed mass window cut with an upper limit of 100 GeV in order to maintain orthogonality with the

h boson tagged jets. This requires the jet mass to be in the range 70 GeV $< m_J <$ 100 GeV for the Z_{bb} tagging and for h_{bb} tagging within the range 100 GeV $< m_J <$ 135 GeV. To ensure clarity, this does means the allowed mass range is defined differently for Z_{qq} and Z_{bb} jets. In order to improve the mass peak resolution, the jet mass is corrected by adding the momentum of the highest-p_{T}muon identified within the large-R jet. This is shown visually in Figure 5.3. Notably, this shows the overlap between the mass window for the W- and Z bosons in the light quark jets and the orthogonality of Z and h bosons in the b-tagged jets.

All objects, both baseline and signal, undergo a process of overlap removal. This procedure ensures there is no double counting objects in any events, for example electrons with high energies can sometimes be recorded as jets so the overlap removal ensures that if that happens only one object is used. Electron, muon, and small-R jet collections are all checked to see if any share tracks in the inner detector or overlap in ΔR. Any objects that overlap or share those tracks will be removed.

The first step in overlap removal checks all small-R jets and removes any that satisfy $\Delta R(e, j) < 0.2$ or $\Delta R(\mu, j) < 0.4$ and have 2 or fewer ghost-associated tracks for the jet. Jets that fit this criteria most likely originated from electron showers or muon braking radiation from calorimeter energy deposits. This step is skipped if a jet is tagged as contianing b-quarks and has p_{T}< 250 GeV. Any electrons or muons with $\Delta R < 0.4$ between the lepton and a small-R jet that remains are discarded. Next any muons matched to an energy deposit in the calorimeter that share an ID track with an electron are removed. Finally any electrons that share ID tracks with any remaining muons are discarded. After the completion of this overlap removal, one additional stage of removal is applied for large-R jets. Any that are found within $\Delta R(e, J) < 1.0$ of a remaining electron are removed.

4.4 Event Selection

The primary physics objects used in this study are large-radius jets (large-R jets). These are defined with a radius parameter of R = 1.0. They are reconstructed from locally calibrated topo-clusters [58] using the anti-k_t algorithm [59] in the FastJet package [60].

4.4.1 Pre-selection

First a set of pre-selection and cleaning cuts are applied for all events. A trigger cut of $E_T^{miss} > 200$ GeV is applied as well as requiring at least one isolated electron, muon, of photon. At least one vertex with two or more tracks with $p_T > 500$ MeV is required and the primary vertex is defined as the vertex with the largest Σp_T^2 of all tracks.

Next a set of cleaning cuts are applied to ensure quality of energy measurements. A veto is applied to any events where a baseline muon that originates too far from the point of collision as these are consistent with cosmic muons.

Any events with a jet pointed to the tile hadronic calorimeter areas that were non-operational are vetoed as well as any events with a baseline muon with poor momentum measurements. Any events with a baseline jet that fails the *Loose* cleaning are removed. Events are required to contain at least two large-R jets. Events with three or more are not vetoed in order to be as inclusive as possible however, applied event selection is always based on the two highest-p_T large-R jets. Events with no baseline leptons are also selected. Both large-R jets are also required to pass boson tagging requirements. In order to suppress backgrounds that include top quarks it is also required that there are no b-quarks in the event that are not matched with one of the two leading large-R jets by the ΔR < 1.0 criterion.

4.4.2 Signal Region Definition

Two orthogonal signal regions are defined in the Run 2 paper, 4Q and 2B2Q. These regions are defined by the presence of a large-R jet containing exactly two b-tagged jets ($J_b b$) for the qqbb final states (2B2Q region) and absence of such a large-R jet for the qqqq final states (4Q region). Boson tagging is applied to the two leading large-R jets, this requires them to pass V_{qq} tagging for the 4Q signal region (n(V_{qq})=2). In the case of the 2B2Q region this requires the J_{bb} to be tagged as either a Z or h boson, denoted $Z_{bb} and h_{bb}$. It also requires the other jet (J_{qq}) to pass the V_{qq} tagging.

	$n(W_{qq})$	$n(Z_{qq})$	$n(V_{qq})$	$n(Z_{bb})$	$n(h_{bb})$
4Q-WW	= 2	-	= 2	= 0	= 0
4Q-WZ	≥ 1	≥ 1	= 2	= 0	= 0
4Q-ZZ	-	= 2	= 2	= 0	= 0
4Q-VV	-	-	= 2	= 0	= 0
2B2Q-WZ	= 1	-	= 1	= 1	= 0
2B2Q-ZZ	-	= 1	= 1	= 1	= 0
2B2Q-Wh	= 1	-	= 1	= 0	= 1
2B2Q-Zh	-	= 1	= 1	= 0	= 1
2B2Q-VZ	-	-	= 1	= 1	= 0
2B2Q-Vh	-	-	= 1	= 0	= 1

Table 4.2: Definition of each SR in the 4Q and 2B2Q categories. $n(W_{qq})$, $n(Z_{qq})$, $n(V_{qq})$, $n(Z_{bb})$, and $n(h_{bb})$ are respectively the number of large-R jets that pass the W_{qq}-, Z_{qq}-, V_{qq}-, Z_{bb}-, and h_{bb}-tagging of two leading large-R jets. Note that 4QWZ requires $n(W_{qq}), n(Z_{qq}) \geq 1$ rather than $n(W_{qq}), n(Z_{qq}) = 1$ because the selection of W_{qq}- and Z_{qq}-tagging are not exclusive. Fig 4.4 shows the overlap between the SRs.

Both of these SR categories have multiple SRs within them. For the 4Q region these include WW, WZ, and ZZ. Where these require the leading large-R jets to pass two W_{qq} tagging, one W_{qq} and one Z_{qq} tag, and two Z_{qq} tags respectively. The union of these three SRs is denoted VV and covers all signals where $\tilde{\chi}_{heavy}$ has branching ratios into W and Z. In the same way the 2B2Q category contains WZ, Wh, ZZ, and Zh where the first two contain a W_{qq}-tagged boson and the latter two a Z_{qq}-tagged boson. Then the second large-R jet contains the necessary Z_{bb}- or h_{bb}-tagging. This gives the VZ(Vh) regions which contain WZ and ZZ(Wh and Zh).

The SR definitions are summarized in Table 4.2 and illustrated in Figure 4.4. In total four and six SRs are defined for SR-4Q and SR-2B2Q regions respectively. SR-4QXX, SR-2B2QXZ, and SR-2B2QXh (X := W/Z) are mutually orthogonal and are statistically combined according to the models.

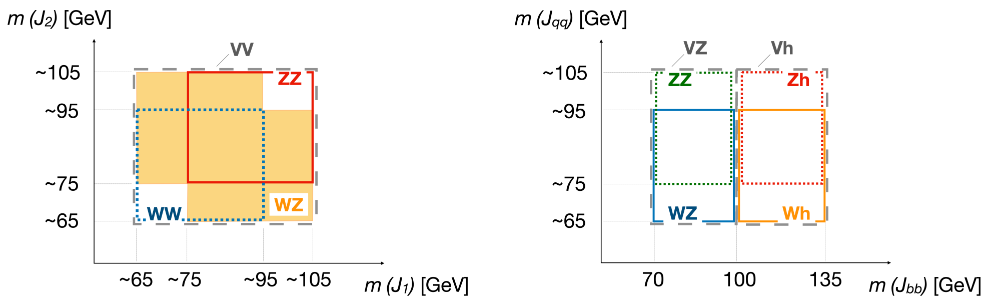

Figure 4.4: The SR segmentation is shown defined by the masses of the two leading large-R jets. In SR4Q (left), both jets are required to pass the W_{qq}- or Z_{qq}-tagging. In SR2B2Q (right), one jet is required to contain exactly two b-tagged track jets (J_{bb}) while the other has at most one (J_{qq}). The mass of J_{bb} is required to be consistent with Z ($70-100$ GeV) or h ($100-135$ GeV), while the J_{qq} is required to pass the W_{qq}- or Z_{qq}-tagging. The W_{qq}-/Z_{qq}-tagging has a variable mass window depending on p_{T}, the typical cut values are indicated. The inclusive SRs (VV, VZ, and Vh) defined by the logical union of two or three mutually overlapping SRs are indicated by the gray dashed lines.

4.4.3 Kinematic Selections

The main SM backgrounds at this stage are $Z(\rightarrow \nu\nu)+$jets, $W+$jets and $t\bar{t}$. A set of background rejection cuts are studied, optimized, and applied to supress these backgrounds.

The number of b-tagged track-jets in the event is required to be less than two within the 4Q category to further reduce the $t\bar{t}$background. At this point kinematic cuts are applied and optimized for each SR. The effective mass variable, m_{eff}, is defined as the sum of E_T^{miss} and the p_T of the two leading large-R jets. It is used with $E_{\mathrm{T}}^{\mathrm{miss}}$to select hard event kinematics. For the 4Q region, $E_{\mathrm{T}}^{\mathrm{miss}} > 300$ GeV and $m_{\mathrm{eff}} > 1300$ GeV are applied In the 2B2Q region slightly looser cuts are applied at $E_{\mathrm{T}}^{\mathrm{miss}} > 200$ GeV and $m_{\mathrm{eff}} > 0300$ GeV.

Event shape is also useful to distinguish signals from backgrounds. Signal events tend to have a relatively spherical shape and the jets are typically isolated from E_T^{miss}. This is because the the heavy electroweakinos are produced nearly at rest. On the other hand, background events have a much higher chance of containing a jet that is aligned with a boson. This can be due to boosted top decays in $t\bar{t}$events, or in $Z(\rightarrow \nu\nu)+$jets and $W+$jets, emition of collinear radiation. This motivates defining the variable min.$\Delta\phi(E_T^{miss}$, j) which is the minimum azimuthal angle of seperation between E_T^{miss} and the nearest small-R jet. In both SR categories min.$\Delta\phi(E_T^{miss}$, j)>1.0 is required.

The strasverse mass variable, m_{T2} [69, 70], is also defined for the 2B2Q category. m_{T2} is an event variable that bounds the momenta of two unseen particles which have decayed semi-visibly. It is a function of the momenta of the two visible particles and missing transverse momentum in an event. The stransverse mass is constructed by assigning the two leading large-R jets to the visible particle legs and is shown to effectively suppress some SM backgrounds, particularly $t\bar{t}$ which exhibits a kinematic cutoff around $m_{T2} = 200$ GeV. The requirement, $m_{\mathrm{T2}} > 250$ GeV, effectively suppresses this background and is applied for the 2B2Q SRs.

Within all SR4Q and SR2B2Q categories equivalent kinematic selections are made. Sensitivity to the $(\widetilde{W}, \widetilde{B})$ model at a mass splitting of $(m_{\widetilde{W}}, m_{\widetilde{B}}) = (900, 100)$ GeV is optimized and the kinematic cuts are applied for the SR4Q, SR2B2QWh, and SR2B2QVh regions. For SR2B2QWZ, SR2B2QZZ and SR2B2QVZ, kinematic selections are determined by optimizing the $(\widetilde{H}, \widetilde{G})$ model with $m_{\widetilde{H}} = 800$ GeV. These cuts are tested on other signal models and confirmed to be nearly optimal as well so to maintain simplicity no changes were made to kinematic cuts within a given category. The metric of sensitivity used for all optimizations is the discovery significance.

The various selections are summarized in Table 4.3 for all SRs, control regions (CRs), and validation regions (VRs). These CRs and VRs are used in background estimation, an in-depth discussion of their formation and application follows in Section 4.5.

4.5 Background Estimation

The most prominent SM backgrounds in the SRs are Z($\rightarrow \nu\nu$)+jets, W($\rightarrow l\nu$)+jets, and VV accounting for approximately 50%, 15-20%, and 10-20% respectively. The remainder of background in SR-4Q are VVV events and in SR-2B2Q $t\bar{t}$, single top, and $t\bar{t}$+X events.

There are two categories of backgrounds, reducible and irreducible. Irreducible backgrounds are cat-

	SR(CR0L) 4Q	SR(CR0L) 2B2Q	VR(CR)1L 4Q	VR(CR)1L 2B2Q	VR(CR)1Y 4Q	VR(CR)1Y 2B2Q	VRTTX
$n_{\text{Large-}R\text{ jets}}$	≥ 2		≥ 2		≥ 2		$= 1$
n_{lepton}	$= 0$		$= 1$		$= 0$		$= 3$
$p_{\text{T}}(\ell_1)$ [GeV]	-		> 30		-		> 30
n_{photon}	-		-		$= 1$		-
$n(V_{qq})$	$= 2\ (= 1)$	$= 1\ (= 0)$	$= 2\ (= 1)$	$= 1\ (= 0)$	$= 2\ (= 1)$	$= 1\ (= 0)$	-
$n(!V_{qq})$	$= 0\ (= 1)$	$= 0\ (= 1)$	$= 0\ (= 1)$	$= 0\ (= 1)$	$= 0\ (= 1)$	$= 0\ (= 1)$	-
$n(J_{bb})$	$= 0$	$= 1$	$= 0$	$= 1$	$= 0$	$= 1$	$= 1$
$m(J_{bb})$ [GeV]	-	$\in [70, 135\ (150)]$	-	$\in [70, 150]$	-	$\in [70, 150]$	-
$n_{b\text{-jet}}^{\text{unmatched}}$	$= 0$		$= 0$		$= 0$		-
$n_{b\text{-jet}}$	≤ 1	-	$= 0$	-	≤ 1	-	-
$E_{\text{T}}^{\text{miss}}$ [GeV]	> 300	> 200	> 50		< 200		-
$p_{\text{T}}(W)$ [GeV]	-		> 200		-		-
$p_{\text{T}}(\gamma)$ [GeV]	-		-		> 200		-
m_{eff} [GeV]	> 1300	$> 1000\ (> 900)$	> 1000	> 900	> 1000	> 900	-
$\min \Delta\phi(E_{\text{T}}^{\text{miss}}, j)$	> 1.0		> 1.0		> 1.0		-
m_{T2} [GeV]	-	> 250	-	> 250	-	> 250	-

Table 4.3: Summary of selections for the SRs, CRs, and VRs. $n(V_{qq})$ and $n(!V_{qq})$ are the number of large-R jets that pass and fail the V_{qq}-tagging between the two highest-p_{T}large-R jets respectively. The same selection is applied in the SR or VR and CR in the same category except for the V_{qq}-tagging and some kinematic selections that are explicitly indicated in parentheses.

egorized as backgrounds that include at least 2 hadronically decaying W/Z/h and a large E_T^{miss}. These backgrounds are VVV and $t\bar{t}$+X. The reducible backgrounds are ones that include fewer than 2 hadronically decaying bosons, meaning there must be at least one large-R jet that originates from something other than a boson decay. This is referred to as a ”fake boson jet” and this category contains the remainder of the SM backgrounds. The strategy for estimating reducible and irreducible backgrounds varies. Irreducible backgrounds are estimated using MC simulation. Reducible backgrounds are estimated using a semi-data driven method.

The irreducible backgrounds, VVV and $t\bar{t}$ + X, make up about 10% of the total backgrounds in SR-4Q and SR-2B2Q respectively and are negligible in the other region. Due to the minor contributions MC predictions are used to estimate the backgrounds directly, with conservative uncertainties assigned.

The LHC has only recently begun to observe VVV backgrounds so there is a very low data sample size. Loosening the selection in order to create a validation region causes very poor VVV purity because the sample size is so small. For this reason no control or validation region is designed. This background is estimated directly from MC predictions.

In the SR-2B2Q region $t\bar{t}$ + X is the dominant component, specifically $t\bar{t} \rightarrow bl\nu bqq$ + Z$\rightarrow$ $\nu\nu$. In order to assign a proper uncertainty to the MC estimation a validation region(VR) VRTTX is defined in the adjacent 3-lepton region. This region is populated primarily by $t\bar{t} \rightarrow bl\nu bqq$ + Z$\rightarrow$ ll. At least 1 large-R jet is required, which contains exactly 2 b-tagged jets. Three baseline and signal leptons with the leading lepton $p_T > 30$ GeV is required. To maintain sufficient data sample in the region no additional kinematic cuts are applied. There were 68 data events observed in VRTTX with 46.5 events predicted. 68% of the total events were predicted so a 70% uncertainty is assigned on the $t\bar{t}$ + X normalization. This has a small impact on the total background estimation given the minor contribution to SRs. The full set of selections are summarized in Table 4.3.

The remainder of the backgrounds are reducible backgrounds. For each SR a control region (CR) is defined. Each CR is defined as the respective SR except with one of the two leading large-R jets failing the V_{qq}-tagging. A diagram showing this selection can be seen in 4.5. Based on this the extrapolation from a CR0L to SR is characterized by the V_{qq}-tagging response of a fake boson jet. The m_{eff} selection ($>$ 1000 GeV to $>$ 900 GeV) and J_{bb} mass tagging (70-135 GeV to 70-150 GeV) are loosened for CR0L-2B2Q with respect to SR-2B2Q in order to maintain sufficient data sample size and minimize signal contamination. Signal contamination in CR0L-4Q and CR0L-2B2Q is evaluated using the ($\tilde{W}$,$\tilde{B}$)-SIM and ($\tilde{H}$,$\tilde{G}$) samples. Non-excluded signals can cause up to 15% and 24% of the expected backgrounds in CR0L-4Q and CR0L-2B2Q respectively. This introduced bias in the BG estimation is smaller than the uncertainty of the SRs and VRs, this it will have a small impact on the final sensitivity.

This CR0L definition comes with the benefit that all contributing physics processes have a comparable 0L transfer factor. The faked boson jets have similar origins and kinematics in all cases so the boson tagging efficiency is the same. This means the backgrounds can be treated as a single component with a common normalization factor assigned. The normalization is done in the 4Q and 2B2Q regions separately with an independent normalization factor. This means that the MC modeling of the 0L transfer factor is essential to the BG estimation. Data events with exactly one lepton or photon are used for this validation. The main

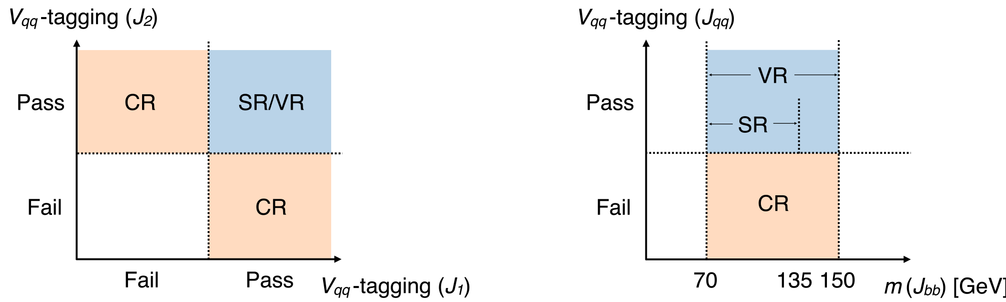

Figure 4.5: Schematics illustrating how the SRs, VRs, and CRs differ in terms of jet-tagging in the (a) 4Q and (b) 2B2Q categories. As described in Section 4.5, the CRs are defined by the inversion of the V_{qq}-tagging requirement for one of the two leading large-R jets in the SR or VR. The J_{bb} mass window cut is also loosened slightly in the CRs and VRs.

backgrounds Z→ $\nu\nu$ + jets, W→ $l\nu$ + jets, and γ + jets production have similar initial state radiation (ISR) jet kinematics for their respective regions (SR/CR0L, 1-lepton, 1-photon).

A background only fit is performed where the sum of the reducible backgrounds in the MC sample is normalized to the data in each CR. The agreement between the data and post-fit background expectation in the VRs is examined to determine the transfer factor. This same method is used to determine the transfer factor and estimate the BGs in the SRs.

4.5.1 QCD multi-jets estimation

One portion of this analysis that I put substantial work into personally was investigating the QCD multi-jet background contribution for the 0-Lepton regions. For this reason a more detailed description of that analysis is presented here.

QCD multi-jet should be a negligible background after requiring $E_{\mathrm{T}}^{\mathrm{miss}} > 200$ GeV in 0-lepton regions based on the past studies looking at a similar phase space as seen in the strong 0L [71], sbottom $b\bar{b} + E_{\mathrm{T}}^{\mathrm{miss}}$, stop 0L [72, 73] analyses to name a few. It is less studied, but the QCD multi-jet contribution in the 1-lepton (1-photon) pre-selection regions is also negligibly low due to the $p_{\mathrm{T}}(\ell) > 30$ GeV, $p_{\mathrm{T}}(W) > 200$ GeV, $E_{\mathrm{T}}^{\mathrm{miss}} > 50$ GeV selection ($p_{\mathrm{T}}(\gamma) > 200$ GeV selection). Moreover, even if there is any, because the QCD multi-jet is still part of the "non-resonant BG", the contribution should be taken into account by the non-resonant BG estimation at the first order. However, the transfer factor can be still subtly different between the QCD multi-jet and the other main backgrounds (e.g. vs V+jets) due to the jet composition (e.g. gluon-initiated vs quark-initiated), so it is still worthwhile to confirm the absence using data-driven methods.

The goal of this sub-section is to provide a quick estimation of the QCD fraction using a set of approximations. The estimation is done differently in the 0-lepton vs 1-lepton and 1-photon region. For the 1-lepton and 1-photon regions a fake factor method is used, this section does not go into further detail regarding these regions. A fake factor method would not work in the 0-lepton region so I used an ABCD analysis to estimate the QCD background contribution.

The studies in this sub-section are subject to a few caveats:

- Since it needs looser kinematic phase space as well as "anti-ID" leptons/photons, the studies had to be based on a different set of ntuples from those used in other portions of the analysis. The major difference is in the AnalysisBase release, track b-tagging config, and the jet cleaning. These changes result in 10 % yield difference in the pre-selection and the CRs/VRs, which does not affect the big picture of the study or the conclusion.
- The normalization of the subtracted non-QCD backgrounds is determined in different methods than the main analysis. This is mainly for sake of simplicity, the impact on the results is minor.

4.5.1.1 0-lepton regions

The QCD multi-jet events in the 0-lepton (and 0-photon) regions surviving the pre-selection typically have mismeasured jets creating large "fake $E_{\mathrm{T}}^{\mathrm{miss}}$". When $E_{\mathrm{T}}^{\mathrm{miss}}$is decently large, the $\min\Delta\phi(j, E_{\mathrm{T}}^{\mathrm{miss}})$ distribution of the QCD multi-jets is known to have a very steep falling shape, which makes $\min\Delta\phi(j, E_{\mathrm{T}}^{\mathrm{miss}}) > 1.0$

an extremely strong QCD rejection cut in the 0-lepton pre-selected regions, CRs, and the SRs. The QCD multi-jet events in those regions are thus supposed to be miniscule. The goal of this section is to set an upper limit on the QCD multi-jet yields in a CR like benchmark region defined as the "region-D" in Table 4.4. The results with different $E_{\mathrm{T}}^{\mathrm{miss}}$threshold are also shown.

After investigating several sets of variables $\min \Delta\phi(j, E_{\mathrm{T}}^{\mathrm{miss}})$ and the presence of a large-R jet passing the $V \to qq$ tagging were selected as the best candidates for variables to define the ABCD regions. Namely whether $\min \Delta\phi(j, E_{\mathrm{T}}^{\mathrm{miss}})$ is less than or greater than 1.0 and whether or not there is 1 large-R get that passes the tagging. An ABCD method is used exploiting the invariant nature of $\min \Delta\phi(j, E_{\mathrm{T}}^{\mathrm{miss}})$ shape between the QCD multi-jet events with and without a large-R jet passing the $V \to qq$ tagging, as demonstrated in Figure 4.6. The proof of principle studies including the closure test were done using the QCD multi-jet MC, and a reasonable closure with these variables are found verifying that the ABCD method can be used.

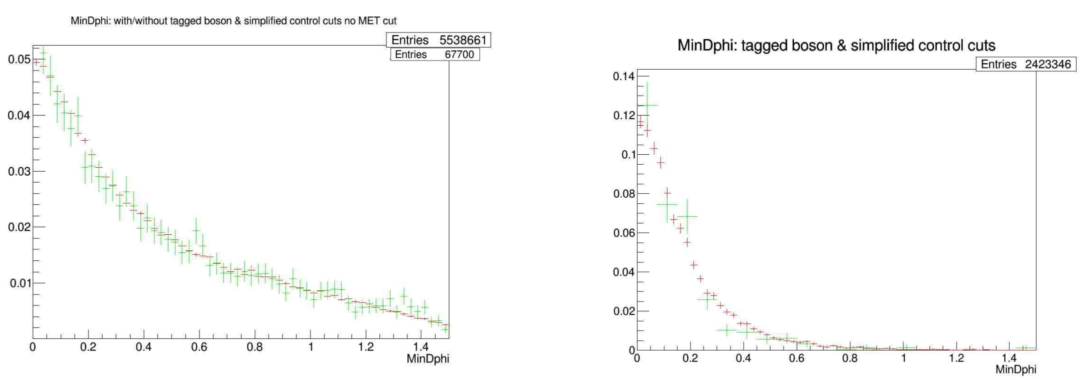

Figure 4.6: $\min \Delta\phi(j, E_{\mathrm{T}}^{\mathrm{miss}})$ distribution of QCD multi-jet MC for events with (green) and without (red) a large-R jet passing the $V \to qq$ tagging. 0-lepton, $n_{\mathrm{Large-}R\ \mathrm{jets}} \geq 2$, $m_{\mathrm{eff}} > 1$ TeV, $n_{b-\mathrm{jet\ (inside\ J)}}^{\mathrm{trk}} \leq 1$ are applied for both plots. $E_{\mathrm{T}}^{\mathrm{miss}}$>100 GeV is additionally applied for the right plot. The areas for all the histograms are normalized to unity.

Table 4.4 summarizes the definition of the ABCD regions used. Single-jet triggers are used to allow testing the regions with low $E_{\mathrm{T}}^{\mathrm{miss}}$thresholds. The $\sigma(E_{\mathrm{T}}^{\mathrm{miss}}) < 10$ cut is to minimize the contamination by the backgrounds other than QCD multi-jet which contribution are subtracted eventually using the MC, with minimally affecting the QCD multi-jet background as this background is characterized by fake $E_{\mathrm{T}}^{\mathrm{miss}}$. This cut is not used in the main analysis, it is only used here to better isolate and predict the QCD multi-jet background.

Object selection				
n_{lepton}	$= 0$			
$n_{\mathrm{Large-}R\ \mathrm{jets}}$	≥ 2			
$n^{\mathrm{trk}}_{b-\mathrm{jet\ (inside\ J)}}$	≤ 1			
Kinematic selection				
$E_{\mathrm{T}}^{\mathrm{miss}}$ [GeV]	$> 100, > 125, > 150, > 175, > 200, > 250, > 300$			
m_{eff} [GeV]	> 1000			
$\sigma(E_{\mathrm{T}}^{\mathrm{miss}})$	< 10			
"ABCD" variables				
	Region-A	Region-B	Region-C	Region-D (target)
$n(V_{qq})$	$= 0$	$= 0$	$= 1$	$= 1$
$n(!V_{qq})$	$= 2$	$= 2$	$= 1$	$= 1$
$\min \Delta\phi(j, E_{\mathrm{T}}^{\mathrm{miss}})$	< 1.0	> 1.0	< 1.0	> 1.0

Table 4.4: Definition of the benchmark region in which the upper limit is calculated (region-D) and the auxiliary regions used for the ABCD method. $n(V_{qq})$ ($n(!V_{qq})$) denote the number of large-R jet passing (failing) the $W/Z \to qq$ tagging. Various $E_{\mathrm{T}}^{\mathrm{miss}}$thresholds are considered. Note that the $E_{\mathrm{T}}^{\mathrm{miss}}$cut in the SRs are $E_{\mathrm{T}}^{\mathrm{miss}} > 300$ GeV in the 4Q and $E_{\mathrm{T}}^{\mathrm{miss}} > 200$ GeV in the 2B2Q category.

Figure 4.7 shows the $\min \Delta\phi(j, E_{\mathrm{T}}^{\mathrm{miss}})$ distributions in the A+B and C+D region with the individual region separated at $\min \Delta\phi(j, E_{\mathrm{T}}^{\mathrm{miss}}) = 1.0$ with various $E_{\mathrm{T}}^{\mathrm{miss}}$thresholds.

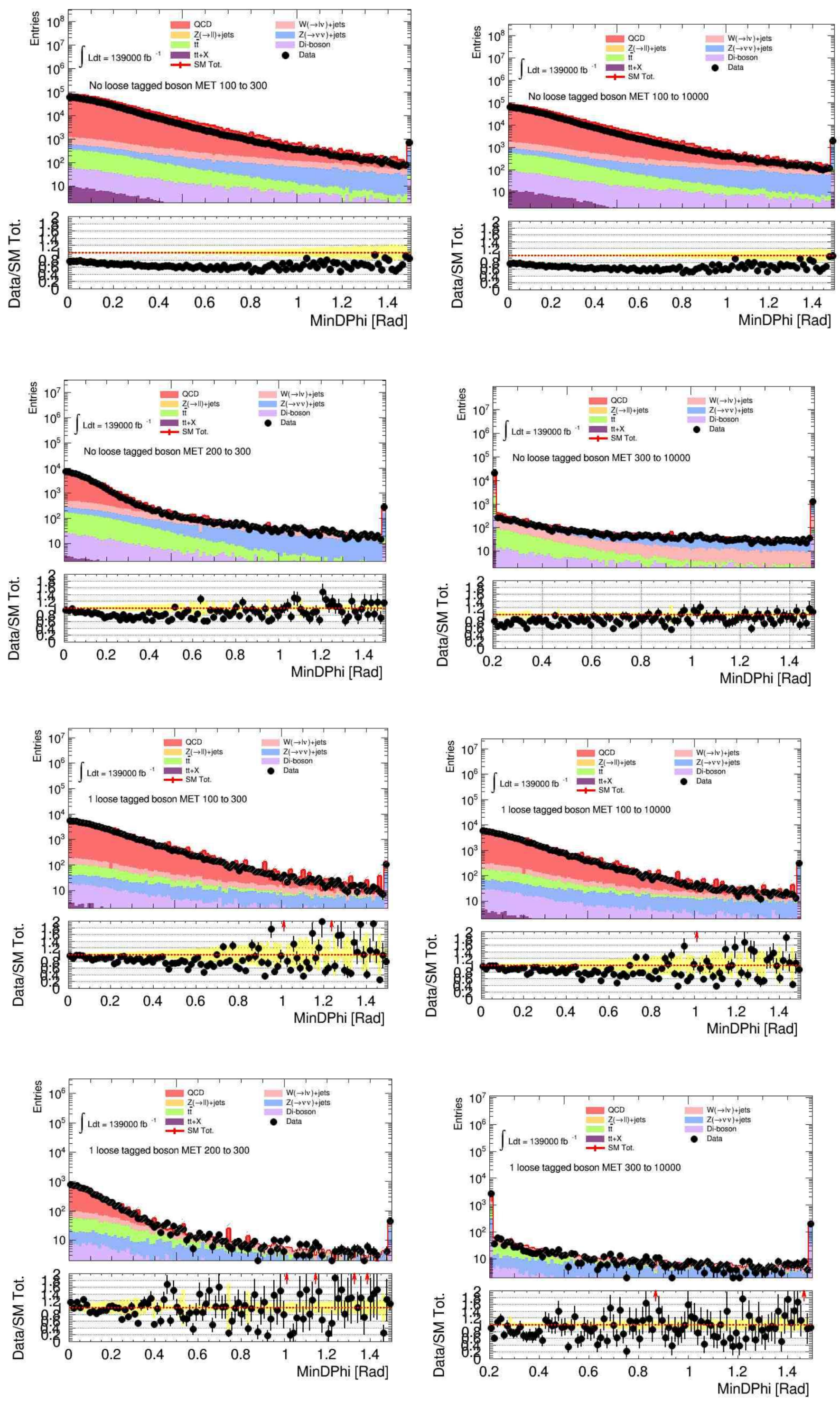

Figure 4.7: $\min \Delta\phi(j, E_{\mathrm{T}}^{\mathrm{miss}})$ distribution of the data and the MC BGs in the A+B region (top) and the C+D region (bottom) (separated at $\min \Delta\phi(j, E_{\mathrm{T}}^{\mathrm{miss}}) = 1.0$) with various $E_{\mathrm{T}}^{\mathrm{miss}}$thresholds. The QCD multi-jet MC is also overlaid as the reference.

The QCD multi-jet yields in Region-D are derived using the ABCD application, with all non-QCD background contribution subtracted using the MC. The results are summarized in Table 4.5 together with the raw data yields in Region-D and those with the MC subtraction. Table 4.6 shows the same estimation in the Region-D with the 2B2Q pre-selection applied. In all cases, the QCD multi-jet contribution in Region-D ($E_{\mathrm{T}}^{\mathrm{miss}} > 300$ GeV) is confirmed to be negligible.

$E_{\mathrm{T}}^{\mathrm{miss}}$	Reg-B (data)	Reg-C (data)	Reg-D (ABCD estimate)	Reg-D (data)
> 100	2322 ± 61	32800 ± 193	202 ± 5	968 ± 31
> 150	45 ± 24.6	9480 ± 114	4.5 ± 2.5	685 ± 26
> 200	-14.8 ± 16.5	3864 ± 82	-1.6 ± 1.8	587 ± 24
> 250	-7.05 ± 12.7	1605 ± 59	-0.78 ± 1.4	491 ± 22
> 300	-9.62 ± 9.73	579.8 ± 39	-0.95 ± 0.96	413 ± 20

Table 4.5: Results of the ABCD estimation of Region-D together with the raw data yields in Region-B/C/D.

$E_{\mathrm{T}}^{\mathrm{miss}}$	Reg-B (data)	Reg-C (data)	Reg-D (ABCD estimate)	Reg-D (data)
> 100	211 ± 18	5063 ± 75	21.8 ± 1.81	68 ± 8.3
> 150	23.6 ± 7.6	2165 ± 52.0	2.97 ± 0.96	45 ± 6.7
> 200	6.4 ± 4.6	988 ± 37.5	0.878 ± 0.63	38 ± 6.2
> 250	5.8 ± 3.7	425 ± 26.6	0.799 ± 0.51	33 ± 5.8
> 300	3.0 ± 2.7	165 ± 17.5	0.408 ± 0.37	27 ± 5.2

Table 4.6: Results of the ABCD estimation of Region-D with the 2B2Q pre-selection applied, together with the raw data yields in Region-B/C/D.

4.6 Results

To determine final background estimates a profile log-likelihood fit is performed simultaneously in all CRs and VRs for a given interpretation. Systematic uncertainties are treated as Gaussian distributed nuisance parameters, while statistical uncertainties of the MC samples are treated as Poisson distributed nuisance parameters. At this point three types of fit configurations are used to derive the results. These include a background-only fit, discovery fit, and exclusion fit.

The background-only fit is performed only considering the CRs and assuming no contribution from signal. The normalization of the total reducible backgrounds is allowed to float and constrained by the fit using data in the CRs. Normalization factors and nuisance parameters are adjusted by maximizing likelihood. Independent fits are performed for the 0L, 1L, and 1Y categories and for the 4Q and 2B2Q region within each category.

In the discovery fit the hypothesis test for a generic BSM (Beyond the SM) signal. This sets upper limits on the number of events and visible cross-section for the signal. Any contribution from signal is allowed only in the SR. The fit uses a single SR and the associated CR0L bins following the same background constraints as in the background-only fit.

The exclusion fit sets the exclusion limit for a given signal model. The SRs and corresponding CRs are fit simultaneously to determine BG normalization factors and systematic constraints. The 95% confidence level(CL) exclusion limit is defined by the $CL_s < 0.05$.

In this study no significant excesses were found. See figure 4.8 for a summary of the observed data. 95% CL exclusion limits are set from the exclusion fits.

4.6.1 $(\widetilde{W}, \widetilde{B})$ simplified model exclusion limits

Results are also found for simplified models of wino production which decay into a bino LSP. These results can be directly compared to search sensitivities from previous ATLAS analyses. For chargino pair production where each decays into a W-boson and an LSP, a chargino mass between 630 and 760 GeV is excluded for m($\tilde{\chi}_{light}$) < 80 GeV. For chargino-neutralino production which decay to two LSPs and a WZ or Wh, wino masses between 440 and 960 GeV with an LSP mass below 300 GeV and between 400 and 1060 GeV is excluded for an LSP mass less than 420 GeV respectively. This significantly extends the exclusion limits

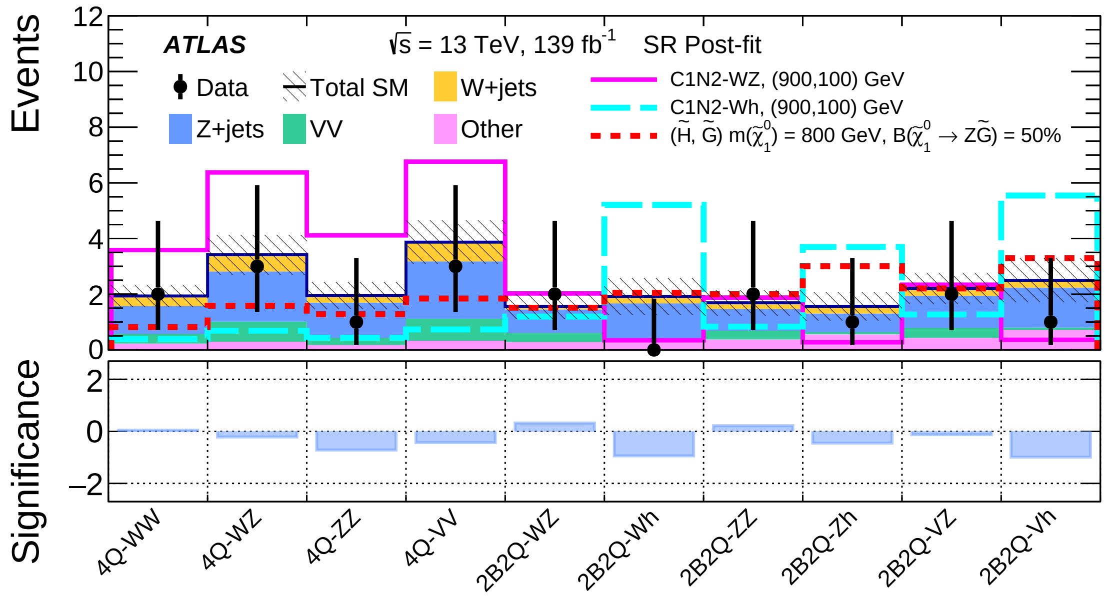

Figure 4.8: Summary of observed data and predicted SM background for all Signal Regions. The bottom panel shows the significance of the difference seen between observed events and predicted SM expectations.

set by previous searches.

4.6.2 $(\widetilde{H}, \widetilde{G})$ model exclusion limits

For the GGM model with a Gravitino LSP exclusion limits are set for various branching ratios. For $\mathcal{B}(\tilde{\chi}_1^0 \to Z\tilde{G})$ = 100% and 50% m($\tilde{\chi}_{light}$) from 450 to 940 GeV and 500 to 850 GeV are excluded respectively. This is seen in figure 4.10.

4.6.3 $(\widetilde{H}, \tilde{a})$ model exclusion limits

Finally for the axino LSP, similarly to the GGM model, exclusion limits are set for various branching ratios. For $\mathcal{B}(\tilde{\chi}_1^0 \to Z\tilde{a}) = 100\%$ a m($\tilde{\chi}_{light}$) results are seen in figure 4.11 where from 450 to 940 GeV is excluded for an axino mass less than 300 GeV. Sensitivity decreases with branching ratio in this model so for $\mathcal{B}(\tilde{\chi}_1^0 \to Z\tilde{a})$ = 50% a $m(\tilde{\chi}_{light})$ between 500 and 850 GeV is excluded for axino mass less than 210 GeV.

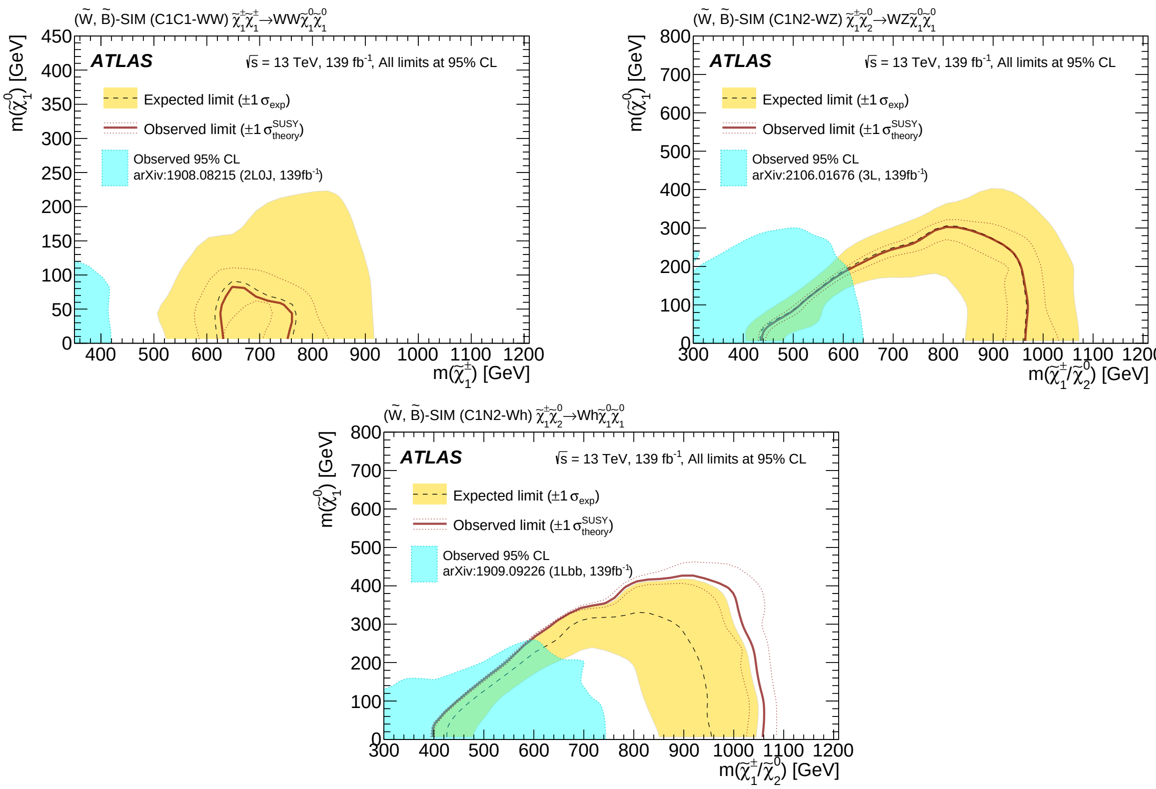

Figure 4.9: Exclusion limits for the $(\widetilde{W}, \widetilde{B})$ simplified model as a function of the produced wino mass $(m(\widetilde{\chi}_1^{\pm}/\widetilde{\chi}_2^0))$ and the bino LSP mass $(m(\widetilde{\chi}_1^0))$. Expected 95% CL exclusion limits are seen in dashed black lines with the observed limits in solid red for C1C1-WW (top-left), C1N2-WZ (top-right), and C1N2-Wh (bottom). Limits set by previous ATLAS searches on C1C1-WW [12], C1N2-WZ [14, 74], and C1N2-Wh [21] are shown by the light blue contours. Only the strongest mass limits from previous searches are shown.

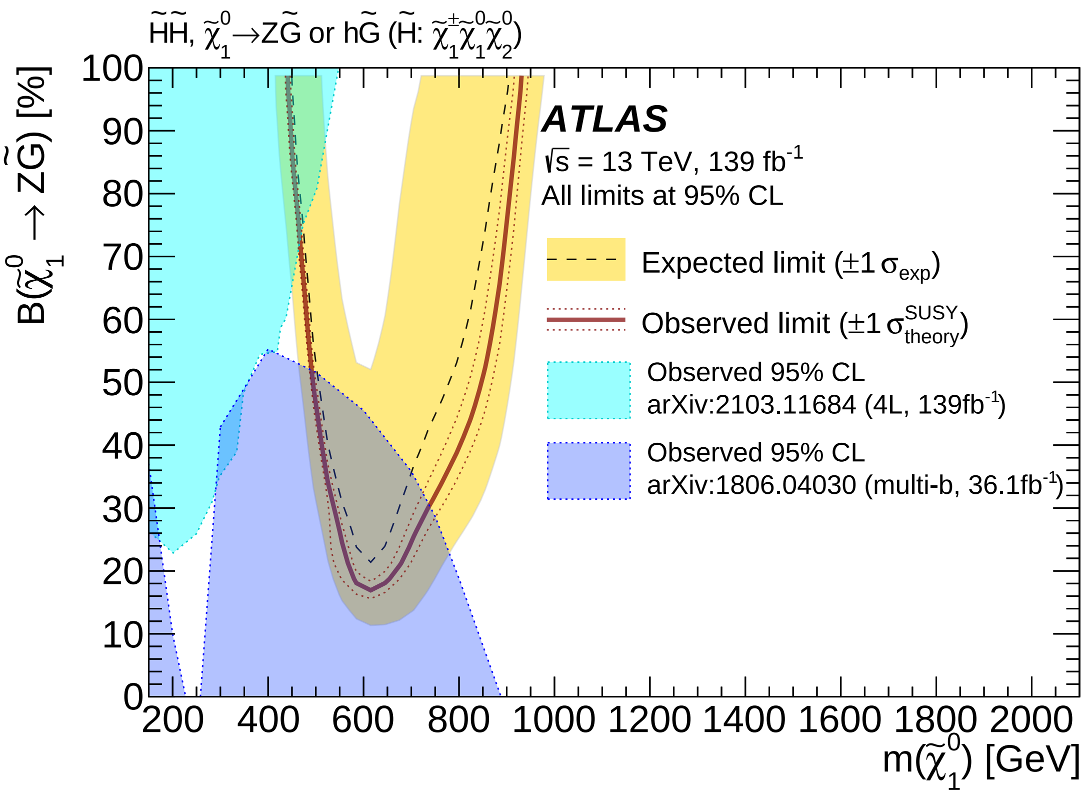

Figure 4.10: Expected and observed 95% CL exlusion limits represented by dashed and solid red lines respectively. This is as a function of lightest higgsino mass and $\mathcal{B}(\tilde{\chi}_1^0 \to Z\tilde{G})$.

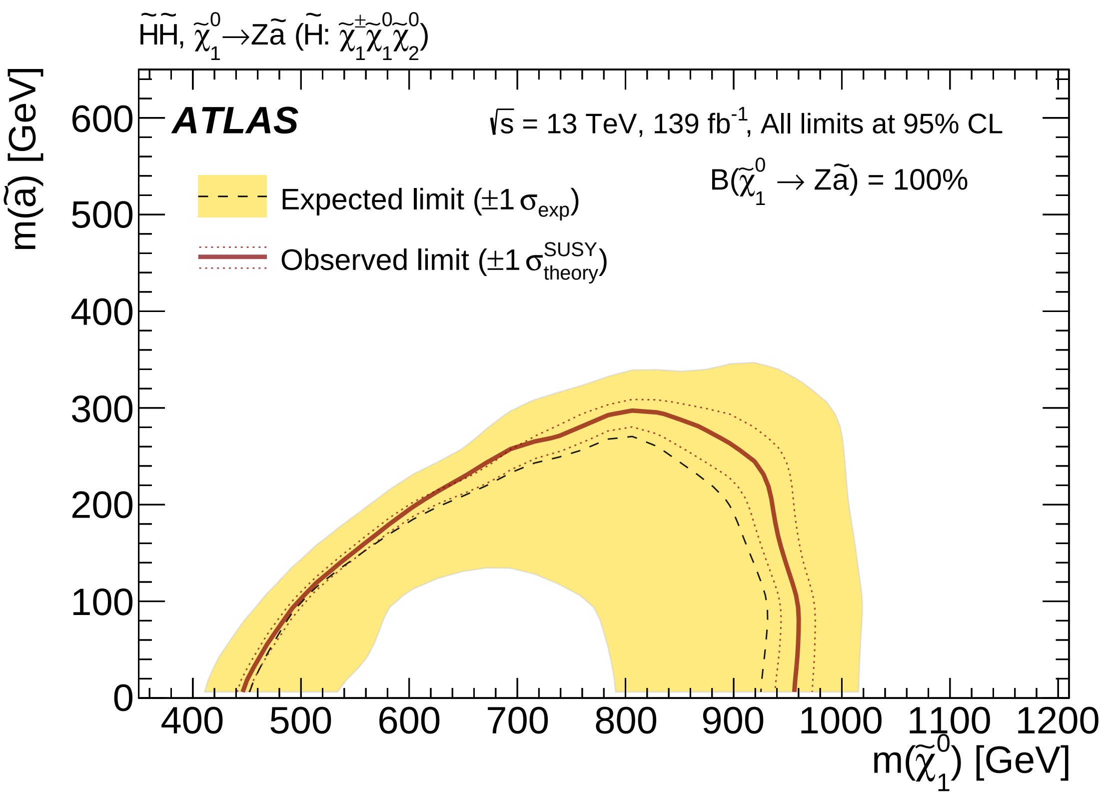

Figure 4.11: Expected and observed 95% CL exlusion limits represented by dashed and solid red lines respectively for the axino model. This is for $\mathcal{B}(\tilde{\chi}_1^0 \rightarrow Z\tilde{a}) = 100\%$ as a function of lightest higgsino mass and axino mass.

CHAPTER 5

EXTRAPOLATION OF ALL-HADRONIC SUSY SEARCH TO HL-LHC CONDITIONS

This chapter describes an upgrade study of the analysis discussed in Chapter 4. The purpose is to extend the Fully-Hadronic SUSY Electroweak analysis to anticipated HL-LHC conditions by simulating the primary differences in order to project possible sensitivites and motivate conducting the analysis once sufficient data has been taken. The primary changes made in this analysis are scaling the backgrounds and signal for the change in cross section expected from going from a center-of-mass energy of 13 TeV during Run 2 to the expected 14 TeV center-of-mass energy and, more importantly, increasing the integrated luminosity from 139 fb^{-1} to an anticipated 3 ab^{-1} (3000 fb^{-1}) of proton-proton collision data. This study focuses on the simplified models of wino pair production, where each decays into a bino LSP (($\widetilde{W}, \widetilde{B}$)-SIM). This upgrade was also able to include signal regions in the 4B Category.

This chapter begins with a motivation of this upgrade study as well as highlighting some of the ways in which it differs from the Run 2 study. Then a review of the physics models and discussion of relevant Phase 2 upgrades to the ATLAS detector and how they may impact this study is included. It is important to note that this study is conducted on entirely MC simulation. A summary of the object defintions used in this study is given, which is a subset of the objects utilized in the Run 2 analysis. Then the signal region selection procedure is detailed as well as highlighting the optimization procedures. Next the statistical analysis used and results from the study are detailed including how the projected limits compared to those presented in Chapter 4. Finally there is a brief summary of the analysis and possible future work further extending this upgrade to other signal models studied in the fully-hadronic electroweak SUSY analysis.

5.1 Interdouction and Motivation

The most relevant superpartners in the Minimal Supersymmetric Standard Model (MSSM) for this analysis are the Wino ($\tilde{W}$), Bino ($\tilde{B}$), and Higgsino ($\tilde{H}$). These are the superpartners of the SU(2), U$(1)_Y$, and the Higgs field respectively. Through mixing, the charginos, $\tilde{\chi}_i^{\pm}$ i=(0,1), and neutralino, $\tilde{\chi}_j^0$ j=(0,1,2,3), mass eigenstates are formed, where the subscript indicates increasing mass. These are collectively referred to as electroweakinos. The lightest neutralino is often assumed to be the lightest supersymmetric particle (LSP) [75, 76]. In other signal models this analysis considers the Gravitino ($\tilde{G}$) to be the LSP candidate. The LSP is a strong candidate for a weakly interacting massive dark matter particle.

This analysis targets the production of heavy electroweakinos $\widetilde{\chi}_{\text{heavy}}$ which then decay to a light elecroweakino and an on-shell W, Z, or h boson. The mass splitting, $\Delta m(\widetilde{\chi}_{\text{heavy}}, \widetilde{\chi}_{\text{light}})$, is assumed to be large, at least 400 GeV. The $\widetilde{\chi}_{\text{light}}$ can be a neutralino, LSP, or a chargino that is nearly degenerate with the neutralino. If $\widetilde{\chi}_{\text{light}}$ is a chargino, it would then decay into the LSP along with soft particles that are not reconstructed or targeted in this search.

The focus of this analysis is on fully hadronic decay modes of the W, Z, and h bosons to take advantage of larger branching ratios of all three bosons to hadronic rather than leptonic final states, providing sensitivity to heavier electroweakinos. These decays can be $W \to q\bar{q}$, $Z \to q\bar{q}/b\bar{b}$, or $h \to b\bar{b}$ as illustrated in Figure 5.1. In the Run 2 analysis described in chapter 4, that this upgrade study is based on, two final states were considered: $qqqq$ where W or Z bosons decay to two light-flavor quarks and $qqbb$ where a W or Z boson decays to two light-flavor quarks and a Z or h boson decays to a b-quark and anti-b-quark. This extrapolation also considers the boosted $bbbb$ final state, which was covered in a separate analysis during Run 2 [77] as a resolved final state, where Z or h bosons decay to $b\bar{b}$. ATLAS and CMS searches have also

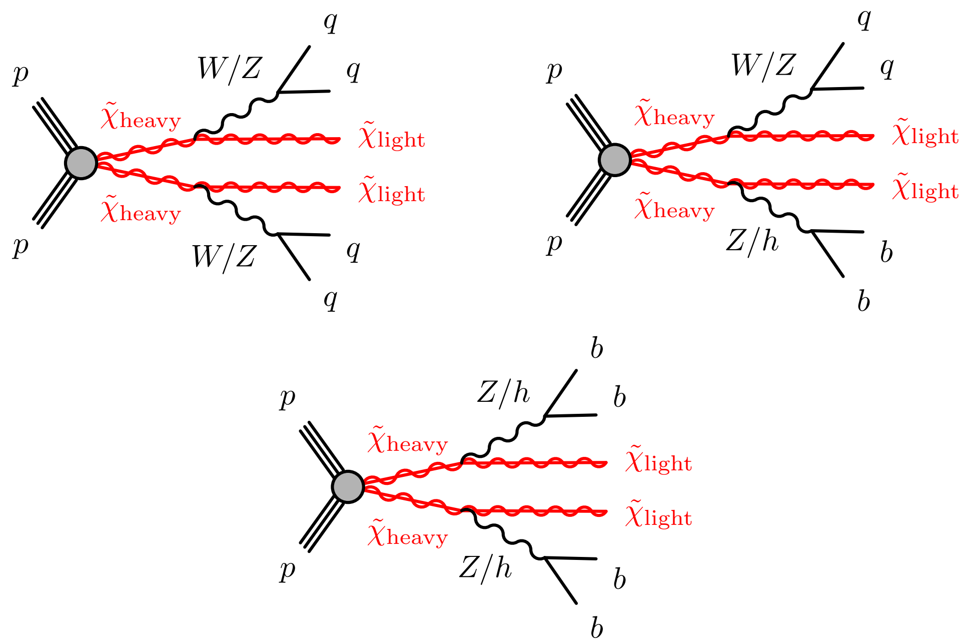

Figure 5.1: Diagrams of targeted models and final state/signatures are depicted. The final states represented in the top row are used for the $(\widetilde{W},\widetilde{B})$ model and all three final states are used for the $(\widetilde{H},\widetilde{G})$ model discussed in Section 5.3. In these diagrams, $\tilde{\chi}_{\text{heavy}}$ represents the wino doublet and higgsino triplet respectively and $\tilde{\chi}_{\text{light}}$ represents the bino and gravitino.

searched for electroweakino pair production that decay leptonically [12–24, 30, 31, 78] extensively.

The high luminosity upgrade to the LHC (HL-LHC) expects to have proton-proton collisions at a center of mass energy of 14 TeV and reach an integrated luminosity of approximately 3 ab^{-1}. The large data set projected for the end of the HL-LHC will provide great potential for the discovery of heavy SUSY particles. This analysis addresses the ATLAS sensitivity to the direct production of charginos and neutralinos that decay to a fully hadronic final state associated with the LSPs. The Run 2 search utilizing fully hadronic final states showed a significant improvement on sensitivity at high mass regions compared to leptonic modes. Conducting a similar search on HL-LHC data is expected to give an improved sensitivity as well; this note is intended to give insight into the potential reach. Several extrapolations to HL-LHC conditions for other searches have already been conducted, including the projection of the fully hadronic search from CMS [79].

The analysis presented here is conducted using Run 2 13 TeV Monte Carlo (MC) simulation following a similar strategy to the Run 2 search. The search is projected for the center of mass energy and integrated luminosity in the HL-LHC, assuming the same object reconstruction performance as Run 2, taking into account both the harsher pileup environment and the expected improved reconstruction techniques. Very similar methods and techniques are used compared to the previous search including use of jet substructure to utilize boosted boson tagging. Background rejection cuts are reoptimized for this analysis compared to the Run 2 search.

There are many changes going forward to HL-LHC conditions including higher center-of-mass energy, new detector geometries, much higher pileup, and a substantially higher integrated luminosity. This projection has taken into account the projected HL-LHC conditions by doing an overall reweighting by a constant factor based on the cross-section ratios for both signal and background simulations. The current detector geometry and pileup are used and this analysis assumes that after the upgrade the new detector and analysis methods will be able to handle the increased pileup, reaching the same efficiency.

5.2 Changes to the Atlas Detector

During Run 2 the ATLAS experiment collected 140 fb^{-1} of proton-proton collisions with a center-of-mass energy of 13 TeV and an average pileup, interactions per bunch crossing, of $\langle\mu\rangle = 34$. The detector will undergo a major upgrade in preparation for the HL-LHC, referred to as the Phase-2 upgrade. This upgrade will allow ATLAS to maintain efficient data taking and event reconstruction in new run conditions including an increase in instantaneous luminosity as well as a dramatic increase in pileup to $\langle\mu\rangle = 200$ with a center-of-mass energy of 14 TeV. A detailed overview of the individual upgrades is given in Refs [80–87].

The most relevant improvements for this analysis are the upgrade from the current Inner Detector (ID) to the new Inner Tracker (ITk) as well as the upgrade to the missing transverse energy ($E_{\text{T}}^{\text{miss}}$) trigger. The current ID covers the region up to $|\eta| < 2.5$ while the ITk will cover up to $|\eta| < 2.7$ with a strip detector and up to $|\eta| < 4$ with a pixel detector. This extension will significantly improve the range of precise tracking within ATLAS and will, for example, improve the current b-tagger which will use the full pixel coverage. The ITk will allow for improvements in b-tagging both within the $|\eta| < 2.5$ range as well as extend that to $|\eta| < 4$ illustrated in Ref. [88]. The b-tagging algorithm is vital to this analysis so this change will directly impact any similar search conducted using data taken during the HL-LHC. It is important to note that these improvements will impact HL-LHC searches but are not included in this analysis.

The current on-line trigger system will be replaced by a new trigger capable of handling the increased rate associated with taking data from the HL-LHC. According to current projections, the new trigger will allow for the maintenance or even lowering of current thresholds, avoiding any loss of performance even with the increased rate. The Run 2 search used a $E_{\mathrm{T}}^{\mathrm{miss}}$trigger so the new $E_{\mathrm{T}}^{\mathrm{miss}}$trigger plateau [85] will be relevant to any search conducted using HL-LHC data following this extrapolation. Within this extrapolation the same efficiency plateau as in the Run 2 analysis (approximately 200 GeV) can be safely assumed for this extrapolation.

The analysis presented here uses full Run 2 conditions including current ATLAS geometry and efficiencies. The simulated data and backgrounds used are described in Section 5.4 and are based on the Run 2 detector conditions and reconstruction.

5.3 Target Physics Models

All physics models in this analysis are labeled in the form ($\widetilde{\chi}_{\mathrm{heavy}}$,$\widetilde{\chi}_{\mathrm{light}}$) and other SUSY particles are assumed to be decoupled in mass. This analysis focuses on only boosted states with a mass splitting of $\Delta m(\widetilde{\chi}_{\mathrm{heavy}}, \widetilde{\chi}_{\mathrm{light}}) > 400$ GeV. Wino-like states form a doublet and higgsino-like states form a triplet creating a mass degeneracy. The mass splittings of these multiplets are typically on the order 10 GeV or less. Because of the large difference between the mass splittings of $\widetilde{\chi}_{\mathrm{heavy}}$ and $\widetilde{\chi}_{\mathrm{light}}$ compared to those within the multiplets, the particles generated from decays within the multiplets are not reconstructed in this analysis and SUSY states within each multiplet are treated as degenerate.

There are two models considered in this upgrade study, $(\widetilde{W}, \widetilde{B})$ and ($\widetilde{H}$,$\widetilde{G}$). In this note only three simplified models of the first are considered, the overall caregory is denoted as $(\widetilde{W}, \widetilde{B})$ simplified models or $(\widetilde{W}, \widetilde{B})$-SIM and is broken up into: C1C1-WW, C1N2-WZ, and C1N2-Wh. The first simplified model is charged wino pair production ($\tilde{\chi}_1^{\pm}\tilde{\chi}_1^{\mp}$) while the second and third are charged and neutral wino production ($\tilde{\chi}_1^{\pm}\tilde{\chi}_2^{0}$). All three of these models were included in the Run 2 analysis [89]. The production modes, final states, Signal Regions (SRs) included, and branching ratio assumptions of each model are shown in Table 5.1. The branching ratio assumptions for the three simplified models are:

C1C1-WW: $\tilde{\chi}_1^{\pm}\tilde{\chi}_1^{\pm} \to WW\ \tilde{\chi}_1^0\tilde{\chi}_1^0 \quad (\mathcal{B}(\tilde{\chi}_1^{\pm} \to W\tilde{\chi}_1^0) = 100\%)$

C1N2-WZ: $\tilde{\chi}_1^{\pm}\tilde{\chi}_2^0 \to WZ\ \tilde{\chi}_1^0\tilde{\chi}_1^0 \quad (\mathcal{B}(\tilde{\chi}_1^{\pm} \to W\tilde{\chi}_1^0) = \mathcal{B}(\tilde{\chi}_2^0 \to Z\tilde{\chi}_1^0) = 100\%)$

C1N2-Wh: $\tilde{\chi}_1^{\pm}\tilde{\chi}_2^0 \to Wh\ \tilde{\chi}_1^0\tilde{\chi}_1^0 \quad (\mathcal{B}(\tilde{\chi}_1^{\pm} \to W\tilde{\chi}_1^0) = \mathcal{B}(\tilde{\chi}_2^0 \to h\tilde{\chi}_1^0) = 100\%)$,

The second model, $(\tilde{H},\tilde{G})$, is inspired by General Gauge Mediation (GGM), which features a nearly massless gravitino ($\tilde{G}$) as the primary LSP candidate. In this model a member of a higgsino triplet is produced and decays into a gravitino LSP plus a Z- or h-boson. All four production modes are considered: $\tilde{\chi}_1^{\pm}\tilde{\chi}_1^{\mp}$, $\tilde{\chi}_1^{\pm}\tilde{\chi}_2^0$, $\tilde{\chi}_1^{\pm}\tilde{\chi}_1^0$, $\tilde{\chi}_1^0\tilde{\chi}_2^0$. In these scenarios the heavy higgsinos are $\tilde{\chi}_1^{\pm}$ and $\tilde{\chi}_2^0$. A small higgsino-gravitino coupling is considered where the heavy higgsinos always decay into a gravitino via the lightest higgsino $\tilde{\chi}_1^0$, this signature is illustrated in Figure 5.2. The $\tilde{\chi}_1^0$ is considered to have a short enough lifetime to be considered a prompt decay. In this model the light higgsino decays into the LSP and either a Z or h boson. The branching ratio between the Z decay and h decay is treated as a free parameter and scanned in the limit setting. A more in depth discussion of this is found in Section 4.6.

Model	**Production**	**Final states**	**SRs simultaneously fitted**	**Branching ratio**
$(\tilde{H},\tilde{G})$	$\tilde{\chi}_1^{\pm}\tilde{\chi}_1^{\mp}$, $\tilde{\chi}_1^{\pm}\tilde{\chi}_1^0$, $\tilde{\chi}_1^{\pm}\tilde{\chi}_2^0$, $\tilde{\chi}_1^0\tilde{\chi}_2^0$	ZZ, Zh, hh	4QZZ, 2B2QZZ, 2B2QZh, 4Bhh	$\mathcal{B}(\tilde{\chi}_1^0 \to h\tilde{G})$ scanned.
$(\tilde{W},\tilde{B})$ **simplified models:**	$(\tilde{W},\tilde{B})$**-SIM**			
C1C1-WW	$\tilde{\chi}_1^{\pm}\tilde{\chi}_1^{\mp}$	WW	4QWW	$\mathcal{B}(\tilde{\chi}_1^{\pm} \to W\tilde{\chi}_1^0) = 1.$
C1N2-WZ	$\tilde{\chi}_1^{\pm}\tilde{\chi}_2^0$	WZ	4QWZ, 2B2QWZ	$\mathcal{B}(\tilde{\chi}_1^{\pm} \to W\tilde{\chi}_1^0) = \mathcal{B}(\tilde{\chi}_2^0 \to Z\tilde{\chi}_1^0) = 1.$
C1N2-Wh	$\tilde{\chi}_1^{\pm}\tilde{\chi}_2^0$	Wh	2B2QWh	$\mathcal{B}(\tilde{\chi}_1^{\pm} \to W\tilde{\chi}_1^0) = \mathcal{B}(\tilde{\chi}_2^0 \to h\tilde{\chi}_1^0) = 1.$

Table 5.1: Summary of the production modes, final states, signal regions (SRs), and the branching ratio assumptions for the signal models targeted in the search.

5.4 Monte Carlo Simulations

MC simulations were used to estimate the relevant SM backgrounds and signal yields in the analysis regions. The same background MC samples that were generated for the Run 2 paper were used here [89]. The

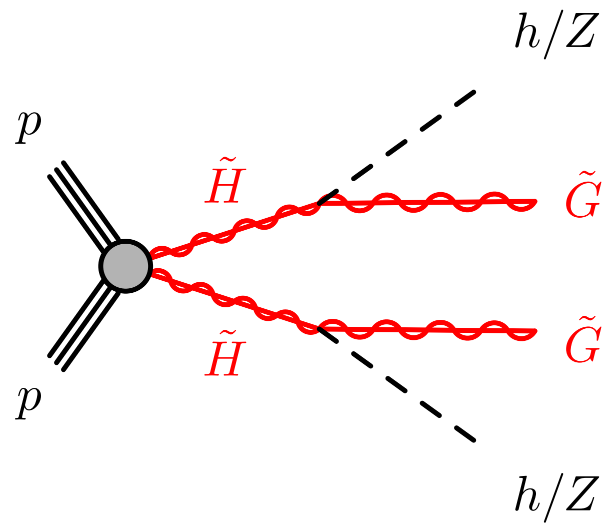

Figure 5.2: Diagram of N2N1 production for the gravitino model where higgsino triplets are represented by $\tilde{H}$.

simulated backgrounds include $Z \rightarrow \nu\nu$, $W+$jets, $t\bar{t}$, $t+X$, $t\bar{t}+X$ (which includes all $t\bar{t}$ events with any additional heavy particles), di-boson (including WW, ZZ, and WZ which are denoted as VV), and tri-boson (which is denoted VVV). All backgrounds are generated at $\sqrt{s} = 13$ TeV and scaled to $\sqrt{s} = 14$ TeV and normalized by a reweighting using a ratio of $\sqrt{s} = 13$ TeV and $\sqrt{s} = 14$ TeV cross-sections.

Three sets of simplified model samples are generated to cover the final states considered in this extrapolation. The signal samples used for designing the Run 2 analysis were reused in this study and additional samples for electroweakino masses up to 1500 GeV were produced for this study using identical methods and generators as were employed in the Run 2 paper. For some mass points outside of the original signal grid, which became necessary in the analysis, the yields were estimated using a ratio of the cross sections between a generated point and the target point assuming invariant acceptance. The simulated signal is given an overall reweighting to $\sqrt{s} = 14$ TeV using a constant factor based on the cross-section ratio, this time from the LHC SUSY cross-sections.

For the Gravitino model, $(\widetilde{H}, \widetilde{G})$, a set of dedicated samples was generated with all production modes included ($\widetilde{\chi}_1^{\pm}\widetilde{\chi}_1^{\mp}$, $\widetilde{\chi}_1^{\pm}\widetilde{\chi}_1^{0}$, $\widetilde{\chi}_1^{\pm}\widetilde{\chi}_2^{0}$, $\widetilde{\chi}_1^{0}\widetilde{\chi}_2^{0}$). The production considers a variable $\mathcal{B}(\widetilde{\chi}_1^0 \rightarrow Z\tilde{G}) = 1 - \mathcal{B}(\widetilde{\chi}_1^0 \rightarrow h\tilde{G})$ in the branching ratio. More details on the specifics of generators used for all of the signal simulations can be found in Chapter 4 or in the Run 2 paper.

5.5 Event Reconstruction and Object Definitions

This section will define the main objects used in this analysis, namely electrons, muons, small-R jets, and large-R jets. One major tool also utilized by the search is boosted boson tagging. The objects used are a subset of those employed in the Run 2 analysis and describedin section 4.3. This employs three additional variables: large-R jet mass, the energy correlation function, and track multiplicity.

Electron candidates are reconstructed from electromagnetic clusters formed by energy deposits in the ECAL consistent with tracks in the inner detector using the super-cluster algorithm. Electrons are required to have $p_{\mathrm{T}} > 7$ GeV and $|\eta| < 2.47$, and meet the *Tight* criteria of the likelihood-based identification [53]. In addition the transverse impact parameter is required to satisfy $|d_0/\sigma(d_0)| < 5$ for electrons in order to reduce non-prompt electrons from heavy hadron decays.

Muons are reconstructed by taking tracks from the inner detector that are consistent with those from the muon spectrometer using the "combined muon algorithm". Muons must have $p_{\mathrm{T}} > 6$ GeV and $|\eta| < 2.7$, and to meet the *Tight* [54] identification criteria defined for muons. Also, the transverse impact parameter is required to satisfy $|d_0/\sigma(d_0)| < 3$ for muons.

Small-R jet candidates are reconstructed from particle-flow objects [55] using the anti-k_t algorithm with a radius parameter of $R = 0.4$. Small-R jets are required to be within $|\eta| < 2.8$ and have $p_{\mathrm{T}} > 30$ GeV. Additionally, those with $p_{\mathrm{T}} < 60$ GeV and $|\eta| < 2.5$ must satisfy the *Tight* quality criteria of the track-based jet vertex tagger [56, 57] in order to suppresses jets originating from pileup. Note that in this analysis small-R jets are only used for $E_{\mathrm{T}}^{\mathrm{miss}}$calculation and in the kinematic variable min $\Delta\phi(E_{\mathrm{T}}^{\mathrm{miss}}, j)$.

Finally, the primary physics objects used in this study are large-radius jets (large-R jets). These are defined with a radius parameter of $R = 1.0$. They are reconstructed from locally calibrated topo-clusters [58] using the anti-k_t algorithm [59] in the FastJet package [60]. To remove contributions from underlying events and pileup a trimming algorithm [61] is applied to mitigate the effects of pileup and soft radiation. The constituents of each jet are reclustered with the k_t algorithm [62] into $R = 0.2$ subjets, these are removed if they carry under 5% of the original jet p_{T}. The jet mass, m_J, is calculated based on the combined mass prescription [63] to have the best mass resolution. This is achieved by taking the weighted sum of masses computed using the calorimeter and tracking information. The $p_{\mathrm{T}}$and mass scales are initially calibrated using simulation, followed by an in situ calibration [64] to correct for residual differences between data and MC simulation. Baseline large-R jets used in the analysis are selected with $p_{\mathrm{T}} > 200$ GeV, $|\eta| < 2.0$, and $m_J > 40$ GeV.

Two types of boosted boson tagging are applied on the preselected large-R jets to identify SM boson decays within each structure. The first is to tag light-flavor quarks, $W_{qq}(Z_{qq})$-tagging targeting $W(Z) \rightarrow qq$. The second focuses on tagging specifically b-quarks, $Z_{bb}(h_{bb})$-tagging targeting $Z(h) \rightarrow bb$. In this note, large-R jets are often referred to in this way, by the boson which is tagged, and whose decay appears to be the origination of the large-R jet, as well as by the quark content of the jet.

The primary variables used in boosted boson tagging are large-R jet mass (m_J), the energy correlation function (D_2), and track multiplicity (n_{trk}). The D_2 variable is defined as the ratio of three-point to two-point energy correlation functions [65, 66]. These variables are also referred to as three- and two- prongness respectively and are based on the energies and pairwise angular separations of particles within a jet. Track multiplicity, n_{trk}, is the number of tracks that, before trimming is applied, are matched to the large-R jet by ghost-association [67]. The selections are optimized separately for targeting W and Z bosons. The cut values applied to m_J and D_2 are the same as for the "50% efficiency W/Z tagger" in Ref. [68]; an n_{trk} cut, loosened from ≤ 26 to ≤ 32 (34) for the $W_{qq}(Z_{qq})$-tagging, is applied in this analysis to achieve the optimum sensitivity and better modeling in MC simulation. In order to maintain orthogonality with $Z_{bb}(h_{bb})$-tagging, the b-jet multiplicity of the large-R jet is required to be less than two.

$E_{\mathrm{T}}^{\mathrm{miss}}$requirements are also heavily used to include any requirements imposed by $E_{\mathrm{T}}^{\mathrm{miss}}$triggers (these are discussed in Section 5.6.1), define particle tagging that is used in the analysis, and provide background rejection cuts. For this analysis light quark jets are tagged as originating from a W or Z boson with a dynamic mass window cut versus $p_{\mathrm{T}}$where the W boson typically has a mass between 65 GeV and 95 GeV while the Z boson is generally from 75 GeV to 105 GeV. In the b-tagged jets however, the Z boson is tagged with a fixed mass window cut with an upper limit of 100 GeV in order to maintain orthogonality with the h boson tagged jets. This requires the jet mass to be in the range $70 \text{ GeV} < m_J < 100 \text{ GeV}$ for the Z_{bb} tagging and for h_{bb} tagging within the range $100 \text{ GeV} < m_J < 135 \text{ GeV}$. In order to improve the mass peak resolution, the jet mass is corrected by adding the momentum of the highest-p_{T}muon identified within the large-R jet. This is shown visually in Figure 5.3. Notably, this shows the overlap between the mass window for the W- and Z bosons in the light quark jets and the orthogonality of Z and h bosons in the b-tagged jets.

A generic large-R jet which contains two light flavor (b-) quarks is referred to as J_{qq} (J_{bb}) and defined by the boson tagging process. A large-R jet that originates from a particle tagged as a W boson and contains two light flavor quarks is referred to as W_{qq}. Similarly a large-R jet that originates from a particle tagged as a Z boson and contains two light flavor (b-)quarks is referred to as Z_{qq} (Z_{bb}). Finally, a particle tagged as a h boson whose decay is the origination point of a large-R jet containing 2 b-quarks is referred to as h_{bb}. To be identified as any of these, a large-R jet must pass the requisite tagging. This includes having the proper number of either light flavor or b-quarks tagged within the radius of the large-R jet (J_{qq} or J_{bb} tagging) as well as the reconstructed jet being consistent with the appropriate mass range as discussed above.

The performance of W_{qq}, Z_{qq},Z_{bb}, and h_{bb}-tagging, which includes both the tagging efficiency and the rejection factor, was carefully studied in the Run 2 analysis. These efficiency and rejection factors are used to weight MC simulated data and background in this analysis in the 4B category in place of explicit cuts in order to maintain background statistics as described in Section 5.4. This method is only used in the 4B category, explicit cuts are used in both the 4Q and 2B2Q categories.

5.6 Event Selection

5.6.1 Preselection

Some initial definitions and cuts apply to all of the following signal regions. All general trigger requirements imposed by the ATLAS detector must be met first. After that, all events require at least two tracks with a large transverse momentum ($p_{\mathrm{T}} > 500$ MeV) that are associated with a reconstructed vertex. A set of event cleaning cuts are imposed to ensure quality of measurements. Any events with a muon consistent with a cosmic muon (originates too far from the point of collision) are vetoed. There is a veto on non-collision backgrounds as well. This includes beam induced backgrounds such as muons generated by interactions between the beam and upstream collimators. Events with jets failing the *Loose* cleaning [35] are removed.

A $E_{\mathrm{T}}^{\mathrm{miss}}$cut is applied to be on trigger plateau to all events. Events are required to have at least two large-R jets. Applied event selection is always based on the two highest-p_{T}large-R jets. Events are vetoed if there is a lepton present. Both large-R jets are also required to pass boson tagging requirements. Backgrounds including leptonically decaying top-quarks are rejected by vetoing events that contain unmatched b-jets. To do this $n_{b-\mathrm{jet}}^{\mathrm{unmatched}} = 0$ is required where $n_{b-\mathrm{jet}}^{\mathrm{unmatched}}$ denotes the number of b-tagged track jets that are not matched to either of the two leading large-R jets.

The main SM backgrounds at this stage are $Z(\to \nu\nu) + \mathrm{jets}$, $W + \mathrm{jets}$ and $t\bar{t}$. A series of kinematic background rejection cuts are applied in order to suppress these backgrounds.

The kinematic cuts used for background rejection in this study include $E_{\mathrm{T}}^{\mathrm{miss}}$, min $\Delta\phi(E_{\mathrm{T}}^{\mathrm{miss}}, j)$, m_{eff}, and m_{T2}. The effective mass variable, m_{eff}, is defined as the sum of $E_{\mathrm{T}}^{\mathrm{miss}}$and the $p_{\mathrm{T}}$of the two leading large-R jets. Event shape is also useful to distinguish signals from backgrounds. Signal events tend to have a relatively spherical shape and the jets are typically isolated from $E_{\mathrm{T}}^{\mathrm{miss}}$. This is because the heavy electroweakinos are produced nearly at rest. On the other hand, background events generally have $E_{\mathrm{T}}^{\mathrm{miss}}$from a mismeasured jet. This means background events have a much higher chance of having $E_{\mathrm{T}}^{\mathrm{miss}}$that is aligned with a jet (the mismeasured jet typically). This can also be due to boosted top decays in $t\bar{t}$events, or in $Z(\to \nu\nu) + \mathrm{jets}$ and $W + \mathrm{jets}$, emission of collinear radiation. This motivates defining the variable min

$\Delta\phi(E_{\mathrm{T}}^{\mathrm{miss}}, j)$ which is the minimum azimuthal angle of separation between $E_{\mathrm{T}}^{\mathrm{miss}}$and the nearest small-$R$ jet.

The final kinematic cut, the stransverse mass variable, m_{T2} [69, 70], is also defined for the 2B2Q and 4B categories. The m_{T2} variable is a function of the momenta of the two visible particles and missing transverse momentum in an event. The stransverse mass is constructed by assigning the two leading large-R jets to the visible particle legs and is shown to effectively suppress some SM backgrounds, particularly $t\bar{t}$ which exhibits a kinematic cutoff around $m_{\mathrm{T2}} = 200$ GeV.

The optimization of these cuts is done for each of the categories independently, the following subsections detail the process of optimization as well as the selected kinematic cuts. For purposes of optimization, this analysis utilizes a profile-likelihood-ratio test statistic using flat 30% systematics in order to calculate significance values (Z_{n}).

5.6.2 Signal Region Definitions

Three orthogonal categories are defined, these include the two from the Run 2 paper, 4Q and 2B2Q, as well as the new 4B category that is considered in this extrapolation. These categories are defined by the presence of a large-R jet containing exactly two b-tagged jets (J_{bb}) for the qqbb final states (2B2Q), two such large-R jets for the 4B category, and the absence of such a large-R jet for the $qqqq$ final states (4Q). Boson tagging is applied to the two leading large-R jets, this requires them to pass V_{qq} tagging for the 4Q signal region (n(V_{qq})=2). In the case of the 2B2Q region this requires the J_{bb} to be tagged as either a Z or h boson, denoted Z_{bb} *and* h_{bb} with the other jet (J_{qq}) to pass the V_{qq} tagging. For the 4B region it is required that both large-R jets pass the J_{bb} tagging.

The first two categories have multiple SRs within them. For the 4Q region these include 4Q-WW, 4Q-WZ, and 4Q-ZZ. These require the leading large-R jets to pass two W_{qq} tagging, one W_{qq} and one Z_{qq} tag, and two Z_{qq} tags respectively. In the same way the 2B2Q category includes 2B2Q-WZ, 2B2Q-Wh, 2B2Q-ZZ, and 2B2Q-Zh where the first two contain a W_{qq}-tagged boson and the latter two a Z_{qq}-tagged boson. Then the second large-R jet contains the necessary Z_{bb}- or h_{bb}-tagging. These signal regions are illustrated in Figure 5.3. The 4B category contains just the 4B-hh region. This region must have two large-R jets which

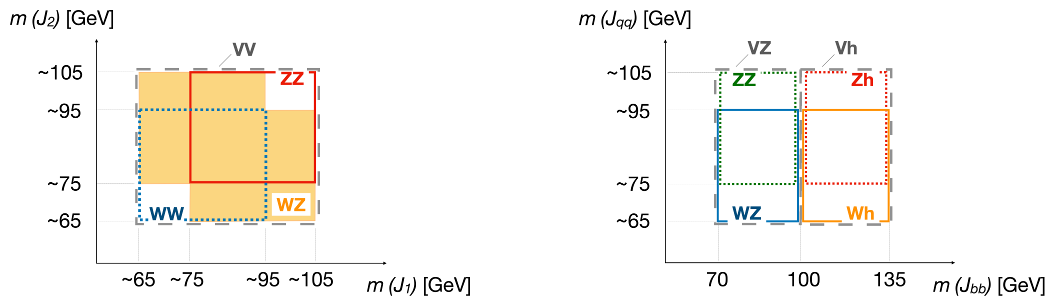

Figure 5.3: The segmentation of the 4Q and 2B2Q categories illustrated as a function of the masses of the two leading large-R jets. Both jets must pass the W_{qq}- or Z_{qq}-tagging for the 4Q category where as in the 2B2Q category one must pass either W_{qq}- or Z_{qq}-tagging while the other must pass either Z_{bb}- or h_{bb}-tagging. Notably, the W_{qq}- and Z_{qq}-boson tagging uses dynamic mass windows as a function of p_{T}so the mass windows pictured are typical values. This leaves significant overlap between the possible masses of each. The Z_{bb}- and h_{bb}-boson tagging, on the other hand, uses a fixed mass window shown on the right. The inclusive SRs, defined by the logical union of a few mutually overlapping SRs, are indicated by the gray dashed lines. The 4B category is not pictured here as only one signal region is included for this analysis.

pass h_{bb}-tagging.

The SR definitions are summarized in table 5.3. In total three, four, and one SRs are defined for the 4Q, 2B2Q, and 4B categories respectively. All signal regions are mutually orthogonal and are statistically combined according to the models.

5.6.3 4Q Signal Regions

The first category (4Q) is defined by the inclusion of two large-R jets both of which are tagged with two light flavor quarks (u, d, c, or s). This category was initially studied by focusing on the SR-4Q-WZ region as was done in the Run 2 study. This requires that one large-R jet is tagged as containing a W boson from the super-particle decay while the other is tagged as containing a Z boson. The 4Q SR also includes SR-4Q-WW and SR-4Q-ZZ. The number of b-tagged track-jets in the event is required to be less than two within this region to further reduce the $t\bar{t}$background. At this point kinematic cuts are applied and optimized for each SR.

In the Run 2 study it was found that the optimization of the WZ signal model was near enough the other two that it was sifficient to optimze for SR-4Q-WZ and apply the same kinematic cuts to all three regions. In this analysis SR-4Q-WW was found to deviate significantly from the other two, so a separate set of kinematic cuts were tested and applied for the WW signal model.

All preselection and background rejection cuts except for one are applied, the excluded cut is then varied to compare the remaining background events along with simulated signal events as seen for m_{eff} in Figure 5.4. The maximum significance value, while still maintaining sufficient background statistics in some cases, is found and the corresponding value for the kinematic cut is selected. This optimization process is applied to the kinematic cuts, $E_{\text{T}}^{\text{miss}}$, m_{eff}, and min $\Delta\phi(E_{\text{T}}^{\text{miss}}, j)$. All distributions used for optimization of kinematic cuts that are not included in the body of this note are found in the appendix.

In this extrapolation, having a much larger luminosity allows for even harder cuts than those in the Run 2 analysis.

Cuts are optimized for the C1N2-WZ model with $(m(\tilde{\chi}_1^{\pm}), m(\tilde{\chi}_1^0)) \approx (1300, 200)$ GeV. The applied cuts are $E_{\text{T}}^{\text{miss}} > 300$ GeV, $m_{\text{eff}} > 2200$ GeV, and min $\Delta\phi(E_{\text{T}}^{\text{miss}}, j) > 1.6$. It is important to note that the m_{eff} and $E_{\text{T}}^{\text{miss}}$cuts are correlated. The optimization for this note was done iteratively across all kinematic variables, in this process the greatest significance was found with a very tight cut on m_{eff} and a cut on $E_{\text{T}}^{\text{miss}}$that removes essentially no signal or background for this region. A more relevant cut on $E_{\text{T}}^{\text{miss}}$was ideal in the Run 2 study and this cut should still be considered in future versions of this analysis.

In the process of optimizing cuts for the C1C1-WW model, it was also found that the $(m(\tilde{\chi}_1^{\pm}), m(\tilde{\chi}_1^0)) \approx (1100, 500)$ GeV mass point gave better results. The distribution of min $\Delta\phi(E_{\text{T}}^{\text{miss}}, j)$ in SR-4Q-WW with all other cuts applied is shown in Figure 5.4.

Cuts are optimized for the C1C1-WW model with $(m(\tilde{\chi}_1^{\pm}), m(\tilde{\chi}_1^0)) \approx (1100, 500)$ GeV. The applied cuts are $E_{\text{T}}^{\text{miss}} > 500$ GeV, $m_{\text{eff}} > 1700$ GeV, and min $\Delta\phi(E_{\text{T}}^{\text{miss}}, j) > 1.2$.

5.6.4 2B2Q Signal Regions

The second category, 2B2Q, includes four signal regions as previously defined: SR-2B2Q-WZ, SR-2B2Q-ZZ, SR-2B2Q-Wh, and SR-2B2Q-Zh. Just as the SR-4Q-WZ was used to model the 4Q category, 2B2Q is modeled by SR-2B2Q-Wh. The kinematic cuts are optimized for SR-2B2Q-Wh and the selected cuts are

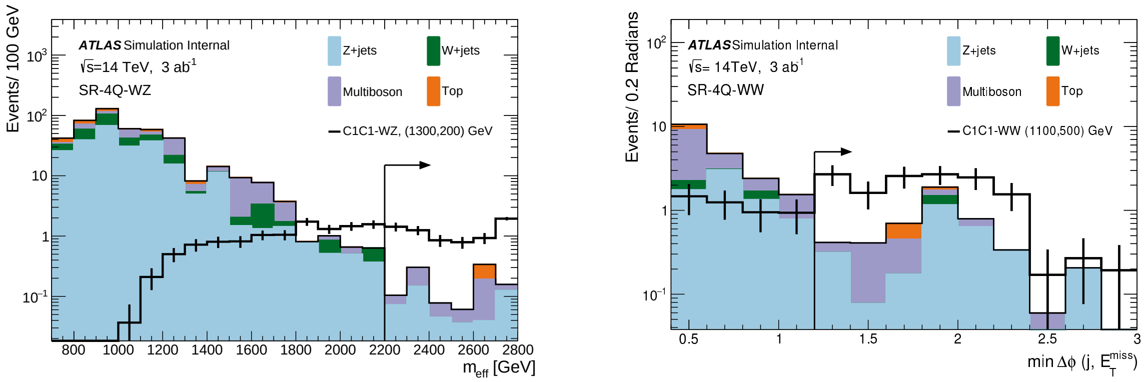

Figure 5.4: The m_{eff} distribution for the 4Q-WZ signal region (left) and min $\Delta\phi(E_{\mathrm{T}}^{\mathrm{miss}}, j)$ distribution for the 4Q-WW signal region (right). The plot shows number of events in MC simulation for signal events and each background. All selection criteria other than the kinematic variable being viewed are applied. The far right bin includes the overflow. The arrow represents the selected cuts for the purpose of optimization. The simulated signals are of the ($\tilde{W}$, $\tilde{B}$) model with $(m(\tilde{\chi}_1^{\pm}), m(\tilde{\chi}_1^0))$ $\approx (1300, 200)$ GeV for 4Q-WZ and $\approx (1100, 500)$ GeV for 4Q-WW.

applied to all four signal regions within the 2B2Q category.

The same kinematic variables are used in the 2B2Q category as in the 4Q category with the addition of the stransverse mass (m_{T2}), which is used in both the 2B2Q and 4B categories. The m_{eff} distribution for the 2B2Q category with all other cuts applied is seen in Figure 5.5.

The cuts are optimized for the mass point $(1300, 200)$ GeV. The optimized cuts for the 2B2Q category are $E_{\mathrm{T}}^{\mathrm{miss}} > 600$ GeV, $m_{\mathrm{eff}} > 1600$ GeV, $m_{\mathrm{T2}} > 500$ GeV, and min $\Delta\phi(E_{\mathrm{T}}^{\mathrm{miss}}, j) > 1.0$.

5.6.5 4B Signal Region

The final SR is SR-4B-GGM-hh which explores the gravitino LSP model. In this case a simulated sample with a higgsino mass of ≈ 1300 GeV is used for initial modeling and kinematic cuts will be selected for this category.

In this category, due to low MC statistics for the background, the explicit boson tagging and b-tagging cuts could not be applied. This would result in extremely low statistics for the extrapolation to 3 ab^{-1} and the statistical uncertainties would dominate. Instead, the boson tagging efficiency and background rejection found in the Run 2 analysis are applied in order to reweight the signal and background estimations respectively [89]. A closure check was done on these two methods by applying both the explicit cuts as

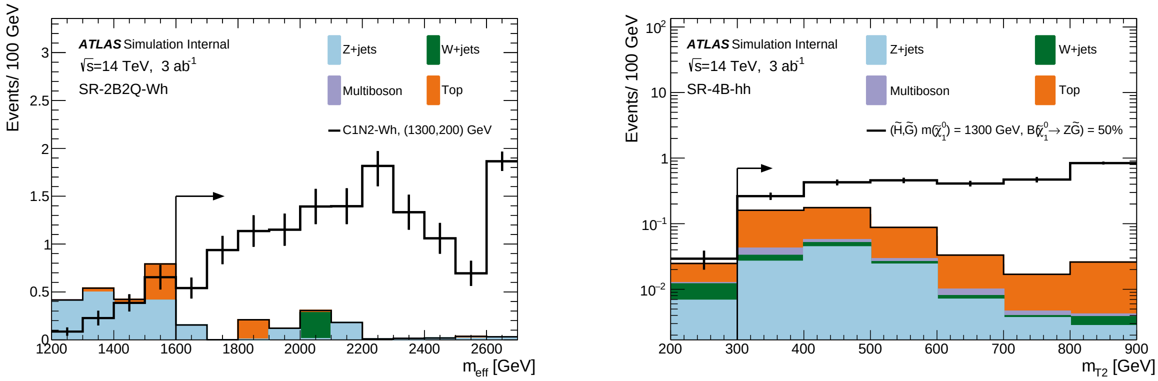

Figure 5.5: The m_{eff} distribution for the 2B2Q category (left) and m_{T2} distribution for the 4B category (right). The plot shows number of events in MC simulation for signal events and each background. All selection criteria other than the kinematic variable being viewed are applied. The far right bin includes the overflow. The arrow represents the selected cuts for the purpose of optimization. Note that this cut looks somewhat loose, this is due to the low background statistics available. Tightening the cut very quickly causes a significant loss of background MC and the increase in error limits the significance value. Keeping a looser cut, given the amount of background MC available, maintains the highest significance; this cut, in an HL-LHC analysis where much higher MC statistics will be available, can likely be made much tighter. The simulated signals are of the $(\tilde{W},\,\tilde{B})$ model with with a mass splitting of approximately $(1300, 200)$ GeV for the 2B2Q region and the GGM model with a mass point of 1300 GeV and a 50% branching ratio to Z/h for the 4B category.

well as the signal and background reweighting to simulate the cuts to a Monte Carlo sample. This check found the reweighting process to be accurate with a maximum discrepancy of 20% less signal when using the reweighting method. This difference has little to no impact on the final exclusion regions and if anything gives a slightly conservative estimate. Increasing the signal by $\approx$ 20%, consistent with the explicit cuts, may result in an improved limit of roughly 50 GeV.

The low MC statistics also affects the optimization process of this region. During the optimization process kinematic selections are made not just to maximize the significance value, Z_{n}, but also to maintain sufficient background in order to avoid excess statistical error. For this reason the kinematic selections made are often slightly softer than the significance alone would warrant. The m_{T2} distribution showing the optimal cut for the 4B category is showin in Figure 5.5. The optimized cuts for the 4B category are $E_{\text{T}}^{\text{miss}}$> 400 GeV, m_{eff} > 1100 GeV, $m_{\text{T2}} > 300$ GeV, and min $\Delta\phi(E_{\text{T}}^{\text{miss}}, j) > 1.0$.

The cuts used in each category are presented in table 5.2. The SR definitions are summarized in table

Table 5.2: Summary of selections for the SRs. $n(V_{qq})$ represents the number of large-R jets passing V_{qq}-tagging of the two highest-p_{T}large-R jets. The trigger selection and event cleaning described in Section 4.4 are also applied.

	4Q	4Q-WW	2B2Q	4B
$n_{\text{Large}-R\text{ jets}}$	≥ 2	≥ 2	≥ 2	≥ 2
n_{lepton}	$= 0$	$= 0$	$= 0$	$= 0$
$n(V_{qq})$	$= 2$	$= 2$	$= 1$	$= 0$
$n(J_{bb})$	$= 0$	$= 0$	$= 1$	$= 2$
$m(J_{bb})$ [GeV]	-	-	$\in [70, 135]$	$\in [70, 135]$
$n_{b-\text{jet}}^{\text{unmatched}}$	$= 0$	$= 0$	$= 0$	$= 0$
$n_{b-\text{jet}}$	≤ 1	≤ 1	-	-
$E_{\mathrm{T}}^{\text{miss}}$ [GeV]	> 300	> 500	> 600	> 400
m_{eff} [GeV]	> 2200	> 1700	> 1600	> 1100
$\min \Delta\phi(E_{\mathrm{T}}^{\text{miss}}, j)$	> 1.6	> 1.2	> 1.0	> 1.0
m_{T2} [GeV]	-	-	> 500	> 300

5.3.

Table 5.3: Definition of each SR in the 4Q, 2B2Q, and 4B categories; where $n(W_{qq})$, $n(Z_{qq})$, $n(V_{qq})$, $n(Z_{bb})$, and $n(h_{bb})$ are respectively the number of large-R jets passing the W_{qq}-, Z_{qq}-, V_{qq}-, Z_{bb}-, and h_{bb}-tagging of the two leading large-R jets. SR-4Q-WZ requires $n(W_{qq}), n(Z_{qq}) \geq 1$ instead of $n(W_{qq}) = n(Z_{qq}) = 1$ because the selections in W_{qq}- and Z_{qq}-tagging are not exclusive.

	$n(W_{qq})$	$n(Z_{qq})$	$n(V_{qq})$	$n(Z_{bb})$	$n(h_{bb})$
4Q-WW	$= 2$	-	$= 2$	$= 0$	$= 0$
4Q-WZ	≥ 1	≥ 1	$= 2$	$= 0$	$= 0$
4Q-ZZ	-	$= 2$	$= 2$	$= 0$	$= 0$
2B2Q-WZ	$= 1$	-	$= 1$	$= 1$	$= 0$
2B2Q-ZZ	-	$= 1$	$= 1$	$= 1$	$= 0$
2B2Q-Wh	$= 1$	-	$= 1$	$= 0$	$= 1$
2B2Q-Zh	-	$= 1$	$= 1$	$= 0$	$= 1$
4B-hh	-	-	-	$= 0$	$= 2$

5.7 Results

A flat 30% systematic uncertainty is assigned to simulated events and background in this analysis. This 30% was chosen based on observations from the Run 2 analysis in order to give a conservative estimate. The MC statistical uncertainty is smaller than this assigned systematic uncertainty in all regions except for SR-4B where statistical uncertainty is very high. It is important to note however that this uncertainty does not have a large impact on the final limits. Varying this between $\approx$ 20% to 40% causes a change in the final limits of less than 25 GeV.

All exclusion limits are calculated at 95% CL for a 1-sided confidence interval (Z_{n}=1.65). The limits are compared to the published results from the Run 2 analysis. It is important to note that the Run 2 published results are exclusion limits calculated from observed events. Table 5.4 shows the predicted signal event yields in each SR as well as the backgrounds yields estimated for each source from MC. As seen in the table, the dominant background is $Z(\rightarrow \nu\nu) + \text{jets}$ for the 2B2Q and 4Q categories while the 4B category has similar contributions from $Z(\rightarrow \nu\nu) + \text{jets}$ and top.

These signal regions are then combined in various ways for the different models that were targeted in this analysis. The $(\widetilde{W}, \widetilde{B})$ mass hierarchy is represented by the simplified models C1C1-WW, C1N2-WZ and C1N2-Wh. The C1C1-WW model only includes contributions from the 4Q category. The C1N2-WZ model is composed of pieces from both the 4Q and 2B2Q categories. The C1N2-Wh model is made up entirely of portions from the 2B2Q category. Finally the GGM scenario includes portions from all three categories; 4Q, 2B2Q, and 4B. When combining orthogonal SRs, the overall sensitivity estimate is obtained by adding the Z_{n} values from each individual SR in quadrature.

The 95% CL exclusion limit for the C1C1-WW simplified model is shown in Figure 5.6. For this model, $m(\widetilde{\chi}_1^{\pm})$ between 625 GeV and 1450 GeV could be excluded for $m(\widetilde{\chi}_1^0) < 280$ GeV. This is to be compared to the Run 2 search, where exclusion limits were set on $m(\widetilde{\chi}_1^{\pm})$ between 620 GeV and 760 GeV for $m(\widetilde{\chi}_1^0) < 60$ GeV. The increased sensitivity expected in the HL-LHC can lead to increases in the mass reach of slightly over 90% based on this study.

The 95% CL exclusion limit for the C1N2-WZ simplified model is shown in Figure 5.7, where the limits

Table 5.4: Number of predicted MC data events and the SM backgrounds in the SRs. Negligible contributions are indicated by "-". The top set of rows shows all four $(\widetilde{W}, \widetilde{B})$ SRs. The notation in the first two rows of these regions, written Signal(A, B), indicates the number of Monte Carlo signal events for the mass splitting (A, B) GeV of $(\widetilde{\chi}_{\text{heavy}}, \widetilde{\chi}_{\text{light}})$. Similarly the next two rows are the significance (Z_{n}) values for the relevant mass splittings. The bottom set of rows shows the four SRs that are included in the $(\widetilde{H}, \widetilde{G})$ model. In this case the first two rows of use the notation Signal(X) indicating the number of MC signal events for the mass point X GeV with the branching ratio that gives the maximum yield. The next two rows are similarly the significance values for the corresponding mass point, again with the branching ratio that gives the greatest Z_{n} value. To avoid unnecessary granularity, the background category top is a combination of $t\bar{t}$, $t\bar{t}+X$, and $t+X$ and the category multiboson is a combination of diboson, tri-boson, and higgs.

$(\widetilde{W}, \widetilde{B})$-SIM				
Region	SR-4Q-WW	SR-4Q-WZ	SR-2B2Q-WZ	SR-2B2Q-Wh
Signal$(1100, 500)$ GeV	9.75 ± 1.00	1.13 ± 0.50	3.69 ± 0.83	11.3 ± 1.1
Signal$(1300, 200)$ GeV	8.59 ± 0.40	7.20 ± 0.52	3.61 ± 0.37	13.3 ± 0.57
$Z_{\text{n}}(1100, 500)$ GeV	2.84	0.91	3.63	5.78
$Z_{\text{n}}(1300, 200)$ GeV	2.57	4.01	3.57	6.45
Total Background	4.60 ± 0.87	1.04 ± 0.29	0.25 ± 0.14	0.86 ± 0.37
$W+$jets	0.33 ± 0.33	-	-	0.27 ± 0.27
$Z(\rightarrow \nu\nu)+$jets	2.96 ± 0.69	0.46 ± 0.11	0.17 ± 0.13	0.53 ± 0.25
multiboson	0.43 ± 0.23	0.43 ± 0.23	0.70 ± 0.43	0.050 ± 0.026
top	1.15 ± 0.37	0.15 ± 0.15	-	-
$(\widetilde{H}, \widetilde{G})$				
Region	SR-4B-hh	SR-2B2Q-ZZ	SR-2B2Q-Zh	SR-4Q-ZZ
Signal(1300) GeV	6.02 ± 0.26	4.81 ± 0.82	6.25 ± 0.41	7.26 ± 1.02
Signal(1500) GeV	1.74 ± 0.07	3.58 ± 0.50	3.77 ± 0.22	6.67 ± 0.68
$Z_{\text{n}}(1300)$ GeV	4.48	4.04	3.33	4.51
$Z_{\text{n}}(1500)$ GeV	1.80	3.28	2.26	4.25
Total Background	0.44 ± 0.03	0.35 ± 0.20	1.34 ± 0.46	0.71 ± 0.25
$W+$jets	0.016 ± 0.002	-	0.27 ± 0.27	-
$Z(\rightarrow \nu\nu)+$jets	0.099 ± 0.012	0.30 ± 0.19	1.03 ± 0.37	0.34 ± 0.10
multiboson	0.017 ± 0.004	0.046 ± 0.035	0.031 ± 0.021	0.37 ± 0.22
top	0.20 ± 0.03	-	-	-

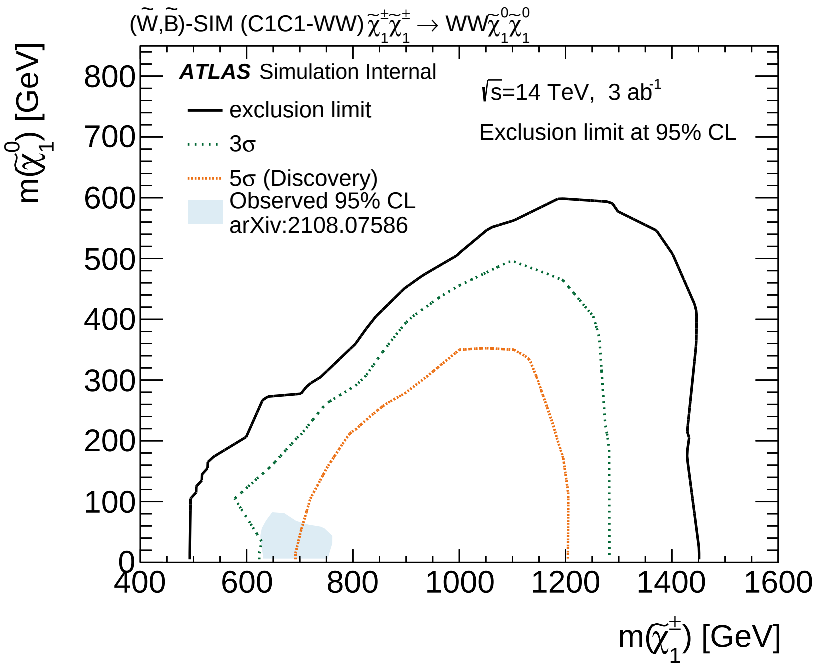

Figure 5.6: C1C1-WW physics model significance contour that includes only SR-4Q-WW. The exclusion limit is calculated at 95% CL ($Z_{\rm n}$=1.65). The blue region represents the 95% exclusion limit found in the Run 2 analysis calculated from observed events. The 5σ contour represents the projected limit for potential discovery.

on $m(\tilde{\chi}_1^{\pm}/\tilde{\chi}_2^0)$ could be from 900 GeV to 1595 GeV for $m(\tilde{\chi}_1^0) < 500$ GeV. For the same simplified model, the Run 2 analysis was able to exclude $m(\tilde{\chi}_1^{\pm}/\tilde{\chi}_2^0)$ between 440 GeV and 960 GeV for $m(\tilde{\chi}_1^0) < 300$ GeV. This leads to an increase of slightly greater than 65% in the mass reach.

The 95% CL exclusion limit for the C1N2-Wh simplified model is shown in Figure 5.8. In the HL-HLC upgrade conditions it is predicted that exclusion limits on $m(\tilde{\chi}_1^{\pm}/\tilde{\chi}_2^0)$ can be set from 950GeV to 1675 GeV for $m(\tilde{\chi}_1^0) < 575$ GeV. This presents an increase in the mass reach of just over 55% compared to the Run 2 search, which was able to exclude $m(\tilde{\chi}_1^{\pm}/\tilde{\chi}_2^0)$ between 400 GeV and 1060 GeV for $m(\tilde{\chi}_1^0) < 400$ GeV.

Finally, the 95% CL exclusion limit for the $(\widetilde{H},\widetilde{G})$ simplified model is shown in Figure 5.9. The limit is given in a plane defined by the mass of the lightest higgsino ($m(\tilde{\chi}_1^0)$) and the branching ratio $\mathcal{B}(\tilde{\chi}_1^0 \rightarrow Z\widetilde{G})$. The top of the plot corresponds to a 100% branching ratio to Z bosons, while the bottom represents a branching ratio entirely to the h boson. For any branching ratio, $m(\tilde{\chi}_1^0)$ below 1575 GeV is expected to be excluded, while this can limit can extend up to 1725 GeV for $\mathcal{B}(\tilde{\chi}_1^0 \rightarrow Z\widetilde{G}) = 0\%$. In the Run 2 search,

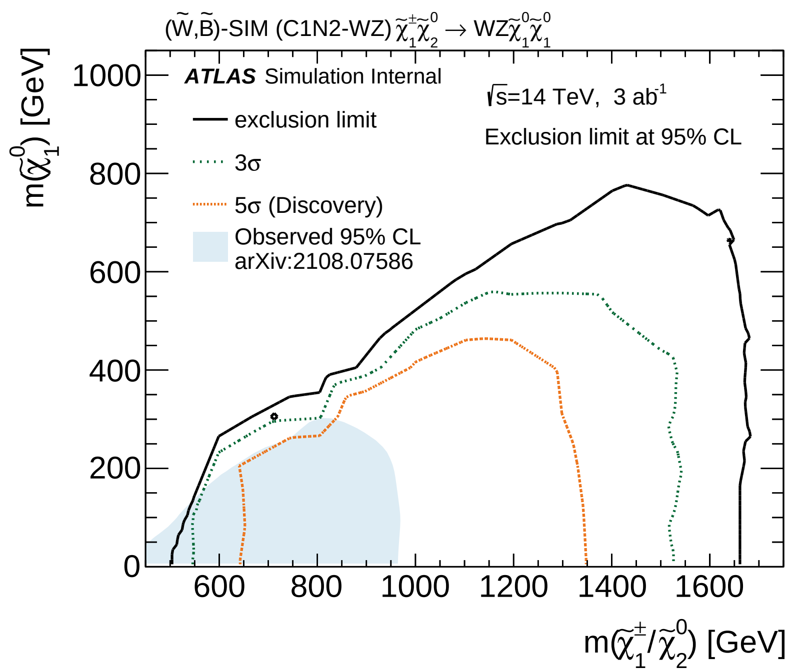

Figure 5.7: The C1N2-WZ physics model significance contour that is a combination of SR-4Q-WZ and SR-2B2Q-WZ. Z_{n} values are added quadratically. The exclusion limit is calculated at 95% CL (Z_{n}=1.65). The blue region represents the 95% exclusion limit found in the Run 2 analysis. The 5σ contour represents the projected limit for potential discovery.

$m(\tilde{\chi}_1^0)$ between 450 (500) GeV and 940 (850) GeV was excluded for models with $\mathcal{B}(\tilde{\chi}_1^0 \rightarrow Z\widetilde{G}) > 80$ (50)%. The ability for this upgrade study to reach $\mathcal{B}(\tilde{\chi}_1^0 \rightarrow Z\widetilde{G}) < 50\%$ with strong limits is a result of the inclusion of SR-4B-hh. This improvement in the mass reach is roughly 80%.

One ideal outcome of upgrading to the HL-LHC and revisiting this and other studies is to actually discover a SUSY particle, so the 5σ region (innermost contour on each exclusion plot) of this study is very motivating. The discovery potential predicted by this analysis with HL-LHC data is significantly beyond existing exclusion ranges from current analyses.

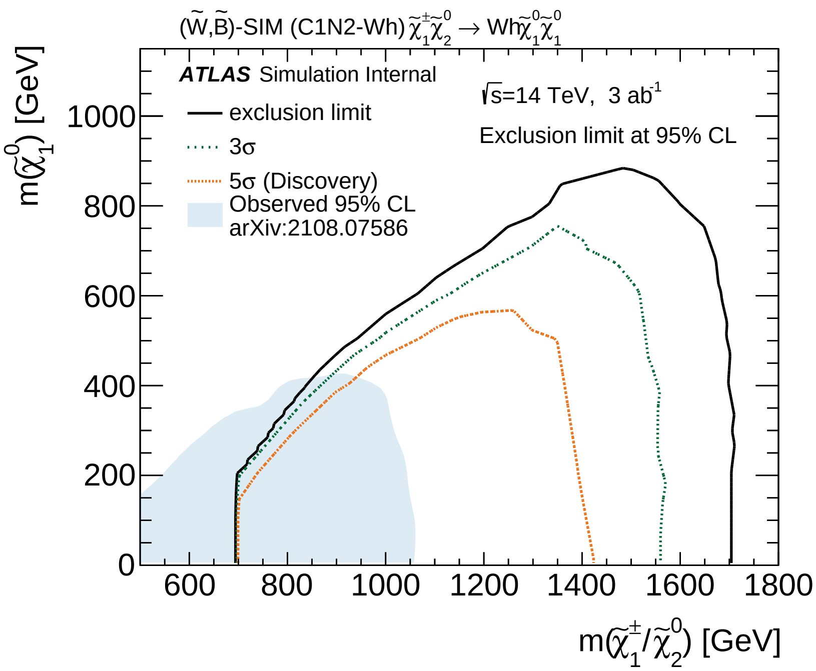

Figure 5.8: The C1N2-Wh physics model significance contour that is modeled entirely from SR-2B2Q-Wh. The exclusion limit is calculated at 95% CL (Z_{n}=1.65). The blue region represents the 95% exclusion limit found in the Run 2 analysis. The 5σ contour represents the projected limit for potential discovery.

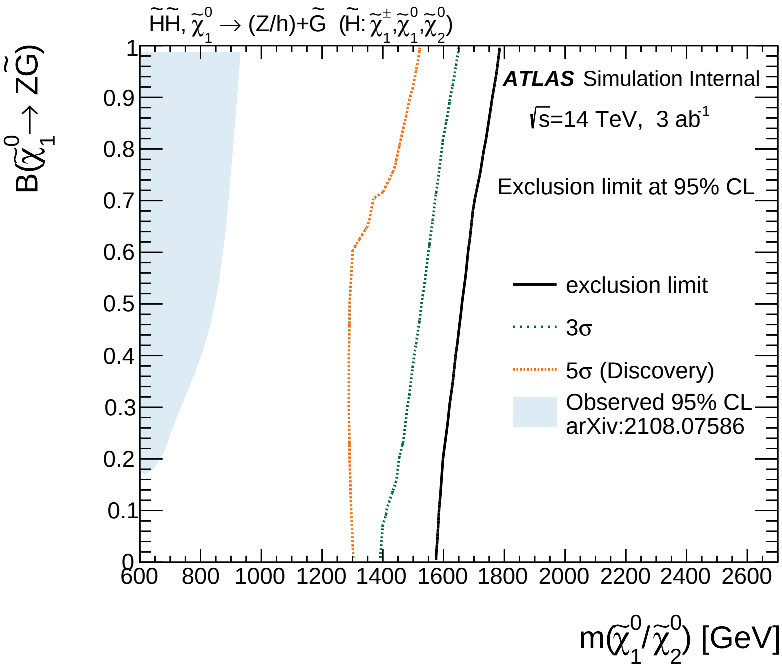

Figure 5.9: GGM scenario significance contour utilizing boson efficiency and background rejection reweighting representing the 4B-hh signal region. This is a combination that also contains SR-2B2Q-ZZ, SR-2B2Q-Zh, and SR-4Q-ZZ all of which were modeled using explicit boson tagging cuts. The exclusion limit is calculated at 95% CL (Z_n=1.65). The y-axis shows the branching ratio of the lightest neutral higgsino into either a Z- or h boson. The top of the plot shows 100% decays into Z and the bottom shows decays entirely to the h bososn. The blue region represents the 95% exclusion limit found in the Run 2 analysis. The 5σ contour represents the projected limit for potential discovery.

5.8 Conclusion

This chapter presents a study to assess the sensitivty of the HL-LHC with the upgraded ATLAS detector to electroweak production of SUSY particles in final states with two boosted bosons decaying to fully hadronic final states. The study used Monte Carlo simulation extrapolated to a luminosity of 3 ab^{-1} at $\sqrt{s} = 14$ TeV. This study includes $(\widetilde{W}, \widetilde{B})$ simplified models as well as a massless Gravitino LSP. Both models show promising prospects for further study and are expected to achieve 5σ discovery potenatial over a wide range of masses that are not excluded by current searches.

CHAPTER 6

CONCLUSION

This thesis presented descriptions of TRT operations and upkeep, compression studies, and a resynchronization error investigations as well as results from the Run 2 fully hadronic SUSY search and the extrapolation of that search to HL-LHC conditions.

The details of DAQ operations discussed included contributions from the entire TRT DAQ team over many years putting in huge amounts of upkeep, maintenance, and at times very stressful troubleshooting when problems arise quickly. The success of the TRT over these years is heavily reliant on the contributions of every single team member. Plans were made to update data compression schemes from the end of Run 2 going into Run 3 allowing for a smooth transition when ATLAS resumed data taking. Despite improved performance of a lossy compression scheme that was developed, limitations in the firmware made implementation unfeasible. The lossless compression scheme using Huffman encoding was sufficient for data taking in Run 3 with minor changes needing to be made in order to update the restrictions placed on the length of the "zero word". A long and detailed investigation into frequent resynchronization of the TRT was conducted across multiple years lasting from Run 2 well into Run 3. Precise measurements were performed to better understand the limits of the electronics being used and without being able to pinpoint the exact circumstances that cause the errors or fully fix them, mitigation methods have proved to be extremely effective and the TRT has remained one of the lowest in dead time contribution in the ATLAS detector.

The first fully hadronic final state SUSY search conducted in ATLAS was presented. This analysis was conducted on data with an integrated luminosity of 140 fb^{-1} of proton–proton collisions collected at $\sqrt{s} =$ 13 TeV. The search was made possible by and heavily utilized improvements to the reconstruction and boson tagging techniques. Special attention was given to descriptions of the QCD multijet background estimations using the ABCD method. Multiple physics models were studied in the search including the baseline MSSM scenario where $\widetilde{\chi}_{\text{heavy}}$ and $\widetilde{\chi}_{\text{light}}$ are modeled as bino, wino, and higgsino electroweakinos, along with the gravitino LSP scenario based on the GGM model and SM extension with a QCD axion resulting in an axino LSP. No excess was found in the search, but some of the strongest limits in ATLAS from Run 2 were set. For the MSSM scenarios, chargino pair production with a chargino mass between 630 and 760 GeV was excluded and chargino-neutralino production with wino masses between 440 and 960 GeV and between 400 and 1060 GeV were excluded for a decays into a WZ and Wh respectively. In the GGM model limits were set dependent on the branching ratio. For $\mathcal{B}(\tilde{\chi}_1^0 \to Z\tilde{G}) = 100\%$ and 50% m($\tilde{\chi}_{light}$), from 450 to 940 GeV and 500 to 850 GeV were excluded respectively. Similar limits were set for the axino model where 450 to 940 GeV was excluded for an axino mass less than 300 GeV and between 500 and 850 GeV were excluded for axino mass less than 210 GeV.

Finally an extrapolation of the fully hadronic Run 2 search to HL-LHC conditions was detailed. The most impactful change in this extrapolation is an increase in the integrated luminosity going from 140 fb^{-1} of proton–proton collisions to the projected 3 ab^{-1}. The Run 2 search was also only able to use the 4Q and 2B2Q regions in order to maintain orthogonality with a separate analysis focused on the 4B final state. In this extrapolation all three regions were included. Finally the projected increase in center-of-mass energy to $\sqrt{s} = 14$ TeV was accounted for using changes to the cross sections of both signal and background processes. Strong increases in the sensitivity for both discovery and exclusion are predicted based on the extrapolation. For the C1C1-WW simplified model, $m(\widetilde{\chi}_1^{\pm})$ between 625 GeVand 1450 GeVcould be excluded, representing an increase in the mass reach of slightly over 90%. In the C1N2-WZ simplified model an increase of slightly greater than 65% in the mass reach is observed where exclusion of $m(\widetilde{\chi}_1^{\pm}/\widetilde{\chi}_2^0)$ could be from 900 GeVto 1595 GeV. For the last simplified model, C1N2-Wh, exclusion limits on $m(\widetilde{\chi}_1^{\pm}/\widetilde{\chi}_2^0)$ could be set up to 950 GeVto 1675 GeVgiving an increase in the mass reach of just over 55%. Finally in the $(\widetilde{H}, \widetilde{G})$ model limits were set dependent on the branching ratio. The exclusion sensitivty for all branching ratios included $m(\widetilde{\chi}_1^0)$ below 1575 GeVand for $\mathcal{B}(\widetilde{\chi}_1^0 \rightarrow Z\widetilde{G}) = 0\%$ the exclusion sensitivty can extend up to 1725 GeVgiving an improvement in the mass reach of roughly 80%. Notably the strong limits for $\mathcal{B}(\widetilde{\chi}_1^0 \rightarrow Z\widetilde{G}) < 50\%$ is a result of the inclusion of the 4B region in the search. This extrapolation gives strong motivation for this search to be conducted with HL-LHC data in the future.

BIBLIOGRAPHY

[1] L. R. Evans and P. Bryant, *LHC Machine*, JINST **3** (2008) S08001, This report is an abridged version of the LHC Design Report (CERN-2004-003), URL: https://cds.cern.ch/record/1129806 (cit. on p. 18).

[2] ATLAS Collaboration, *The ATLAS Experiment at the CERN Large Hadron Collider*, JINST **3** (2008) S08003 (cit. on p. 23).

[3] D. O. M. H. J. S. P. Wagner, *'Readout of the ATLAS Transition Radiation Tracker: Data Structure and Detector Granularity'*, https://cds.cern.ch/record/1179456 (cit. on pp. 48, 51).

[4] K. Yoshihara, *'TRT DAQ Performance for Run 2'*, https://cds.cern.ch/record/2282001 (cit. on pp. 48, 49).

[5] I. Dyckes, *'TRT Compression and Readout Performance in Run 2'*, https://cds.cern.ch/record/2640983 (cit. on pp. 49, 52, 53, 55).

[6] J. Mullin, *'TRT Compression Studies'*, https://twiki.cern.ch/twiki/bin/view/Atlas/TrtQualification (cit. on p. 58).

[7] J. Mullin, *'TRT DAQ DOCS Introduction'*, https://atlas-trt-daq-docs.web.cern.ch/Introduction/ (cit. on p. 61).

[8] G. Giudice and A. Romanino, *Split supersymmetry*, Nucl. Phys. B **699** (2004) 65, arXiv: hep-ph/0406088 (cit. on p. 63), Erratum: Nucl. Phys. B **706** (2005) 65.

[9] N. Arkani-Hamed and S. Dimopoulos, *Supersymmetric unification without low energy supersymmetry and signatures for fine-tuning at the LHC*, JHEP **06** (2005) 073, arXiv: hep-th/0405159 (cit. on p. 63).

[10] T. Han, S. Padhi, and S. Su, *Electroweakinos in the light of the Higgs boson*, Phys. Rev. D **88** (2013) 115010, arXiv: 1309.5966 [hep-ph] (cit. on p. 64).

[11] A. Djouadi, M. M. Mühlleitner, and M. Spira, *Decays of Supersymmetric particles: The Program SUSY-HIT (SUspect-SdecaY-Hdecay-InTerface)*, Acta Phys. Polon. B **38** (2007) 635, arXiv: hep-ph/0609292 (cit. on p. 65).

[12] ATLAS Collaboration, *Search for electroweak production of charginos and sleptons decaying into final states with two leptons and missing transverse momentum in $\sqrt{s} = 13$ TeV pp collisions using the ATLAS detector*, Eur. Phys. J. C **80** (2020) 123, arXiv: 1908.08215 [hep-ex] (cit. on pp. 65, 90, 95).

[13] CMS Collaboration, *Searches for pair production of charginos and top squarks in final states with two oppositely charged leptons in proton–proton collisions at $\sqrt{s} = 13$ TeV*, JHEP **11** (2018) 079, arXiv: 1807.07799 [hep-ex] (cit. on pp. 65, 95).

[14] ATLAS Collaboration, *Search for chargino-neutralino pair production in final states with three leptons and missing transverse momentum in $\sqrt{s} = 13$ TeV pp collisions with the ATLAS detector*, ATLAS-CONF-2020-015, 2020, URL: https://cds.cern.ch/record/2719521 (cit. on pp. 65, 90, 95).

[15] ATLAS Collaboration, *Search for chargino–neutralino production using recursive jigsaw reconstruction in final states with two or three charged leptons in proton–proton collisions at $\sqrt{s} = 13$ TeV with the ATLAS detector*, Phys. Rev. D **98** (2018) 092012, arXiv: 1806.02293 [hep-ex] (cit. on pp. 65, 95).

[16] ATLAS Collaboration, *Search for chargino–neutralino production with mass splittings near the electroweak scale in three-lepton final states in $\sqrt{s} = 13$ TeV pp collisions with the ATLAS detector*, Phys. Rev. D **101** (2020) 072001, arXiv: 1912.08479 [hep-ex] (cit. on pp. 65, 95).

[17] CMS Collaboration, *Search for new phenomena in final states with two opposite-charge, same-flavor leptons, jets, and missing transverse momentum in pp collisions at $\sqrt{s} = 13$ TeV*, JHEP **03** (2018) 076, arXiv: 1709.08908 [hep-ex] (cit. on pp. 65, 95).

[18] CMS Collaboration, *Combined search for electroweak production of charginos and neutralinos in proton–proton collisions at $\sqrt{s} = 13$ TeV*, (2018), arXiv: 1801.03957 [hep-ex] (cit. on pp. 65, 95).

[19] ATLAS Collaboration, *Search for chargino and neutralino production in final states with a Higgs boson and missing transverse momentum at $\sqrt{s} = 13$ TeV with the ATLAS detector*, Phys. Rev. D **100** (2019) 012006, arXiv: 1812.09432 [hep-ex] (cit. on pp. 65, 95).

[20] ATLAS Collaboration, *Search for direct production of electroweakinos in final states with missing transverse momentum and a Higgs boson decaying into photons in pp collisions at $\sqrt{s} = 13$ TeV with the ATLAS detector*, JHEP **10** (2020) 005, arXiv: 2004.10894 [hep-ex] (cit. on pp. 65, 95).

[21] ATLAS Collaboration, *Search for direct production of electroweakinos in final states with one lepton, missing transverse momentum and a Higgs boson decaying into two b-jets in pp collisions at $\sqrt{s} = 13$ TeV with the ATLAS detector*, Eur. Phys. J. C **80** (2020) 691, arXiv: 1909.09226 [hep-ex] (cit. on pp. 65, 90, 95).

[22] CMS Collaboration, *Search for electroweak production of charginos and neutralinos in multilepton final states in proton–proton collisions at $\sqrt{s} = 13$ TeV*, (2017), arXiv: 1709.05406 [hep-ex] (cit. on pp. 65, 95).

[23] CMS Collaboration, *Search for electroweak production of charginos and neutralinos in WH events in proton–proton collisions at $\sqrt{s} = 13$ TeV*, JHEP **11** (2017) 029, arXiv: 1706.09933 [hep-ex] (cit. on pp. 65, 95).

[24] CMS Collaboration, *Search for supersymmetry with Higgs boson to diphoton decays using the razor variables at $\sqrt{s} = 13$ TeV*, Phys. Lett. B **779** (2018) 166, arXiv: 1709.00384 [hep-ex] (cit. on pp. 65, 95).

[25] P. Meade, N. Seiberg, and D. Shih, *General Gauge Mediation*, Prog. Theor. Phys. Suppl. **177** (2009) 143, arXiv: 0801.3278 [hep-ph] (cit. on p. 65).

[26] C. Cheung, A. L. Fitzpatrick, and D. Shih, *(Extra)ordinary gauge mediation*, JHEP **07** (2008) 054, arXiv: 0710.3585 [hep-ph] (cit. on p. 65).

[27] M. Dine and W. Fischler, *A phenomenological model of particle physics based on supersymmetry*, Phys. Lett. B **110** (1982) 227 (cit. on p. 65).

[28] L. Alvarez-Gaumé, M. Claudson, and M. B. Wise, *Low-energy supersymmetry*, Nucl. Phys. B **207** (1982) 96 (cit. on p. 65).

[29] C. R. Nappi and B. A. Ovrut, *Supersymmetric extension of the SU(3) x SU(2) x U(1) model*, Phys. Lett. B **113** (1982) 175 (cit. on p. 65).

[30] ATLAS Collaboration, *Search for pair production of higgsinos in final states with at least three b-tagged jets in $\sqrt{s} = 13$ TeV pp collisions using the ATLAS detector*, Phys. Rev. D **98** (2018) 092002, arXiv: `1806.04030 [hep-ex]` (cit. on pp. 65, 95).

[31] ATLAS Collaboration, *Search for supersymmetry in events with four or more leptons in 139 fb^{-1} $\sqrt{s} = 13$ TeV pp collisions with the ATLAS detector*, ATLAS-CONF-2020-040, 2020, URL: `https://cds.cern.ch/record/2727861` (cit. on pp. 65, 95).

[32] R. D. Peccei and H. R. Quinn, *CP Conservation in the Presence of Pseudoparticles*, Phys. Rev. Lett **38** (1977) 328 (cit. on p. 66).

[33] S. Weinberg, *A New Light Boson?*, Phys. Rev. Lett. **40** (1978) 223 (cit. on p. 66).

[34] F. Wilczek, *Problem of Strong P and T Invariance in the Presence of Instantons*, Phys. Rev. Lett. **40** (1978) 279 (cit. on p. 66).

[35] ATLAS Collaboration, *Selection of jets produced in 13 TeV proton–proton collisions with the ATLAS detector*, ATLAS-CONF-2015-029, 2015, URL: `https://cds.cern.ch/record/2037702` (cit. on pp. 67, 103).

[36] ATLAS Collaboration, *Performance of the missing transverse momentum triggers for the ATLAS detector during Run-2 data taking*, JHEP **08** (2020) 080, arXiv: `2005.09554 [hep-ex]` (cit. on p. 68).

[37] ATLAS Collaboration, *Performance of electron and photon triggers in ATLAS during LHC Run 2*, Eur. Phys. J. C **80** (2020) 47, arXiv: `1909.00761 [hep-ex]` (cit. on p. 68).

[38] ATLAS Collaboration, *Performance of the ATLAS muon triggers in Run 2*, JINST **15** (2020) P09015, arXiv: `2004.13447 [hep-ex]` (cit. on p. 68).

[39] E. Bothmann et al., *Event generation with Sherpa 2.2*, SciPost Phys. **7** (2019) 034, arXiv: `1905.09127 [hep-ph]` (cit. on p. 69).

[40] T. Gleisberg and S. Höche, *Comix, a new matrix element generator*, JHEP **12** (2008) 039, arXiv: `0808.3674 [hep-ph]` (cit. on p. 69).

[41] F. Cascioli, P. Maierhöfer, and S. Pozzorini, *Scattering Amplitudes with Open Loops*, Phys. Rev. Lett. **108** (2012) 111601, arXiv: `1111.5206 [hep-ph]` (cit. on p. 69).

[42] A. Denner, S. Dittmaier, and L. Hofer, *Collier: A fortran-based complex one-loop library in extended regularizations*, Comput. Phys. Commun. **212** (2017) 220, arXiv: `1604.06792 [hep-ph]` (cit. on p. 69).

[43] S. Frixione, G. Ridolfi, and P. Nason, *A positive-weight next-to-leading-order Monte Carlo for heavy flavour hadroproduction*, JHEP **09** (2007) 126, arXiv: `0707.3088 [hep-ph]` (cit. on p. 69).

[44] P. Nason, *A new method for combining NLO QCD with shower Monte Carlo algorithms*, JHEP **11** (2004) 040, arXiv: `hep-ph/0409146` (cit. on p. 69).

[45] S. Frixione, P. Nason, and C. Oleari, *Matching NLO QCD computations with parton shower simulations: the POWHEG method*, JHEP **11** (2007) 070, arXiv: `0709.2092 [hep-ph]` (cit. on p. 69).

[46] S. Alioli, P. Nason, C. Oleari, and E. Re, *A general framework for implementing NLO calculations in shower Monte Carlo programs: the POWHEG BOX*, JHEP **06** (2010) 043, arXiv: `1002.2581 [hep-ph]` (cit. on p. 69).

[47] M. Beneke, P. Falgari, S. Klein, and C. Schwinn, *Hadronic top-quark pair production with NNLL threshold resummation*, Nucl. Phys. B **855** (2012) 695, arXiv: `1109.1536 [hep-ph]` (cit. on p. 70).

[48] M. Cacciari, M. Czakon, M. Mangano, A. Mitov, and P. Nason, *Top-pair production at hadron colliders with next-to-next-to-leading logarithmic soft-gluon resummation*, Phys. Lett. B **710** (2012) 612, arXiv: 1111.5869 [hep-ph] (cit. on p. 70).

[49] P. Bärnreuther, M. Czakon, and A. Mitov, *Percent-Level-Precision Physics at the Tevatron: Next-to-Next-to-Leading Order QCD Corrections to $q\bar{q} \to t\bar{t} + X$*, Phys. Rev. Lett. **109** (2012) 132001, arXiv: 1204.5201 [hep-ph] (cit. on p. 70).

[50] J. Alwall et al., *The automated computation of tree-level and next-to-leading order differential cross sections, and their matching to parton shower simulations*, JHEP **07** (2014) 079, arXiv: 1405.0301 [hep-ph] (cit. on p. 71).

[51] T. Sjöstrand et al., *An introduction to PYTHIA 8.2*, Comput. Phys. Commun. **191** (2015) 159, arXiv: 1410.3012 [hep-ph] (cit. on p. 71).

[52] D. J. Lange, *The EvtGen particle decay simulation package*, Nucl. Instrum. Meth. A **462** (2001) 152 (cit. on p. 71).

[53] ATLAS Collaboration, *Electron and photon performance measurements with the ATLAS detector using the 2015–2017 LHC proton–proton collision data*, JINST **14** (2019) P12006, arXiv: 1908.00005 [hep-ex] (cit. on pp. 72, 100).

[54] ATLAS Collaboration, *Muon reconstruction and identification efficiency in ATLAS using the full Run 2 pp collision data set at $\sqrt{s} = 13$ TeV*, Eur. Phys. J. C **81** (2020) 578, arXiv: 2012.00578 [hep-ex] (cit. on pp. 72, 100).

[55] ATLAS Collaboration, *Jet reconstruction and performance using particle flow with the ATLAS Detector*, Eur. Phys. J. C **77** (2017) 466, arXiv: 1703.10485 [hep-ex] (cit. on pp. 72, 100).

[56] ATLAS Collaboration, *Performance of pile-up mitigation techniques for jets in pp collisions at $\sqrt{s} = 8$ TeV using the ATLAS detector*, Eur. Phys. J. C **76** (2016) 581, arXiv: 1510.03823 [hep-ex] (cit. on pp. 72, 100).

[57] ATLAS Collaboration, *Tagging and suppression of pileup jets with the ATLAS detector*, ATLAS-CONF-2014-018, 2014, URL: https://cds.cern.ch/record/1700870 (cit. on pp. 72, 100).

[58] ATLAS Collaboration, *Local Hadronic Calibration*, 2008, URL: https://cds.cern.ch/record/1112035 (cit. on pp. 73, 75, 100).

[59] M. Cacciari, G. P. Salam, and G. Soyez, *The anti-k_t jet clustering algorithm*, JHEP **04** (2008) 063, arXiv: 0802.1189 [hep-ph] (cit. on pp. 73, 75, 100).

[60] M. Cacciari, G. P. Salam, and G. Soyez, *FastJet user manual*, Eur. Phys. J. C **72** (2012) 1896, arXiv: 1111.6097 [hep-ph] (cit. on pp. 73, 75, 100).

[61] D. Krohn, J. Thaler, and L.-T. Wang, *Jet trimming*, JHEP **02** (2010) 084, arXiv: 0912.1342 [hep-ph] (cit. on pp. 73, 100).

[62] S. D. Ellis and D. E. Soper, *Successive combination jet algorithm for hadron collisions*, Phys. Rev. D **48** (1993) 3160, arXiv: hep-ph/9305266 (cit. on pp. 73, 100).

[63] ATLAS Collaboration, *Jet mass reconstruction with the ATLAS Detector in early Run 2 data*, ATLAS-CONF-2016-035, 2016, URL: https://cds.cern.ch/record/2200211 (cit. on pp. 73, 101).

[64] ATLAS Collaboration, *In situ calibration of large-radius jet energy and mass in 13 TeV proton–proton collisions with the ATLAS detector*, Eur. Phys. J. C **79** (2019) 135, arXiv: 1807.09477 [hep-ex] (cit. on pp. 73, 101).

[65] A. J. Larkoski, G. P. Salam, and J. Thaler, *Energy correlation functions for jet substructure*, JHEP **06** (2013) 108, arXiv: 1305.0007 [hep-ph] (cit. on pp. 73, 101).

[66] A. J. Larkoski, I. Moult, and D. Neill, *Power counting to better jet observables*, JHEP **12** (2014) 009, arXiv: 1409.6298 [hep-ph] (cit. on pp. 73, 101).

[67] M. Cacciari, G. P. Salam, and G. Soyez, *The Catchment Area of Jets*, JHEP **04** (2008) 005, arXiv: 0802.1188 [hep-ph] (cit. on pp. 74, 101).

[68] ATLAS Collaboration, *Boosted hadronic vector boson and top quark tagging with ATLAS using Run 2 data*, ATL-PHYS-PUB-2020-017, 2020, URL: https://cds.cern.ch/record/2724149 (cit. on pp. 74, 101).

[69] C. G. Lester and D. J. Summers, *Measuring masses of semi-invisibly decaying particles pair produced at hadron colliders*, Phys. Lett. B **463** (1999) 99, arXiv: hep-ph/9906349 (cit. on pp. 79, 104).

[70] A. Barr, C. Lester, and P. Stephens, *A variable for measuring masses at hadron colliders when missing energy is expected; m_{T2}: the truth behind the glamour*, J. Phys. G **29** (2003) 2343, arXiv: hep-ph/0304226 (cit. on pp. 79, 104).

[71] ATLAS Collaboration, *Internal note of SUSY inclusive 0-lepton analysis (ANA-SUSY-2018-22).*, ATL-COM-PHYS-2018-1416, 2020, URL: https://cds.cern.ch/record/2641285 (cit. on p. 82).

[72] ATLAS Collaboration, *Internal note of SUSY stop $t\bar{t}+E_{\mathrm{T}}^{\mathrm{miss}}$ 0-lepton analysis (ANA-SUSY-2018-12).*, ATL-COM-PHYS-2018-1654, 2020, URL: https://cds.cern.ch/record/2649377 (cit. on p. 82).

[73] ATLAS Collaboration, *Internal note of SUSY sbottom $b\bar{b}+E_{\mathrm{T}}^{\mathrm{miss}}$ analysis (ANA-SUSY-2018-34).*, ATL-COM-PHYS-2019-1380, 2020, URL: https://cds.cern.ch/record/2699826 (cit. on p. 82).

[74] ATLAS Collaboration, *Search for electroweak production of supersymmetric particles in final states with two or three leptons at $\sqrt{s}=13$ TeV with the ATLAS detector*, (2018), arXiv: 1803.02762 [hep-ex] (cit. on p. 90).

[75] H. Goldberg, *Constraint on the Photino Mass from Cosmology*, Phys. Rev. Lett. **50** (1983) 1419 (cit. on p. 94), Erratum: Phys. Rev. Lett. **103** (2009) 099905.

[76] J. Ellis, J. Hagelin, D. V. Nanopoulos, K. A. Olive, and M. Srednicki, *Supersymmetric relics from the big bang*, Nucl. Phys. B **238** (1984) 453 (cit. on p. 94).

[77] *Search for pair production of Higgsinos in final states with at least three b-tagged jets in $\sqrt{s}=13$ TeV pp collisions using the ATLAS detector*, Phys. Rev. D **98** (9 2018) 092002, URL: https://link.aps.org/doi/10.1103/PhysRevD.98.092002 (cit. on p. 94).

[78] CMS Collaboration, *Search for Higgsino pair production in pp collisions at $\sqrt{s}=13$ TeV in final states with large missing transverse momentum and two Higgs bosons decaying via $H\to b\bar{b}$*, Phys. Rev. D **97** (2018) 032007, arXiv: 1709.04896 [hep-ex] (cit. on p. 95).

[79] *Snowmass White Paper Contribution: Physics with the Phase-2 ATLAS and CMS Detectors*, tech. rep., All figures including auxiliary figures are available at https://atlas.web.cern.ch/Atlas/GROUPS/PHYSICS/PUBNOTES/ATL-PHYS-PUB-2022-018: CERN, 2022, URL: https://cds.cern.ch/record/2805993 (cit. on p. 95).

[80] *ATLAS Phase-II Upgrade Scoping Document*, tech. rep., CERN, 2015, URL: https://cds.cern.ch/record/2055248 (cit. on p. 96).

[81] *Technical Design Report for the ATLAS Inner Tracker Strip Detector*, tech. rep., CERN, 2017, URL: https://cds.cern.ch/record/2257755 (cit. on p. 96).

[82] *Technical Design Report for the Phase-II Upgrade of the ATLAS Muon Spectrometer*, tech. rep., CERN, 2017, URL: https://cds.cern.ch/record/2285580 (cit. on p. 96).

[83] *ATLAS Liquid Argon Calorimeter Phase-II Upgrade: Technical Design Report*, tech. rep., CERN, 2017, URL: https://cds.cern.ch/record/2285582 (cit. on p. 96).

[84] *Technical Design Report for the Phase-II Upgrade of the ATLAS Tile Calorimeter*, tech. rep., CERN, 2017, URL: https://cds.cern.ch/record/2285583 (cit. on p. 96).

[85] *Technical Design Report for the Phase-II Upgrade of the ATLAS TDAQ System*, tech. rep., CERN, 2017, URL: https://cds.cern.ch/record/2285584 (cit. on pp. 96, 97).

[86] *Technical Design Report for the ATLAS Inner Tracker Pixel Detector*, tech. rep., CERN, 2017, URL: https://cds.cern.ch/record/2285585 (cit. on p. 96).

[87] *Technical Design Report: A High-Granularity Timing Detector for the ATLAS Phase-II Upgrade*, tech. rep., CERN, 2020, URL: https://cds.cern.ch/record/2719855 (cit. on p. 96).

[88] *Expected Tracking Performance of the ATLAS Inner Tracker at the HL-LHC*, tech. rep., All figures including auxiliary figures are available at https://atlas.web.cern.ch/Atlas/GROUPS/PHYSICS/PUBNOTES/ATL-PHYS-PUB-2019-014: CERN, 2019, URL: https://cds.cern.ch/record/2669540 (cit. on p. 96).

[89] ATLAS Collaboration, *Search for charginos and neutralinos in final states with two boosted hadronically decaying bosons and missing transverse momentum in pp collisions at $\sqrt{s} = 13$ TeV with the ATLAS detector*, Physical Review D **104** (2021), URL: https://doi.org/10.1103%2Fphysrevd.104.112010 (cit. on pp. 97, 98, 107).